

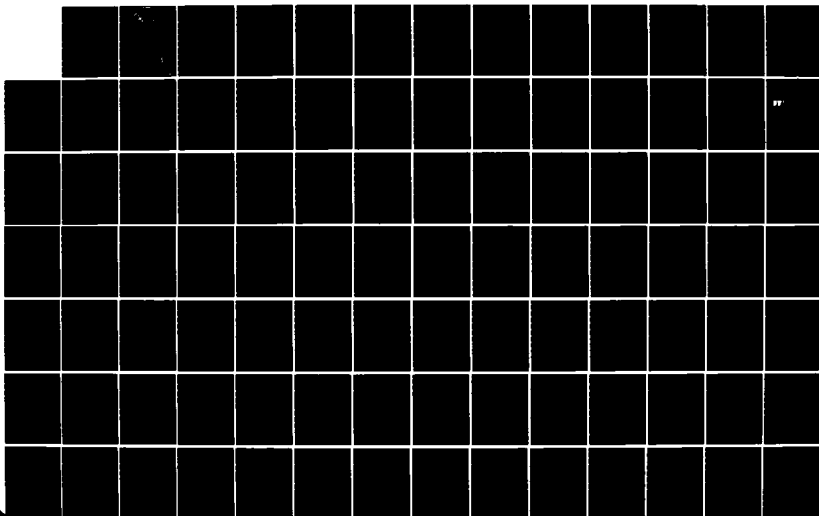
AD-A151 999

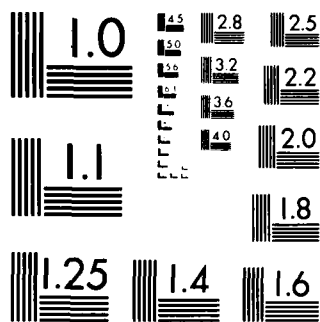
ANALYSIS OF COMBUSTION OSCILLATIONS IN HETEROGENEOUS
SYSTEMS(U) PRINCETON COMBUSTION RESEARCH LABS INC NJ
H BEN-REUVEN MAY 84 PCRL-FR-84-002 AFOSR-TR-85-0250
F49620-82-C-0062 F/G 21/2

1/2

UNCLASSIFIED

NL





MICROCOPY RESOLUTION TEST CHART
NATIONAL BUREAU OF STANDARDS-1963-A

AD-A151 999

AFOSR-TR-85-0250

③
EPA

PRINCETON COMBUSTION RESEARCH LABORATORIES, INC.

ANALYSIS OF COMBUSTION OSCILLATIONS
IN
HETEROGENEOUS SYSTEMS

DTIC FILE COPY

Approved for public release;
distribution unlimited.

DTIC
ELECTE
APR 01 1985
S E D

PRINCETON COMBUSTION RESEARCH LABORATORIES, INC.

475 U.S. Highway One, Monmouth Junction, NJ 08852 Telephone (609) 452-9200

Approved for public release;
distribution unlimited.

85 03 13 020



DISCLAIMER NOTICE

**THIS DOCUMENT IS BEST QUALITY
PRACTICABLE. THE COPY FURNISHED
TO DTIC CONTAINED A SIGNIFICANT
NUMBER OF PAGES WHICH DO NOT
REPRODUCE LEGIBLY.**

Final Report
PCRL-FR-84-002
May 1984

ANALYSIS OF COMBUSTION OSCILLATIONS
IN
HETEROGENEOUS SYSTEMS

Copy even if DTIC does not
permit fully legible reproduction

Contract No. F49620-82-C-0062

Submitted to

USAF, AFSC
Air Force Office of Scientific Research
ATTN: AFOSR/NA (Dr. Leonard H. Caveny)
Building 410
Bolling Air Force Base, DC 20332

Submitted by

Dr. Moshe Ben-Reuven
PRINCETON COMBUSTION RESEARCH LABORATORIES, INC.
475 U.S. Highway One
Monmouth Junction, NJ 08852

AIR FORCE OFFICE OF SCIENTIFIC RESEARCH
NOTICE OF
This report is
Approved
Dissemination
MATTHEW
Chief, Technical

SECRET
APR 01 1985
E

UNCLASSIFIED

SECURITY CLASSIFICATION OF THIS PAGE

REPORT DOCUMENTATION PAGE

1a. REPORT SECURITY CLASSIFICATION UNCLASSIFIED		1b. RESTRICTIVE MARKINGS NONE	
2a. SECURITY CLASSIFICATION AUTHORITY		3. DISTRIBUTION/AVAILABILITY OF REPORT Approved for Public Release; Distribution is Unlimited.	
2b. DECLASSIFICATION/DOWNGRADING SCHEDULE		5. MONITORING ORGANIZATION REPORT NUMBER(S) AFOSR-TR- 82-0250	
4. PERFORMING ORGANIZATION REPORT NUMBER(S) PCRL-FR-84-002		7a. NAME OF MONITORING ORGANIZATION <i>Same as #7</i>	
6a. NAME OF PERFORMING ORGANIZATION Princeton Combustion Research Laboratories, Inc.	6b. OFFICE SYMBOL (If applicable)	7b. ADDRESS (City, State and ZIP Code)	
6c. ADDRESS (City, State and ZIP Code) 475 U.S. Highway One Monmouth Junction, NJ 08852		9. PROCUREMENT INSTRUMENT IDENTIFICATION NUMBER F49620-82-C-0062	
8a. NAME OF FUNDING/SPONSORING ORGANIZATION Air Force Office of Scientific Research	8b. OFFICE SYMBOL (If applicable) NA	10. SOURCE OF FUNDING NOS.	
8c. ADDRESS (City, State and ZIP Code) Bolling AFB DC 20332		PROGRAM ELEMENT NO. 61102F	PROJECT NO. 2308
11. TITLE (Include Security Classification) Combustion Oscillations in Heterogeneous Systems		TASK NO. A1	WORK UNIT NO.
12. PERSONAL AUTHOR(S) Dr. Moshe Ben-Reuven			
1. TYPE OF REPORT FINAL REPORT	13b. TIME COVERED FROM 3/15/82 to 3/15/84	14. DATE OF REPORT (Yr., Mo., Day) May 1984	15. PAGE COUNT 95
16. SUPPLEMENTARY NOTATION			
17. COSATI CODES		18. SUBJECT TERMS (Continue on reverse if necessary and identify by block number)	
FIELD	GROUP	SUB GR	
21.08	21.02		
20.13			
		Combustion instability; solid propellant rocket motors; velocity-coupled instability; visco-acoustic coupling; MacCormack integration scheme; injected cold flow simulation.	
19. ABSTRACT (Continue on reverse if necessary and identify by block number)			
<p>This study is aimed at elucidation of the physical mechanisms capable of driving acoustic instability in solid propellant rocket motors, of the type termed velocity-coupled instability. The first and second tasks of this research, Critical Literature Review, and Order of Magnitude Analyses of velocity-coupling mechanisms, have been reported earlier. The third part of the study, Analytical Simulation of the Interior Flowfield Within a Solid Propellant Grain, is reported herein. The subject of the present analysis is simulation of the cold-flow experiments by Dr. Brown at UTC/CSD, in which nitrogen is injected through the porous sidewalls of a cylindrical pipe, creating an internal axisymmetric flow field. A comprehensive analytical model of the</p>			
20. DISTRIBUTION/AVAILABILITY OF ABSTRACT CLASSIFIED/UNLIMITED <input checked="" type="checkbox"/> SAME AS RPT <input type="checkbox"/> DTIC USERS <input type="checkbox"/>		21. ABSTRACT SECURITY CLASSIFICATION UNCLASSIFIED	
22a. NAME OF RESPONSIBLE INDIVIDUAL LEONARD H CAVENY		22b. TELEPHONE NUMBER (Include Area Code) (202) 767-4937	22c. OFFICE SYMBOL AFOSR/NA

UNCLASSIFIED

SECURITY CLASSIFICATION OF THIS PAGE

nonsteady flow processes entails a system of four partial differential equations for continuity, radial and axial momentum, and thermal enthalpy. The flowfield is considered compressible and viscous, with all of the dissipative terms included. A focal point of the analysis has been the thin viscous sublayer adjacent to the porous surface, where visco-acoustic interactions occur. Order of magnitude analysis, as well as earlier experimental data (demonstrating great enhancement of wall heat transfer at the presence of a sufficiently intense acoustic field), indicate that this is a highly plausible velocity-coupled instability mechanism. A singular perturbation analysis was carried out for the viscous sublayer; a simple algebraic expression for the first order axial pressure drop within the port was obtained, correlating the available UTC/CSD experimental (steady state) data excellently, with their inherent Reynolds No. effects. A numerical finite-difference algorithm has been developed, using a modified (un-split) MacCormack integration scheme; the code utilizes nonuniform radial stepsize, with very fine mesh near the porous surface. Results of converged steady-state cases are reported herein. The numerically-calculated trends are in agreement with both available experimental observations and the results of perturbation analysis.

Accession For	
NTIS GRA&I	X
DTIC TAB	
Unannounced	
Justification	
By _____	
Distribution/	
Availability Codes	
Dist	Avail and/or Special
A-1	73 CV

Authors Comments:
Mathematical Model,
Comparison with

TABLE OF CONTENTS

	<u>Page</u>
Title Page	i
DD Form 1473.....	ii
Table of Contents.....	iv
1. Introduction.....	1
2. Functional Description of the Finite Difference Code.....	4
2.1 Introduction.....	4
2.2 Formulation of the Differential System.....	6
2.3 The Finite Difference Algorithm: 2-Step/Unsplit MacCormack.....	9
2.4 The Boundary Conditions.....	12
2.5 Discussion of Results.....	13
2.6 Conclusions and Recommendations.....	15
Figures: Section 2.....	17
3. User's Manual for the "MOSCO" Cold Flow Simulation Computer Program.....	29
3.1 Input Description.....	29
3.1.1 Block Data Statement.....	29
3.2 Main Program.....	32
3.3 Time-Integration Procedure.....	33
3.3.1 Subroutine TIMINT.....	33
3.3.2 Subroutines DGDX and DFDR.....	35
3.3.3 Subroutine SORCE.....	37
3.3.4 Special Functions.....	39
3.3.5 Subroutine BNDRY.....	40

3.4	Output Section.....	41
3.4.1	Subroutine PRINT.....	41
3.4.2	Subroutines XPRNT1 and XPRNT2.....	45
3.5	Subroutine SDATA: Calculation of the Constant Parameters and the Initial Data.....	46
3.6	Printout - A Datum Case.....	50
3.6.1	Input and Calculated Parameters from SDATA.....	50
3.6.2	Initial Data: Culick's Inviscid Profiles.....	51
3.6.3	Final Step Printout, the Datum Case (1201 Dt).....	54
Appendix A.....		60
Appendix B.....		72

1. INTRODUCTION

This report summarizes a three year effort under AFOSR contract to elucidate plausible velocity coupling mechanisms in solid propellant rocket instability.

"Velocity coupling" is a rather general term, which would tend to encompass all phenomena not included in pressure-coupled instability; in practice, the majority of instability phenomena in solid propellant rocket motors seem to resist explanation by pure pressure-coupled instability. In most general terms, pressure is a state variable, and the response of the propellant combustion to pressure perturbations could be explained without detailed account of the associated fluid dynamic processes within the motor -- provided the gaseous combustion region were sufficiently thin to be conceived as quasi-steady (in the sense of responding "instantaneously" to any pressure perturbation). This leaves the thermal wave relaxation within the condensed phase as the only possible mechanism for dynamic coupling with an external acoustic field, considering a Rayleigh instability mechanism. This is in general insufficient. Fluid dynamic phenomena must be incorporated to account for other instability mechanisms. This means, in particular that the instability characteristics of a given propellant/motor configuration can not be conceived globally, based on the propellant properties alone: one must take into account the particular internal flow field, or fluid-dynamic variables. This complicates the task of instability calculation considerably, for obvious reasons.

After the effect of pressure perturbation has been separated, what seems to remain is the (external, tangential) velocity effect; hence the name for the instability coupling mechanism. In practice, this may involve turbulence-combustion interaction, residual exothermicity (slow kinetics) coupling, visco-acoustic coupling, vortex-boundary interaction, or other diverse phenomena, all having to do with instability mechanisms coupled with the fluid dynamics of the internal flow.

The phenomena under consideration are also characteristically nonlinear, in the sense that the response depends upon the perturbation amplitude, and efficient coupling (and energy exchange) exists between different frequency components (in particular, high-frequencies influencing low-frequency behavior). This accounts for the considerable complication in the analysis, and renders limited utility to quasi-linearized calculations.

Against this general background, the present investigation has engaged in the following three major tasks, undertaken during a period of three years: (1) a critical literature evaluation regarding mechanisms of velocity-coupled instability, (2) a detailed order of magnitude evaluation of the various mechanisms, and (3) a detailed numerical analysis of the most prominent mechanism.

The major accomplishments of the present study are in the three aforementioned areas: The critical literature review included vortex/boundary interaction, an area studied previously by Flandro, Combustion/Acoustic interaction in the coreflow, due to residual exothermicity, studied previously by Ben-Reuven and Caveny in conjunction with nitramine rocket propellants, and visco-acoustic coupling. All of these areas have been covered extensively in the two foregoing annual interim scientific reports under this contract.

The subject of turbulence-combustion interaction has also received due coverage during the present study, although outside of the areas covered in the two previous interim reports.

An additional objective of the study was to establish and maintain contact with the experimental study, carried out in parallel at UTC/CSD, under Dr. Robert Brown. This has been likewise carried out, through numerous discussions and exchange of information, which definitely shaped both the focus and the outcome of the present velocity coupling analysis.

Aside from the literature surveys published earlier, cf AFOSR TR-82-1017, this analysis has two major accomplishments: (1) Identification of the visco/acoustic coupling as a potentially powerful velocity-coupled instability mechanism, through both detailed order of magnitude study, as well as small-perturbation (asymptotic) analysis, and (2) development of an explicit numerical finite-difference algorithm, for solution of the nonsteady, compressible, axisymmetric flowfield within the rocket motor, geared toward the elucidation of the visco-acoustic effect predominant near the injected surface.

An interesting outcome of the present study is in the area of steady injected internal flow. The singular small-perturbation analysis has enabled analytical expressions for the dimensionless axial pressure drop, and the surface friction coefficient, in terms of the injection Reynolds number and Mach number. These afford exceptionally good agreement with the experimental data obtained by Dr. Brown at CSD/UTC recently, as well as earlier measurements by Olson and Eckert. These tend to be collaborated by the numerical results generated recently by this author. The evidence points to the plausibility of the visco/acoustic driving mechanism (as a necessary condition); in the meantime, one need not invoke turbulence or other phenomena to explain the axial pressure drop deviation from the pure inviscid (rotational) theory of Culick Taylor, Berman, and others. The reader is referred to Appendices A and B for detailed discussions.

The small perturbation boundary layer analysis of the viscous sublayer at steady state has been the subject of two publications, presented at the recent (1983) 20th JANNAF Combustion Meeting, and at the Aerospace Sciences Meeting of the AIAA (Jan. 1984); the latter has been submitted to the AIAA Journal for publication. Both papers are enclosed in Appendices A and B mentioned above.

At the closing of the present research period, the computational finite-difference algorithm developed has just begun to yield useful results. Numerical stability was demonstrated in marching toward steady state with fixed injection rate and wall temperature imposed; the initial data utilized Culick's inviscid solutions. Some of the results following 1200 timewise integration steps are shown in Figures 2.1 through 2.4 herein. In particular, the computed axial pressure drop shown in Figure 2.1, is similar to that measured by Brown et al (1983), and correlated by the perturbation analysis of Ben-Reuven, all of which depart from the axial pressure drop predicted by the inviscid theory. Integration can be readily carried out with imposed time-dependent boundary data, to simulate the perturbed exit nozzle behavior in the CSD experiment.

The explicit finite difference algorithm developed herein follows a modular design, and allows for arbitrary radial mesh specification (within the limits of physical resolution and numerical stability). The modular structure can readily accommodate additions [more comprehensive boundary data treatment; accounting for combustion; including turbulence transport], in the form of subprograms. A joint publication with Prof. Vichnevetsky is in preparation on the numerical stability features when source terms are incorporated.

The remainder of the present report comprises a User's Manual for the "MOSCO" finite difference program. Three chapters provide background information regarding the formulation of the partial differential system and the finite difference algorithm used for solution, a discussion of the program features, and a discussion of the results, respectively.

2. FUNCTIONAL DESCRIPTION OF THE FINITE DIFFERENCE CODE.

2.1 INTRODUCTION.

MOSCO is a finite difference FORTRAN code, to solve the viscous, time-dependent, compressible Navier-Stokes equations. The four equations of motion, for an axi-symmetric geometry are: continuity, axial momentum, radial momentum and energy. The finite difference algorithm used is a **modified unsplit MacCormack scheme**. The general mode of integration is explicit predictor-corrector.

For a complete description of the original scheme and a discussion of the limitations thereof, the reader is referred to the two original MacCormack papers listed in References 1 and 2.

A detailed discussion of the partial-differential system is given in Ref. 3 herein. It should be pointed out that for a nonsteady, compressible configuration, **the flowfield is non-solenoidal**, i.e., divergence of the velocity vector is nonzero. This gives rise to a number of terms emanating from the symmetrical part of the stress tensor, which can not be ignored in general.

The two important modifications made to the original scheme are as follows: (i) only **advective** terms are written in the conservation form (general flux terms), while dissipative terms of all kinds appear as "source" terms (non-conservative) in the finite-differenced equations of motion. Also, (ii) arbitrarily-varying radial mesh size is employed, along with a uniform axial mesh; along with the variation imposed in (i), this necessitates proper representation for the second-order and radially-space-centered first-order derivatives, to reflect the aforementioned nonuniformity and maintain second-order consistency of the scheme.

Actual implementation of the MOSCO program involves very small radial mesh-size near the $r=1$ boundary, representing the porous, injected wall. The mesh is then gradually increased toward $r=0$, at the cylindrical centerline. A ratio of 1/100 between the respective mesh sizes has been tried. A similar ratio would also hold normally between the smallest radial increment and the (uniform) axial mesh size.

Preliminary small perturbation analysis has pointed out the necessity of proper accounting for the near-wall processes, where viscous dissipation is dominant. The importance of these viscous processes to proper understanding of the steady state axial pressure distribution has been discussed elsewhere. The interaction between acoustic vibrations and the dissipative processes in this nearfield drives the visco-acoustic coupling mechanism, an important component of nonlinear velocity coupled instability. For this purpose, the fine radial stepsize near the wall is implemented.

The unsplit MacCormack scheme, under these conditions, has one

major drawback: to maintain numerical stability, the Courant-Friedrichs-Lewy condition is implemented to calculate the time step size according to the smallest spatial increment. Consequently, the **overall (uniform) time step** is very small, considering the value implied by the radial mesh near the centerline, or the regular axial mesh. Over a period of several thousands of timesteps, this might lead to an appreciable error regarding the timewise profiles. In this respect, the split MacCormack method might be superior for obtaining long-term transient or low frequency behavior.

The present algorithm is set up to integrate the fully dynamic system. Its limitations regarding long-time and low frequency behavior are recognized. The major advantage of the system relative to implicit integration algorithms is quite obvious, in obtaining typically low-cost and low CPU performance. Other advantages, due to the specific construction, are the modular structure, in which changes in the formulation are easy to implement, (details specific to the partial differential system being solved appear only in three subprograms) additions can be readily made (through auxiliary subprograms) and programming errors can be detected easily.

The general structure of OSC03, the cold-flow simulation FORTRAN code is depicted in Fig. 1. This is a development based on the earlier ROSCO-series, reported previously by this author.

The logic of the timewise integration cycle is shown in Fig. 2. The particular configuration corresponds to the marching toward steady state mode, pertaining to the configuration of the program listing in Appendix A herein.

A concise description of the partial differential system, the boundary data, and the finite difference method is given in the following Section. This is followed by a detailed glossary of input parameters, and the output maps. Options regarding the use of output data files were not included; other options which require extensive setup (and depend crucially on printer configuration), such as printer-plots, were omitted. The program listing, and a sample output are given in Appendices A and B, respectively.

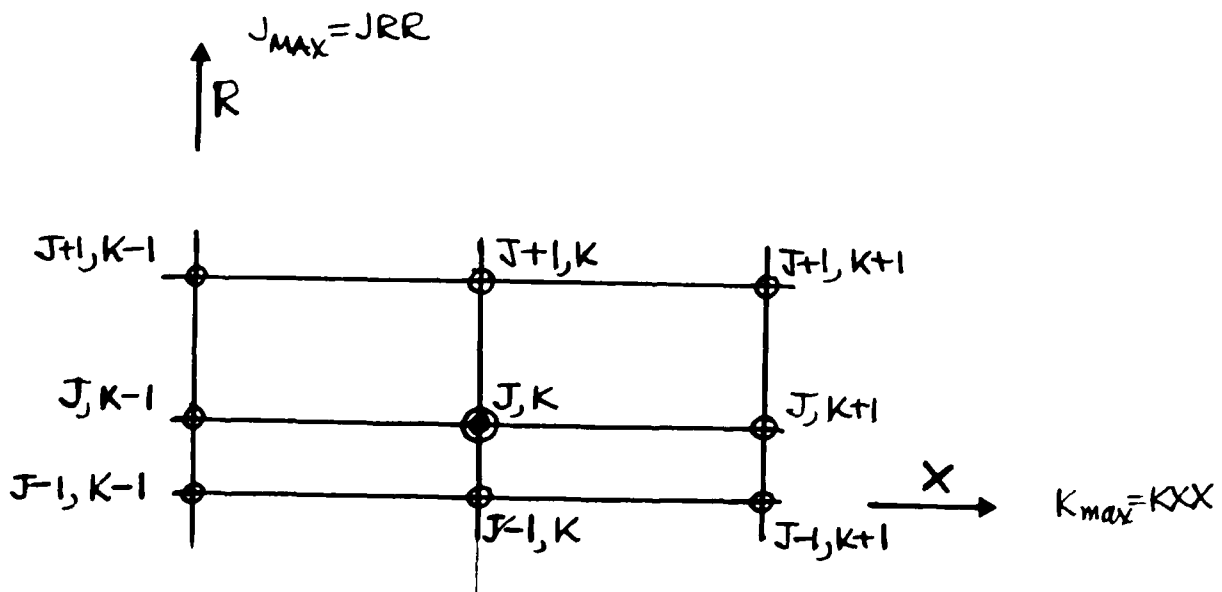
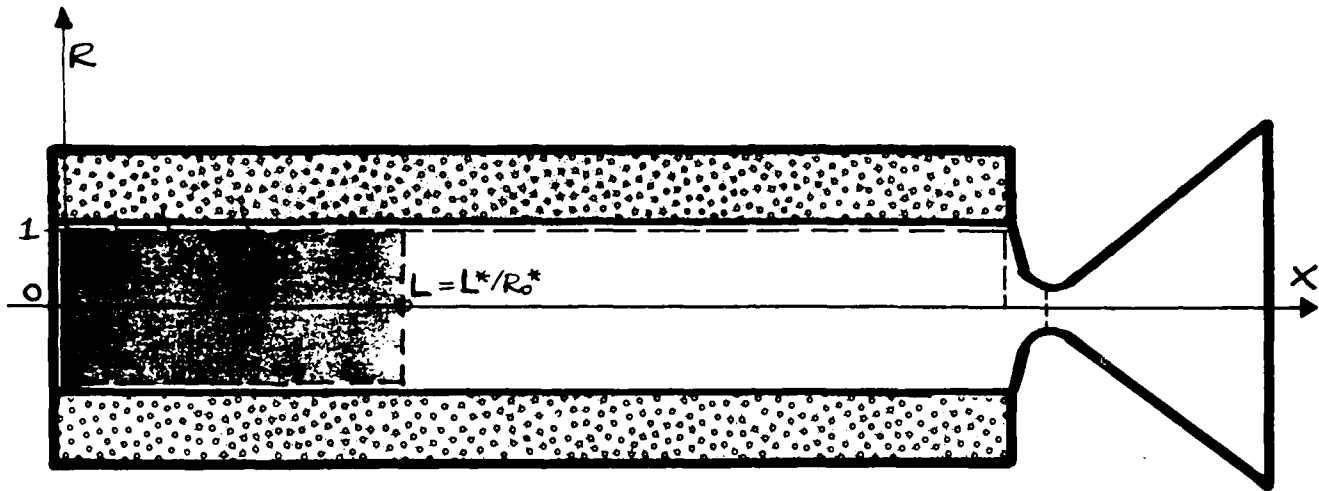


FIG. 2.3

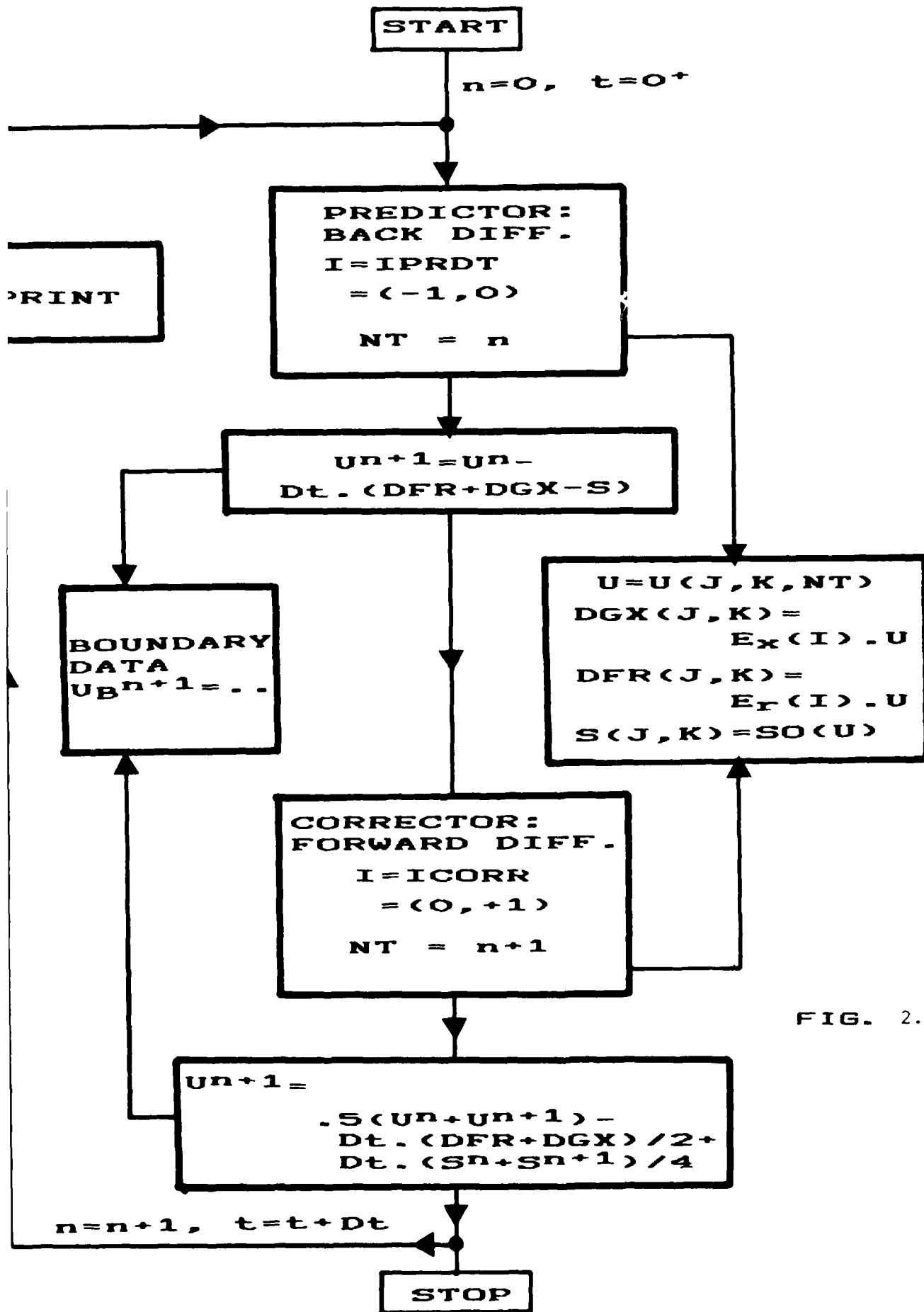


FIG. 2.2

"MOSCO" BLOCK DIAGRAM

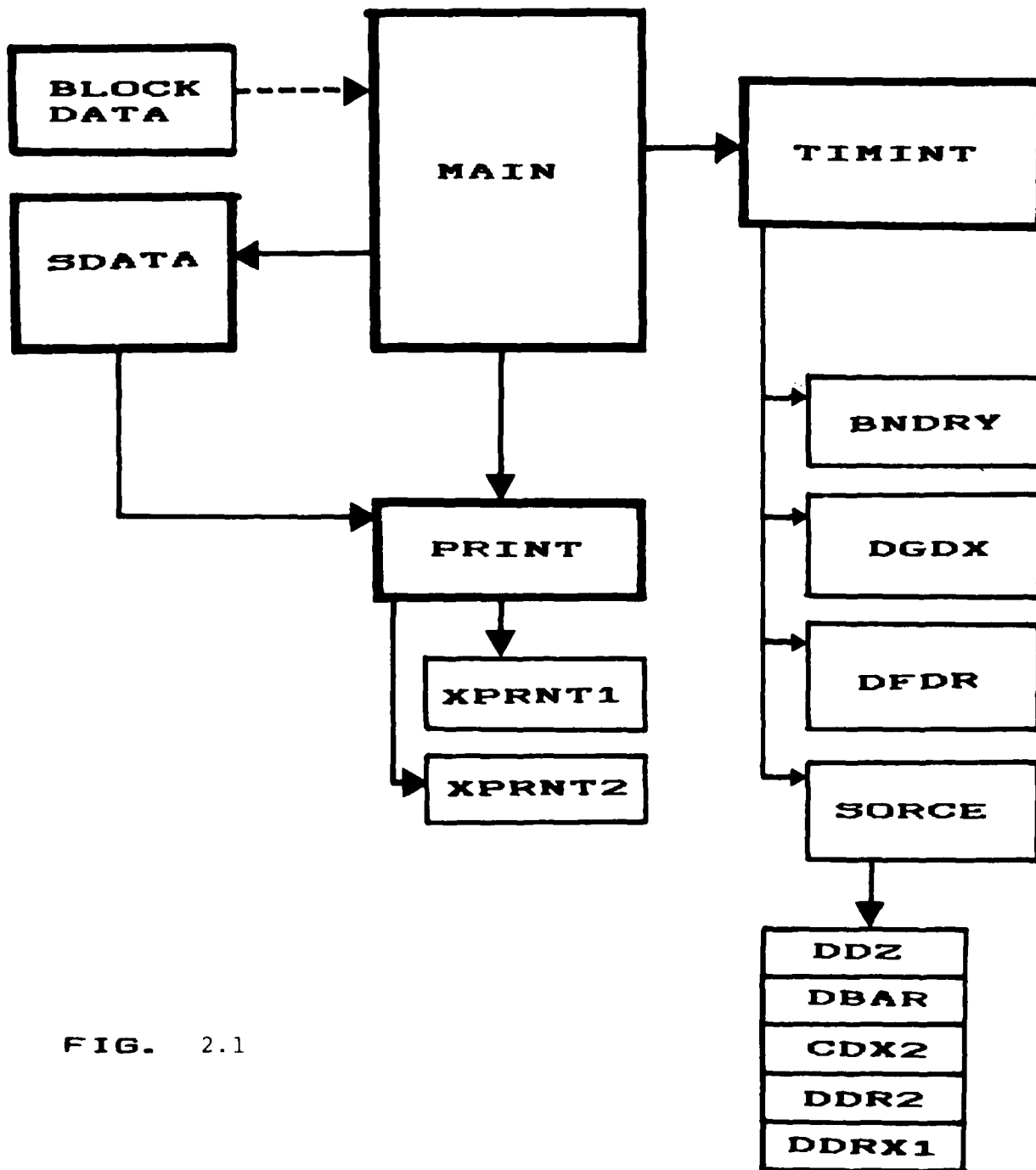


FIG. 2.1

The question of relevance of cold-flow simulation to internal rocket flows, and the use of porous materials to simulate propellants has been raised many times. Based on the present experience, it seems that both are highly relevant, although obviously defficient in several ways. For instance, normal propellants respond to a positive pressure perturbation by raising the burn rate, while a porous plug would yield a lower mass flow rate if the pressure differential across it decreased. The inability to simulate the high thermal-gradient region near the surface of a propellant with the existing injected flow techniques is another drawback. On the other hand, probing within the interior of a burning propellant grain is still quite impossible. The conclusion drawn is that cold flow injection and porous materials have many limitations, but could still be successfully utilized for study of certain limited physical interactions, certainly not the entire instability phenomena. An excellent example of such limited application is the visco-acoustic mechanism, which comprises a clear fluid dynamic phenomenon.

The importance of interior fluid dynamic considerations to the proper understanding of solid propellant motor behavior can not be overemphasized. Whether it is the highly-ordered, frequency dependent visco-acoustic phenomenon, acoustic-combustion interaction, or similar mechanisms of interaction, or turbulence/combustion effects-- all require details of the local fluid dynamic processes. It is therefore strongly recommended that both theoretical analysis and idealized experimental simulation of the internal flow field of solid propellant rockets be continued.

2.6 CONCLUSIONS AND RECOMMENDATIONS

A considerable amount of experimental data has been generated by the cold-flow simulation effort at UTC/CSD, by Dr. Brown. Nonsteady wall heat transfer coefficient measurements as well as hot wire anemometry were utilized. Since the wall heat transfer is very important to the understanding of combustion instability, the following comments are made. It appears that the coherently averaged spectra of the wall heat transfer, which filter out the RMS or DC-effects due to turbulence and viscous second-order interactions, demonstrate the validity of the visco-acoustic coupling mechanism, suggested by this author in our 1982/83 Interim Report. The original figures from Brown's Annual Report have been merely re-grouped here, in Figs. 2.8 through 2.12.

These figures show that the effect of increasing perturbation amplitude, (from A'/A of 0.6 to 5.9%) and increasing perturbation frequency (from 76 to 170 Hz) both cause enhanced wall heat transfer, coherently with the acoustic frequency, at axial stations considerably upstream of the velocity antinode of the first or second axial acoustic modes. All of these effects are explained by the visco-acoustic coupling mechanism.

When the same data were re-cast with the DC effects included, it is evident that the low amplitude phenomena are swamped by near-wall turbulence effects and other high frequency noise, peaking at the surface (as corresponding hot-wire traverses indicate). This occurs at roughly 10 diameters downstream of the head end. The higher perturbation amplitude and frequency coherence, nevertheless, persist way downstream of this point.

Other hot wire anemometry data, obtained by Dr. Brown during 1983, seemed to indicate relatively high turbulence intensities near the centerline (close to the head end) while these intensities increased toward the wall at downstream stations. It should be emphasized that these data were mostly obtained at the low perturbation amplitude of $A'/A = 0.6\%$; close to the centerline, the axial velocities are high, but du/dr is vanishing; in the meantime, both the radial velocity component as well as dv/dx are vanishingly small. Near the wall, however, the radial velocity is nonzero, and both du/dy and dv/dr are appreciable, while the axial velocity is small. The foregoing physical picture holds for most of the flowfield. One therefore expects the vorticity effects, responsible for turbulence generation, to be strongest near the walls, even though the walls are injected.

It is therefore suggested that the results pertaining to this low-amplitude of perturbation be thoroughly checked prior to any far reaching conclusions regarding the origin or evolution of turbulence in internal injected flows. The experimental evidence of most significance (and relevance to velocity coupling instability) seems to be the steady state data, and the high perturbation amplitude and frequency data.

On the other hand, the corresponding (not normalized) radial velocity distribution at the same station, shown in Fig. 2.7, departs appreciably from its inviscid counterpart. This is not surprising, as it infers that du/dx (axial acceleration) is somewhat less than the inviscid prediction, since

$$\partial u / \partial x \approx -(\partial v / \partial r + v/r)$$

according to the continuity equation with negligible compressibility; so that whenever dv/dr obtains a positive increment, as occurs near the surface in Fig. 2.7, du/dx decreases accordingly. This is consistent with the information obtained in the axial pressure drop, Fig. 2.4, which shows that the computed p-drop is somewhat smaller than the theoretical inviscid prediction, since the axial acceleration balances the axial pressure gradient in the coreflow, cf Appendix A.

In conclusion, the steady state results herein are both self-consistent as well as in agreement with the predictions of the viscous (perturbational) wall layer analysis, and the recent measurements of Brown. The algorithm has been demonstrated numerically stable in this mode, and can be utilized for nonsteady flowfield simulation.

2.5 DISCUSSION OF RESULTS

Some of the results obtained from the numerical solutions will be discussed herein, pertaining to marching toward steady state. The reader is referred to Figs. 2.4 - 2.7 in which converged data following 1201 timewise integration steps is summarized. Considerably more data is available at both the last step and intermediate time-levels as well; a partial output listing of the same datum case discussed herein is appended to the User's Guide, Chapter 3 .

It should be pointed out that there is nothing particular about the Datum Case configuration used. The specific radial mesh divisions are in no way "the best" or optimal. The axial mesh size is quite large (1.0 in the dimensionless system, i.e., equal to one radial length); smaller mesh size and considerably more points in both radial and axial directions would definitely yield better quality of data. The computer program can accommodate both with only minor (and obvious) modification to Common statements and the input data.

The physical input data used was to simulate cold nitrogen injection under experimental conditions similar to those used by Dr. Brown at CSD, without attempting to simulate any particular set of conditions exactly. Again, conditions like the injection velocity, temperature, chamber reference pressure, etc can be readily varied, over a sufficiently wide parametric range.

In the meantime, it is asserted that the finite difference scheme is numerically stable, within the limits of time-resolution discussed in Section 2.3, and that the formulation as well as its implementation correspond to the compressible Navier-Stokes equations, in axisymmetric form. In numerous tests with coarse radial mesh, (the viscous scales being much smaller), numerical instability consistently developed; the aforementioned stability therefore obviously depends on the degree of spatial resolution near the surface.

In Fig. 2.4 the axial pressure drop is plotted against axial distance, x . the trend in departure from the inviscid solution of Culick is the same as that measured by Brown at CSD. In Fig. 2.5, the friction coefficient and Stanton number (heat transfer coefficient) are plotted against the injection ratio. The nearly-linear trend is similar to that measured (for C_f) by Olson and Eckert. Departure from the inviscid theoretical normalized axial velocity profile is quite small at 10 radial distances from the head end, as shown in Fig. 2.6.

2.4 THE BOUNDARY CONDITIONS

As differs from the physical plane, all of the dependent variables in the numerical simulation must be specified along each of the four boundaries. The available physical boundary data has been discussed already in section 1.2 herein.

Along the centerline, $(x, r=0)$, all of the boundary data is physically available. The radial gradients of the density, axial mass flux, and enthalpy, are all zero; the radial velocity is zero:

$$\begin{aligned} U(1,1,K) &= U(1,2,K) \\ U(3,1,K) &= U(3,2,K) \\ U(4,1,K) &= U(4,2,K) \end{aligned} ; \quad V(2,1,K) = 0.$$

Along the porous sidewall, $(x, r=1)$ the axial velocity is zero, the injection velocity and the wall temperature are specified, and the pressure extrapolated, using a three-point algorithm:

C-----POROUS SURFACE: PRESSURE EXTRAPOLATED. WALL ENTHALP=HWP.

```
DO 3 K=2,KXX
  U(4,JRR,K)=(RRS*U(4,JRM1,K)-U(4,JRM1-1,K))/RSM1
  3 U(1,JRR,K)=U(4,JRR,K)/HWP
```

$$V(3,JRR,K) = 0.$$

$$RRS = [r(JRR) - r(JRR-2)] / \Delta r(JRR-1); \quad RSM1 = RRS - 1.$$

This allows calculation of the density at the wall:

$$\rho_w = p/h_w \quad (\text{LOOP \#3 ABOVE}).$$

At the head end, $(x=0, r)$, both velocity components are zero, while the wall temperature is specified. The pressure is extrapolated axially to the wall, using a two-point, second order accurate extrapolation:

C-----HEAD END: $x=0$. NOTE: $U_2=0$ AND $U_3=0$, ALWAYS. WALL TEMP.=HW=F(R).

```
DO 2 J=1,JRM1
  U(4,J,1)=U(4,J,2)*2.-U(4,J,3)
  U(1,J,1)=U(4,J,1)/HWO
DO 2 M=1,MXX
  2 U(M,J,KXX)=U(M,J,KXM1)*2.-U(M,J,KXM1-1)
```

From which the density at the wall is calculated:

$$\rho(x=0) = p(x=0)/h_o \quad \text{cf. } U(1,J,1) \text{ ABOVE.}$$

At the exit plane, all of the variables are extrapolated axially, using a two-point formula:

$$U(J, KXX) = 2U(J, KXX-1) - U(J, KXX-2).$$

which simulates a continued duct, not the entrance to a choked nozzle; to simulate the latter, characteristics segments have to be utilized locally, in a finite difference form.

currently used, and the (regular) axial mesh size are such, that the minimal timestep is always obtained by use of delta-R, namely:

$$\Delta t_x = B \cdot \Delta x / \max_{j,k} (c+u) < \Delta t_e .$$

(20)

$$\frac{\partial^2 Q}{\partial r^2} \doteq \frac{2}{\Delta r_j + \Delta r_{j-1}} \left\{ \frac{Q_{j+1} - Q_j}{\Delta r_j} - \frac{Q_j - Q_{j-1}}{\Delta r_{j-1}} \right\}_k^n + O(\Delta r_j - \Delta r_{j-1}) \quad (17)$$

$$\frac{\partial^2 Q}{\partial r \partial x} \doteq \frac{1}{2\Delta x} \left\{ DOR_{k+1} - DOR_{k-1} \right\}_j^n \quad (18)$$

Obviously, the differences between adjacent radial increments should be small where the third order radial derivative is expected to be large, to insure small truncation error for the second derivative. This principle is indeed followed in the neighborhood of the porous wall; near the centerline, however, the third-order radial derivatives are expected to be quite negligible, so that a larger radial meshsize **variation** can be implemented.

The reason for the peculiar weighting factors in the radial flux terms within the predictor and corrector steps is now clear, to maintain second-order accuracy in the overall (combined) timestep integration; otherwise, (if the same finite-differencing is used for both axial and radial derivatives), the algorithm is consistent only to first order, with a radial diffusion term which is proportional to the **difference** between two adjacent radial increments.

The timestep size is determined by the smallest spatial increment, using the Courant-Friedrichs-Lewy stability condition,

$$\Delta t \equiv \Delta t_R = B \cdot \Delta r_{\min} / \max_{j,k} (C + v), \quad C \equiv 1/M_0 \quad (19)$$

where the coefficient $B < 1$ (strictly), is typically taken between 0.5 and 0.8.

Previous error analysis of a modified Lax-Wendroff scheme (one dimensional, nonsteady), which involved source terms has indicated that using a CFL number $B=0.5$ has clear advantages toward reduction of the induced numerical diffusivity. Due to the inherent similarities between both mathematical systems (predominantly hyperbolic in axial direction), and numerical method used (overall central-differences in space, predictor-corrector, explicit), the same CFL number is currently implemented. Performance in marching toward steady state is clearly superior to identical cases using datum case input with $B=0.8$, in terms of improved stability. In this mode of operation, the cost is an obviously longer overall integration time.

The relative magnitudes of the smallest radial increment

2.3 THE FINITE DIFFERENCE ALGORITHM: 2-STEP/UNSPLIT MacCORMACK

Following the original scheme by MacCormack, (1971, 1975) the following explicit two-step procedure is proposed, in a predictor-corrector manner:

$$\begin{aligned} \overline{U}_{j,k}^{n+1} = U_{j,k}^n - \Delta t \left(\frac{G_k - G_{k-1}}{\Delta x} \right)_j^n - \frac{\Delta t}{r_j} \cdot \frac{\Delta r_j}{\Delta r_j + \Delta r_{j-1}} \cdot \left(\frac{r_j F_j - r_{j-1} F_{j-1}}{\Delta r_{j-1}} \right)_k^n \\ + \Delta t S_{j,k}^n \end{aligned} \quad (13)$$

$$\begin{aligned} U_{j,k}^{n+1} = \frac{1}{2} (U_{j,k}^n + \overline{U}_{j,k}^{n+1}) - \frac{\Delta t}{2} \left(\frac{G_{k+1} - G_k}{\Delta x} \right)_j^{n+1} \\ - \frac{1}{2} \frac{\Delta t}{r_j} \cdot \frac{2 \Delta r_{j-1}}{\Delta r_j + \Delta r_{j-1}} \cdot \left(\frac{r_{j+1} F_{j+1} - r_j F_j}{\Delta r_j} \right)_k^{n+1} + \frac{\Delta t}{4} (S_j^n + \overline{S}^{n+1})_{j,k} \end{aligned} \quad (14)$$

where overbar denotes "predicted" properties. The main differences from the original MacCormack scheme are in the source terms herein (the original was written for conservation-form differential system), and the special treatment required by the uneven mesh. The "source" terms herein contain the dissipative effects in the system.

Fig. 3 depicts the spatial mesh in the axi-symmetric flowfield. The configuration employs a nonuniform radial mesh distribution, which is very fine near the porous wall ($r=1$) and much coarser near the centerline ($r=0$). The axial mesh is uniform.

The overall configuration of the two steps, (first backward, then forward) when combined, is space-centered. To remain at the second-order accuracy level in the radial direction, for the source or S-terms which involve first and second derivatives, the following finite differencing algorithm is utilized:

$$\frac{\partial Q}{\partial x} \equiv \left(\frac{Q_{k+1} - Q_{k-1}}{2 \Delta x} \right)_j^n ; \quad \frac{\partial^2 Q}{\partial x^2} \equiv \left(\frac{Q_{k+1} - 2Q_k + Q_{k-1}}{\Delta x^2} \right)_j^n \quad (15)$$

$$\frac{\partial Q}{\partial r} \equiv \frac{\Delta r_j \Delta r_{j-1}}{\Delta r_j + \Delta r_{j-1}} \left\{ \frac{Q_{j+1} - Q_j}{\Delta r_j^2} + \frac{Q_j - Q_{j-1}}{\Delta r_{j-1}^2} \right\}_k^n = DQR_{j,k}^n \quad (16)$$

transonic region is outside of the domain of interest for the present system.

The initial data is specified as the following arbitrary (in principle) distributions,

$$U(t=0, r, x) = U^0(r, x) \quad (12)$$

The foregoing formulation is the subject for the numerical OSCO/COLD-FLOW algorithm. Obviously, mathematical closure is obtained when additional boundary data are invoked; this is attained by using the appropriate characteristics relations near the boundaries. The auxiliary boundary data are discussed in the following section.

The radial and axial flux terms are, respectively,

$$\begin{aligned} F^T &= (\rho v, \rho v^2, \rho uv, \gamma \rho h v) \\ G^T &= (\rho u, \rho vu, \rho u^2 + \frac{p}{M_0^2}, \gamma \rho h u) \end{aligned} \quad (7)$$

The source terms are defined as follows. $S_1 = 0$,

$$\begin{aligned} S_2 &= \frac{4/3}{Re_0} \frac{1}{r} \left(\frac{\partial v}{\partial r} - \frac{v}{r} \right) - \frac{1}{\gamma M_0^2} \frac{\partial p}{\partial r} + \\ &\quad \left[\frac{\partial^2 v}{\partial x^2} + \frac{1}{3} \frac{\partial}{\partial r} \left(\frac{\partial u}{\partial x} + 4 \frac{\partial v}{\partial r} \right) \right] \cdot \frac{1}{Re_0} \\ S_3 &= \frac{1/r}{Re_0} \left(\frac{\partial u}{\partial r} + \frac{1}{3} \frac{\partial v}{\partial x} \right) + \\ &\quad \left[\frac{\partial^2 u}{\partial r^2} + \frac{1}{3} \frac{\partial}{\partial x} \left(\frac{\partial u}{\partial x} + \frac{\partial v}{\partial r} \right) \right] \cdot \frac{1}{Re_0} \\ S_4 &= \gamma \left(v \frac{\partial p}{\partial r} + u \frac{\partial p}{\partial x} \right) + \frac{\gamma/p_r}{Re_0} \left(\frac{1}{r} \frac{\partial h}{\partial r} + \frac{\partial^2 h}{\partial r^2} + \frac{\partial^2 h}{\partial x^2} \right) + \\ &\quad \frac{\gamma(\gamma-1)M_0^2}{Re_0} \left\{ \frac{4}{3} \left[\left(\frac{\partial u}{\partial x} \right)^2 + \left(\frac{\partial v}{\partial r} \right)^2 + \left(\frac{v}{r} \right)^2 \right] - \right. \\ &\quad \left. \frac{4}{3} \left[\left(\frac{\partial v}{\partial r} - \frac{v}{r} \right) \frac{\partial u}{\partial x} + \frac{v}{r} \frac{\partial v}{\partial r} \right] + \left(\frac{\partial u}{\partial r} + \frac{\partial v}{\partial x} \right)^2 \right\} \end{aligned} \quad (8)$$

The following physical boundary data are available for the cold-flow simulation problem; on the centerline, $(t, r=0, x)$

$$v=0, \quad \frac{\partial u}{\partial r}=0, \quad \frac{\partial p}{\partial r}=0, \quad \frac{\partial h}{\partial r}=0 \quad (9)$$

at the injected porous surface, $(t, r=1, x)$

$$v = -v_0(x, t), \quad u=0, \quad h=h_w(x, t) \quad (10)$$

at the nonpermeable, solid head-end, $(t, r, x=0)$

$$v=0, \quad u=0, \quad h=h_H(r, t) \quad (11)$$

The exit plane, defined by $(t, r, x=L)$, forms an entrance into a short convergent nozzle section, assumed choked at all times; detailed description of the nozzle entrance and its inherent

2.2 FORMULATION OF THE DIFFERENTIAL SYSTEM

The four equations of motion pertain to compressible, viscous, nonsteady motions in an axisymmetric flowfield. The system is written in differential form, employing source terms to represent the various dissipative effects.

The following dimensionless independent variables are introduced,

$$r = r^*/R_0^*, \quad x = x^*/R_0^*, \quad t = t^*/t_0^* \quad (1)$$

where $t_0^* = R_0^*/v_0^*$.

The corresponding dependent variables are:

$$V = v^*/v_0^*, \quad u = u^*/v_0^* \\ \rho = \rho^*/\rho_0^*, \quad h = h^*/h_0^*, \quad p = p^*/p_0^* \quad (2)$$

The properties used for non-dimensionalization are the injection velocity, the reference gas density, and the reference chamber pressure. The corresponding thermal enthalpy, h_0 , is calculated from the caloric equation of state,

$$p_0^* = \frac{\gamma-1}{\gamma} \rho_0^* h_0^* ; \quad p = \rho h \quad (3)$$

where $\gamma = C_p/C_v$ is considered a constant. The reference adiabatic speed of sound is,

$$a_0^* = (\gamma p_0^*/\rho_0^*)^{1/2} = \sqrt{(\gamma-1)h_0^*} \quad (4)$$

The corresponding injection Mach number, Reynolds and Prandtl numbers are, respectively,

$$M_0 \equiv v_0^*/a_0^*$$

$$Re_0 \equiv \rho_0^* v_0^* R_0^*/\mu^*, \quad Pr \equiv \mu^* c_p^*/\lambda^* \quad (5)$$

Thus, the dimensionless differential system can be written in general, for $0 < x < L$, $0 < r < 1$, and $t > 0$:

$$\frac{\partial}{\partial t} + \frac{1}{r} \frac{\partial}{\partial r}(rF) + \frac{\partial G}{\partial x} = S \quad (6)$$

and the dependent variable vector is:

$$U^T = (\rho, \rho v, \rho u, p = \rho h)$$

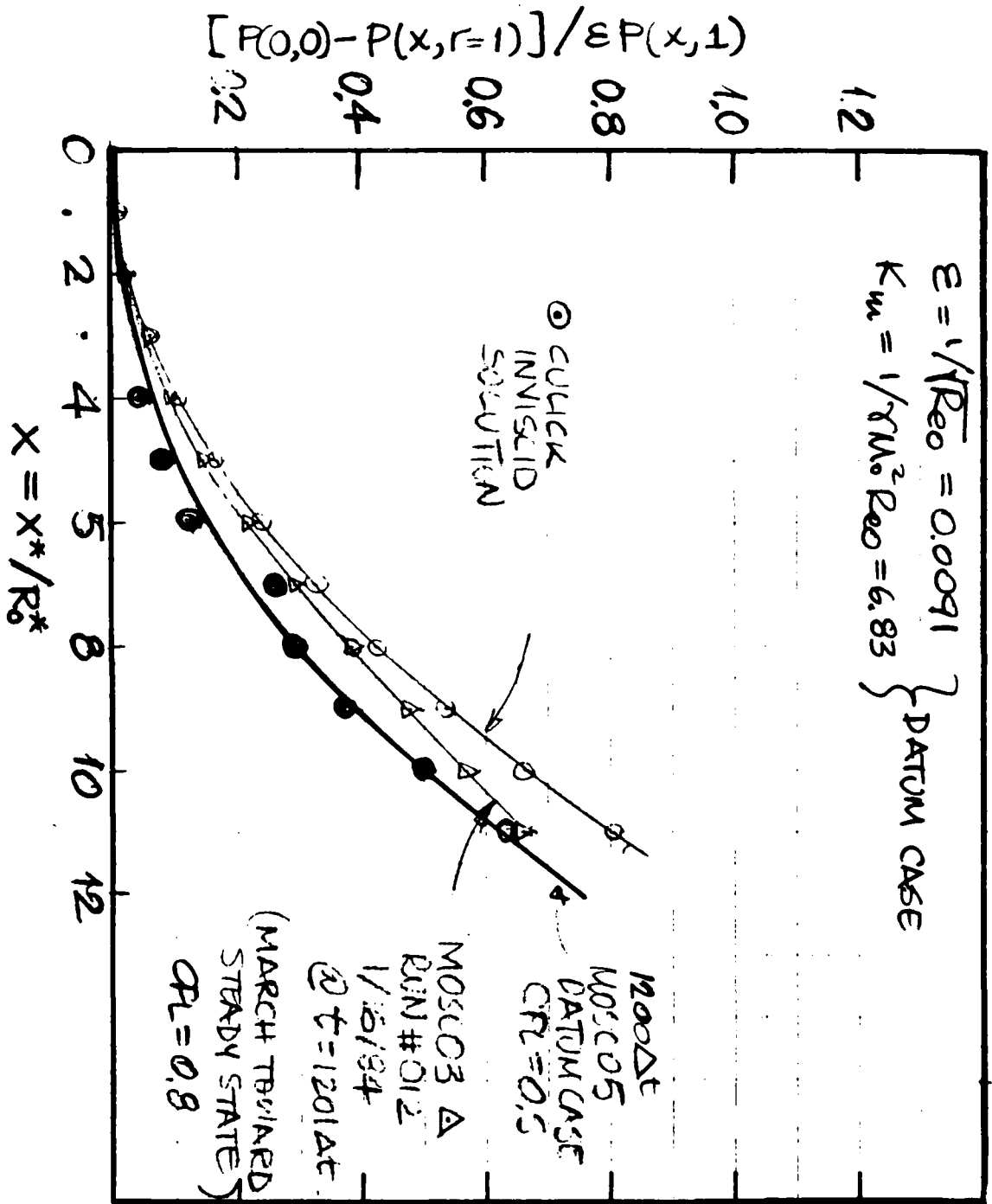


FIG. 2.4

AXIAL PRESSURE-DROP

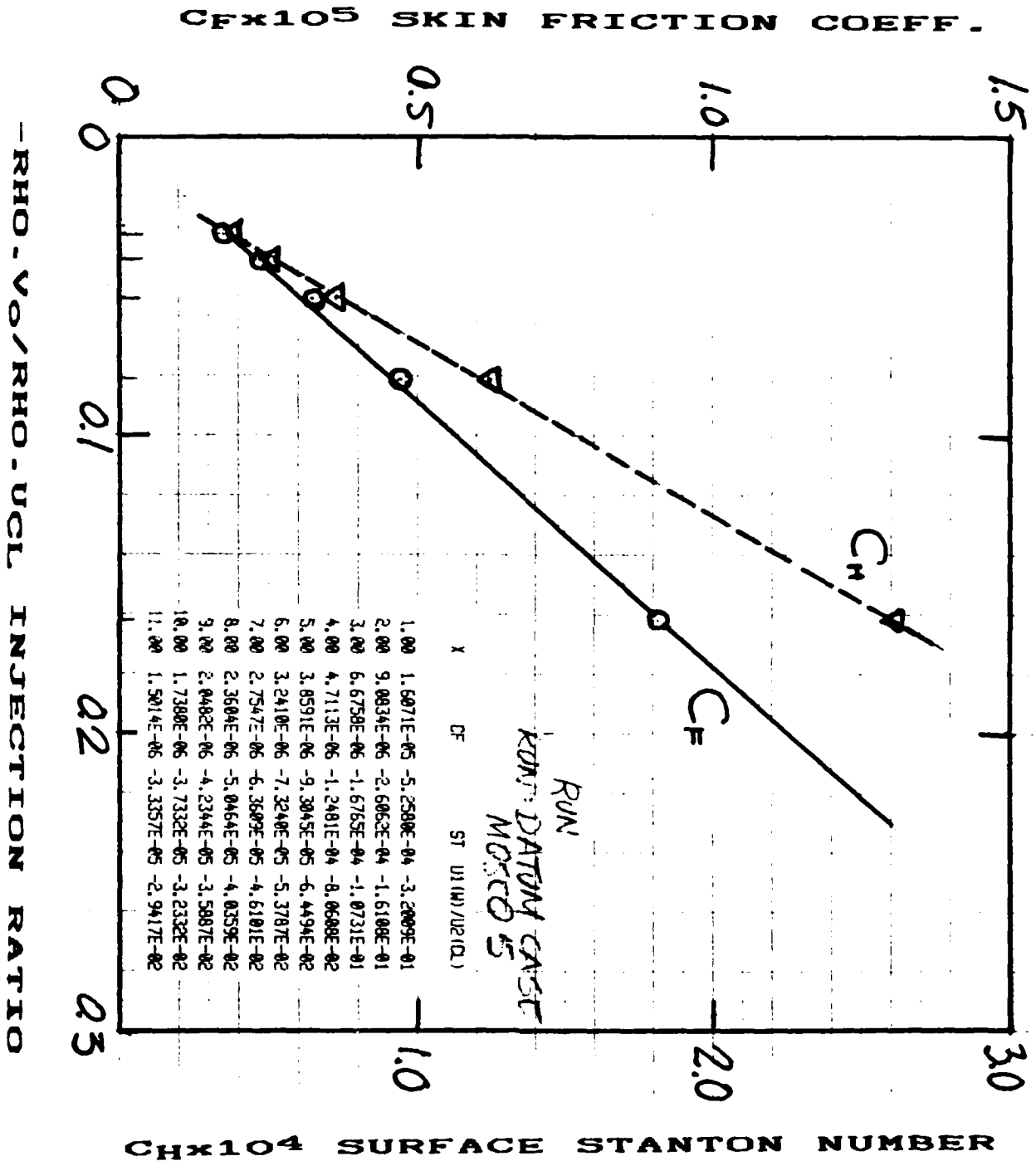
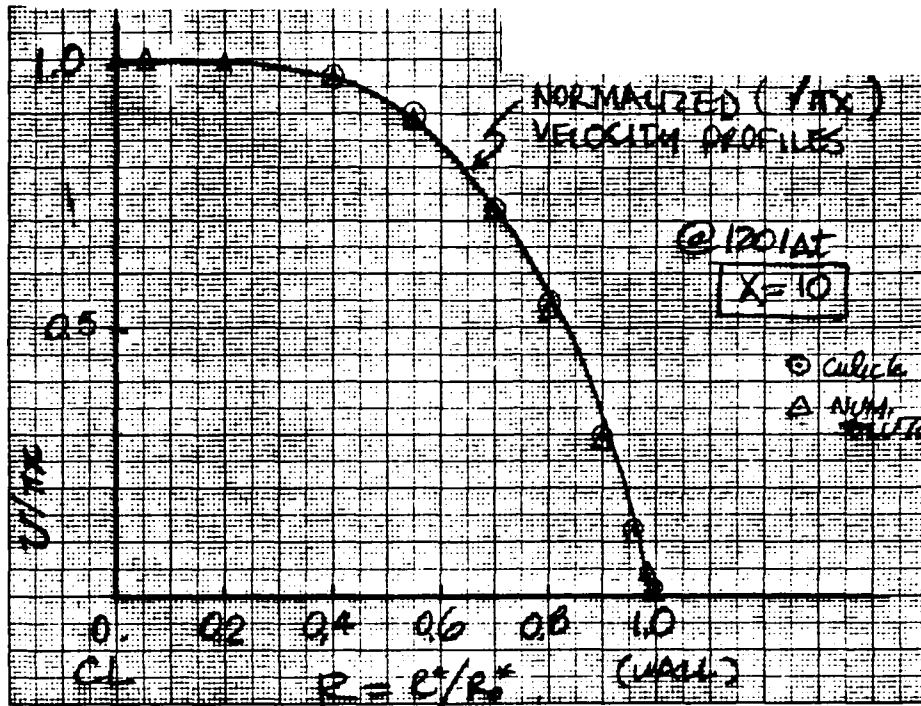
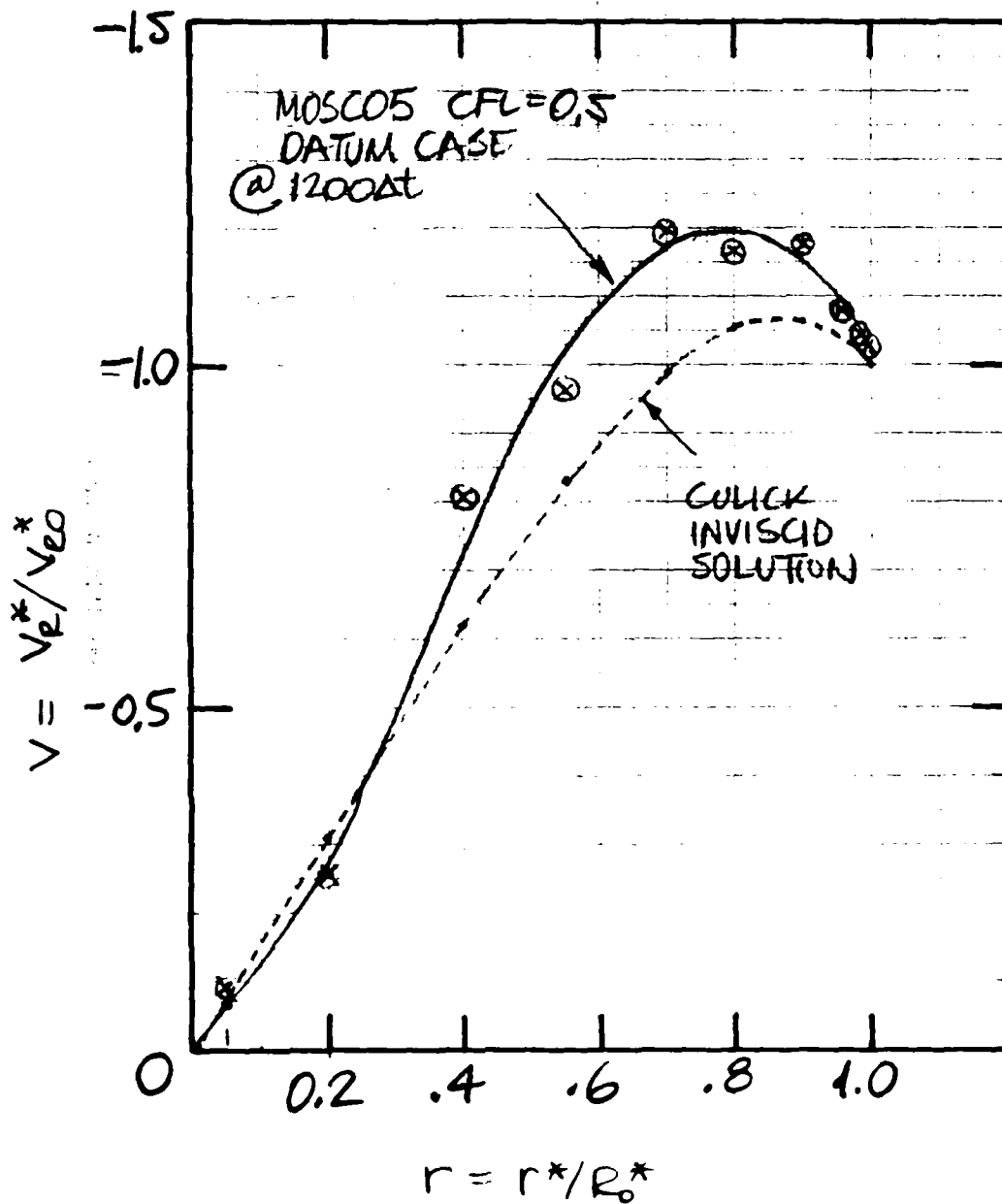


FIG 2.7



RADIAL DISTRIBUTION OF
AXIAL VELOCITY

FIG. 2.6



RADIAL VELOCITY PROFILE

FIG. 2.7

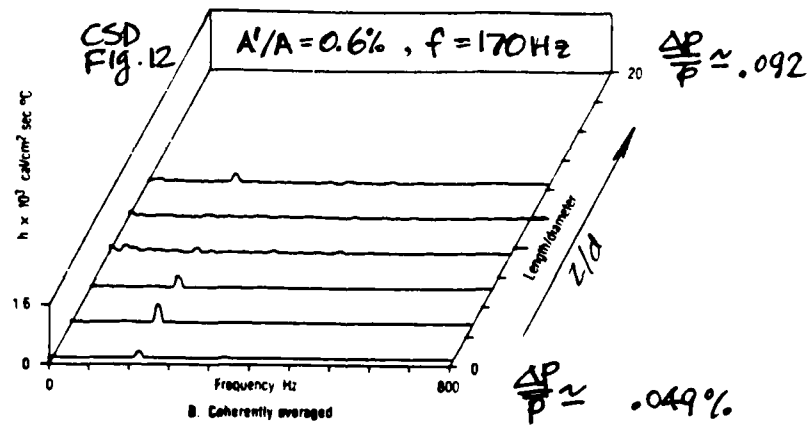
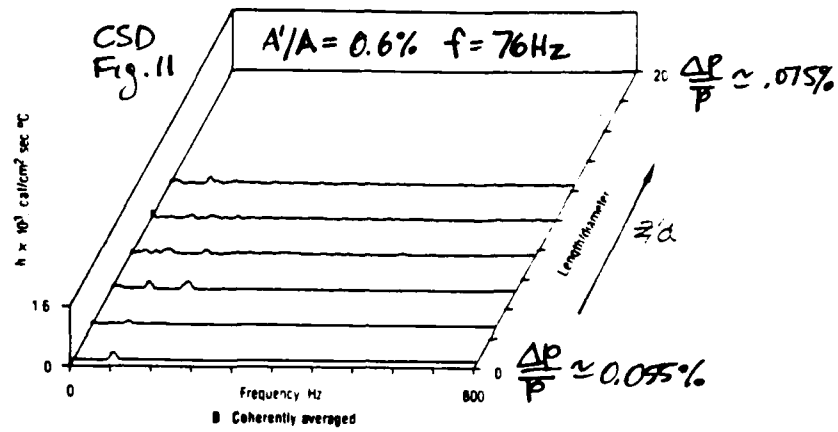


FIG. 2.8

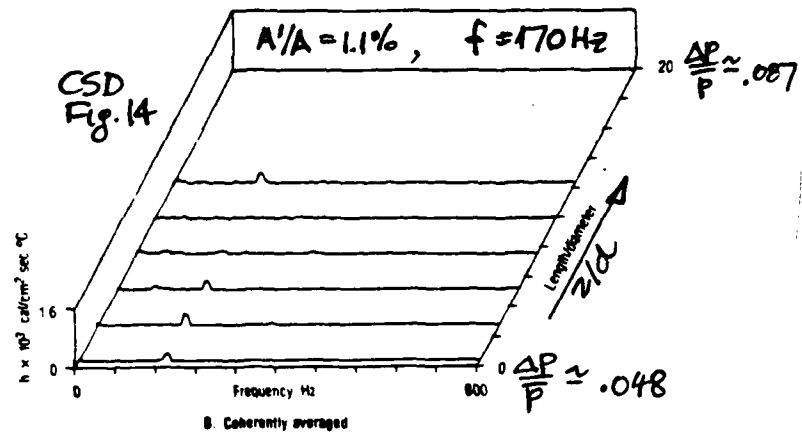
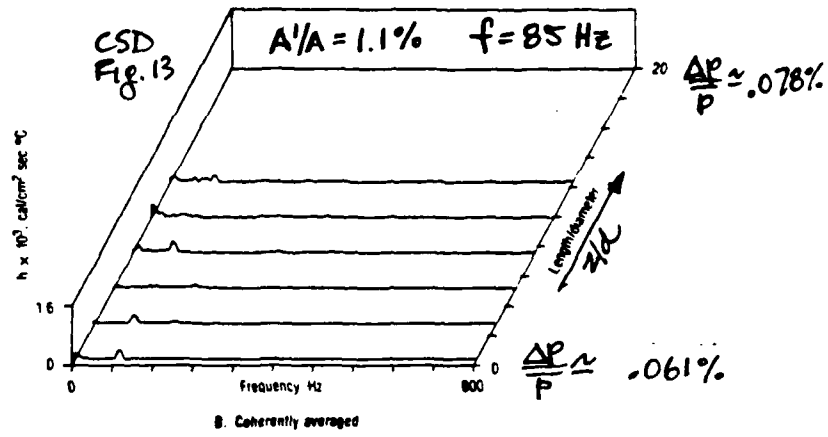


FIG. 2.9

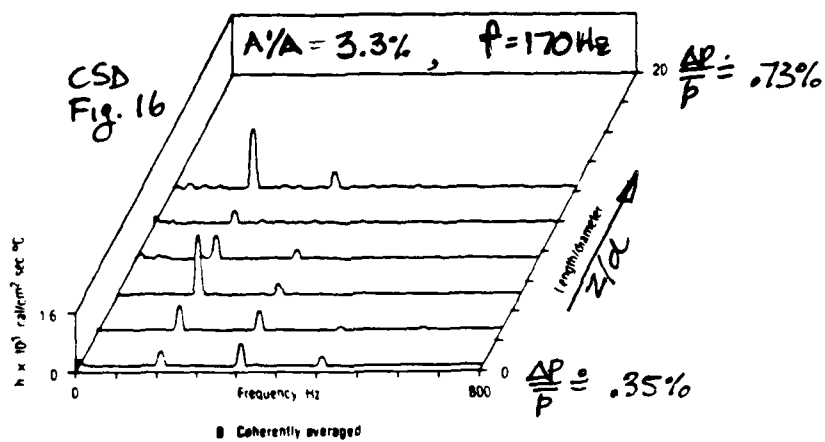
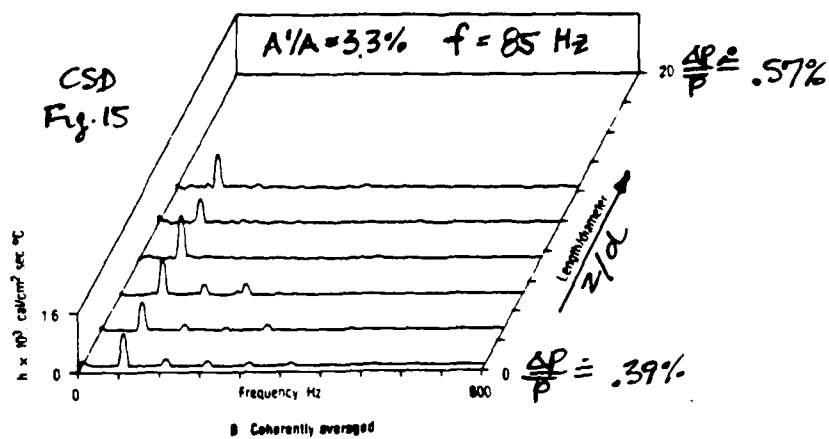


FIG. 2.10

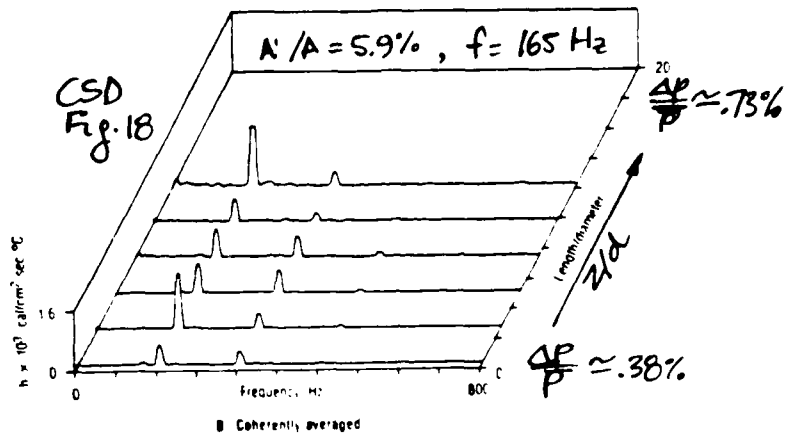
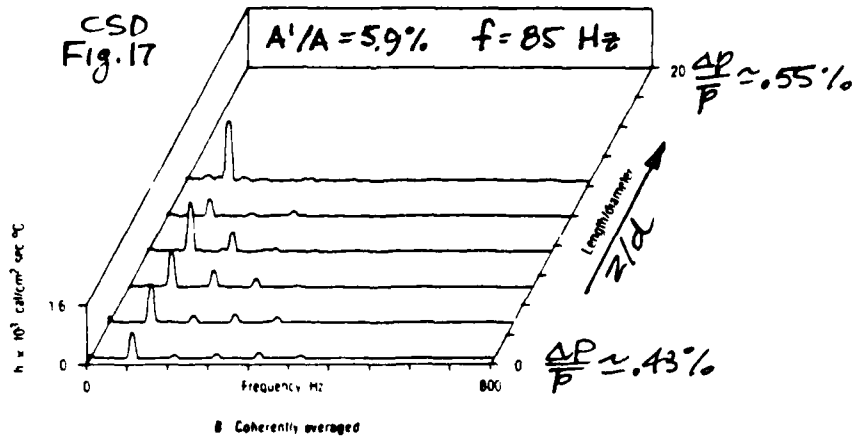


FIG. 2.11

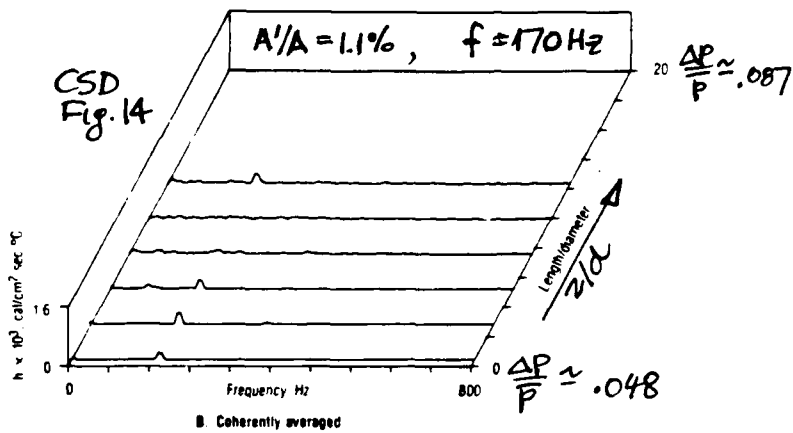
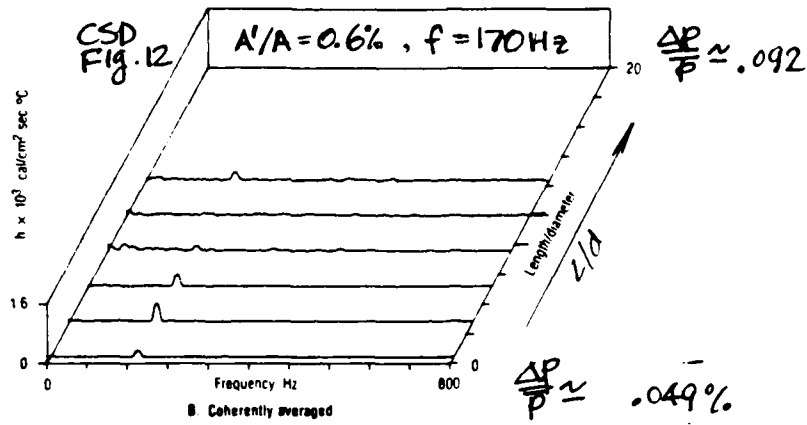
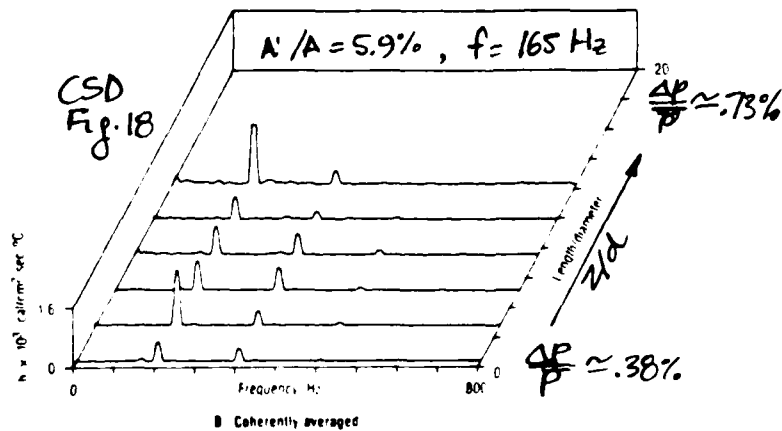
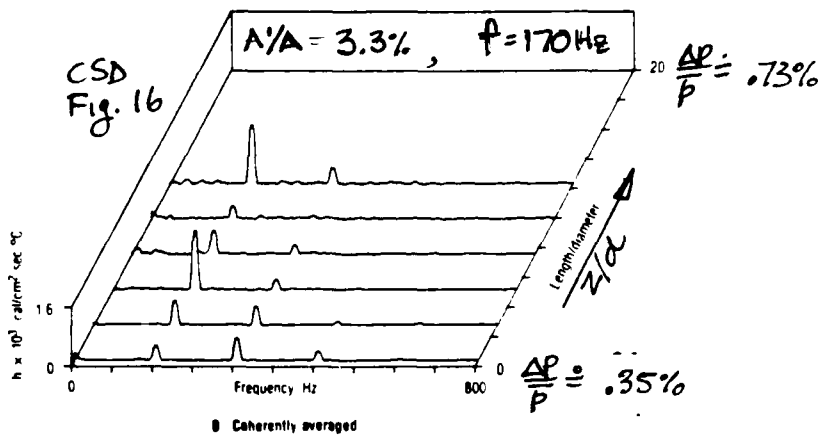


FIG. 2.12



3. USER'S MANUAL for "MOSCO" COLD FLOW SIMULATION PROGRAM

3.1 INPUT DESCRIPTION

3.1.1 BLOCK DATA Statement

```

BLOCK DATA
COMMON/AREA0/VZERO, PSTAR, TSTAR, VISC, COND, WBAR, RUJ, HSTAR, CP,
+CFL, RSTAR, XSTAR, XO, IPRT1, IPRDT(2), ICORR(2), INC(3), ITMAX, VO, PO, RO
COMMON/AREA1/GAMA, GAM1, GAM2, GAM3, GAM3T, C61, C62, C63, C64, C65,
+REO, EMO, EMO2, PI, PIT, EKM, RHOG, SSND, PRN, DX, TODX, DX2, RR(26), DRR(25),
+R2(26), R3(26), XX(26), DT, EPS
COMMON/AREA2/MXX, JRR, KXX, JRM1, KXM1, KXPR(6), KXPMA, JRPR(6),
+JRPMA, D6X(4,26,26), DFR(4,26,26), VIC(4,26,26), HMO, HMP, RRS, RSM1
DATA COND, PSTAR, RSTAR, XSTAR, GAMA, CFL/.0166, 2.00E5, .05, .55, 1.4, .5/
DATA VZERO, VISC, TSTAR, WBAR, RUJ/1.000, 1.E-5, 278., .028, 8.314/
DATA JRPMA, JRPR, JRR/6, 1, 3, 5, 7, 9, 11, 12/
DATA KXPMA, KXPR, KXX/6, 1, 3, 5, 7, 9, 11, 12/
DATA VO, PO, RO/1.0000, 1.0000, 1./, ITMAX, IPRT1/1201, 200/
DATA IPRDT, ICORR, INC/-1, 0, 0, 1, -1, 0, 1/, MXX/4/
DATA DRR/.05, .15, .2, .15, .15, .1, .1, .06, .025, .01, .005, 14*0./
END

```

All of the input enters through the BLOCK DATA statement, and transmitted to the remainder of the program through the labelled Common Blocks.

Throughout the program, all dimensional parameters are in SI units. The integration itself is carried out with dimensionless variables; suitable transformation of the differential system has been made, prior to utilization of the finite difference algorithm herein.

The seven input data lines are discussed in the following glossary.

Line 1

COND = thermal conductivity, J/m-s-R of the gas (air)
PSTAR = reference pressure, N/m²
RSTAR = inner radius, m
XSTAR = axial length, m
GAMA = ratio of specific heats, C_A/C_V
CFL = Courant-Friedricks-Lewy number

Line 2

VZERO = injection velocity, m/sec
VISC = viscosity coefficient, Kg/m-s
TSTAR = ref. temperature of gas, K
WBAR = mean molecular weight of gas, kg/mol
RUJ = universal gas constant, J/mol-K

Line 3

JRPMAX = total number of points to print out in radial mapping (see output)
JRPR = radial position vector; numbers correspond to distinct radial stations, and their total number should agree with JRPMAX.
JRP = maximum number of meshpoints in radial direction (including ends)

Line 4

KXPMAX = (same as JRPMAX) total number of axial points in printout of axial maps
KXPR = axial position vector; axial mesh indices of points to be printed out; total number should be equal to KXPMAX
KXX = maximum number of axial mesh points, including boundaries

Line 5

VO = dimensionless (absolute) injection velocity
PO = dimensionless reference pressure
RO = dimensionless inner channel radius
ITMAX = total number of timewise integration steps
allowed
IPRNT1 = number of timewise integration steps between
output

Line 6

IPRDT = predictor step, index displacement vector
(backward differences), used in DGDY and DFDR
ICORR = same as above, for corrector step (forward
differences)
INC = index shift vector for the central-difference
algorithms of SORCE subprogram

Line 7

DRR = radial increment, starting with increment near
centerline, and ending with that near the wall
(last)

NOTE: DRR is dimensioned to 26 and empty places
above 12 must be padded with zeros.

CAUTION: Performance of the program is quite
sensitive to (small, required) step size near
wall.

This concludes the entire input data set.

3.2 MAIN

```

C---MBR VERSION OF MACCORMACK INTEGRATION SCHEME.12/9/83
C---FIRST TRIAL:UNPLIT, SINGLE PREDICTOR/CORRECTOR CYCLE EACH DT.
C---VARIABLE RADIAL STEPSIZE. ARBITRARY DR(J)=INPUT VECTOR.
COMMON/AREA0/VZERO, PSTAR, TSTAR, VISC, COND, WBAR, RUJ, HSTAR, CP,
+CF, RSTAR, XSTAR, X0, IPRNT1, IPRDT(2), ICORR(2), INC(3), ITMAX, V0, PG, R0
COMMON/AREA1/GAMA, GAM1, GAM2, GAM3, GAM3T, C61, C62, C63, C64, C65,
+REQ, EMO, EMO2, P1, PIT, EXM, RHOG, SSND, PRN, DX, TODX, DX2, RR(26), DRR(25),
+R2(26), R3(26), XX(26), DT, EPS
COMMON/AREA2/MXX, JRR, KXX, JRM1, KX1, KXPR(6), KXPMAX, JRPR(6),
+JRPMAX, D6X(4,26,26), DFR(4,26,26), VIC(4,26,26), HMO, HMF, RRS, RSM1
COMMON/AREA3/U(4,12,12), UB(4,12,12), S(4,12,12), SB(4,12,12)
TIME=0.
CALL SDATA
K=0
DO 1 L=1,ITMAX
IF(K.LT.IPRNT1)GO TO 2
CALL PRINT2(TIME,L)
K=K+1
2 CONTINUE
CALL TIMINT1(MXX,JRR,KXX,TIME,DT)
K=K+1
1 CONTINUE
STOP2222
END

```

The MAIN program just calls for calculation of the fixed parameters and the initial data profiles, all in subroutine SDATA. Then, in Do-loop #1 timewise integration is called out each timestep, by calling subroutine TIMINT. Printing of the variable tables of interest is made by calls to subroutine PRINT, each preselected number of timesteps: the integer IPRINT1 controls the number of timesteps between such output dumps.

3.3 TIME-INTEGRATION PROCEDURE

3.3.1 Subroutine TIMINT

```

SUBROUTINE TIMINT(MF,JF,KF,TIME,DT)
C-----MFR VERSION OF UNSPLIT MACCORMACK TIME MARCHING. 12/9/83.
COMMON/AREA0/VZERO,PSTAR,TSTAR,VISC,COND,WBAR,RUI,HSTAR,CP,
+ CFL,RSTAR,XSTAR,XD,IPRNT1,IPRDT(2),ICORR(2),INC(3),ITMAX,VO,PO,RO
COMMON/AREA2/MXX,JRR,KXX,JRM1,KXM1,KXPR(6),KXPMAX,JRPR(6),
+ JRPMAX,DSX(4,26,26),DFR(4,26,26),VIC(4,26,26),HWD,HWP,RRS,RSM1
COMMON/AREA3/U(4,12,12),UB(4,12,12),S(4,12,12),SB(4,12,12)
C-----PREDICTOR STEP
CALL DFDR(MF,JF,KF,U,2,IPRDT)
CALL DGDY(MF,JF,KF,U,2,IPRDT)
CALL SORCE1(MF,JF,KF,U,S)
DO 6 M=1,MF
DO 6 J=2,JRM1
DO 6 K=2,KXM1
6 UB(M,J,K)=U(M,J,K)-DT*(DFR(M,J,K)+DGY(M,J,K)-S(M,J,K))
C-----CORRECTOR STEP
CALL BNDY(MF,JF,KF,UB)
CALL DFDR(MF,JF,KF,UB,2,ICORR)
CALL DGDY(MF,JF,KF,UB,2,ICORR)
CALL SORCE1(MF,JF,KF,UB,SB)
DO 7 M=1,MF
DO 7 J=2,JRM1
DO 7 K=2,KXM1
U(M,J,K)=(U(M,J,K)+UB(M,J,K))/2.-.5*DT*(DFR(M,J,K)+DGY(M,J,K)
- (S(M,J,K)+SB(M,J,K))/2.)
7 CONTINUE
CALL BNDY(MF,JF,KF,U)
TIME=TIME+DT
RETURN
END

```

Subroutine TIMINT carries out the timewise integration process for the unsplit MacCormack scheme. The Predictor step involves calculation of the radial and axial flux terms, based on backward-differences: this is carried out for the entire interior of the physical field by calls to subprograms DFDR and DGDY, respectively. The integer vector IPRDT=(-1,0) controls the backward differencing. A call to subroutine SORCE establishes the "source" terms, involving dissipative effects. The second order differential terms are discretized as central differences in subroutine SORCE. Subsequent to these calls, the entire dependent-variable (predicted) vector, UB, is calculated in Do-loop #6.

Continued

```

RHOG=PSTAR*WBAR/(RUJ*TSTAR)
SSND=(GAMA*PSTAR/RHOG)**.5
REO=RHOG*VZERO*ASTAR/VISC
EPS=1./SQRT(REO)
EMO=VZERO/SSND
EMO2=EMO**2
XO=XSTAR/RSTAR
GAM1=GAMA-1.
GAM2=GAM1/GAMA
GAM3=GAMA*EMO2
GAM3T=GAM3/2.
CG1=1./GAM3
CG2=4./3./REO
CG3=1./REO
CG5=GAM1*GAM3/REO
EKM=1./(GAM3*REO)
HSTAR=PSTAR/(GAM2*RHOG)
CP=HSTAR/TSTAR
PRN=VISC*CP/COND
CG4=GAMA/REO/PRN
JRM1=JRR-1
KXM1=KXX-1
MXM1=MX-1
DX=XO/KXM1
TODX=2.*DX
DX2=DX*DX

```

Continued

The first group of parameters calculated are as follows.

RHOG	ref. gas density, kg/m ³
SSND	ref. adiabatic speed of sound in gas, m/sec
REO	injection Reynolds number, based on the injection velocity and the chamber radius.
EPS	the small parameter pertaining to viscous effects
EMO	injection Mach number
XO	dimensionless axial length
EKM	second dimensionless parameter denoting the ratio of inertial to viscous effects: K_m in the analysis of Appendix A.
HSTAR	ref. specific thermal enthalpy, J/kg
CP	ref. specific heat, isochoric, J/kg-K
PRN	Prandtl number
GAM**	constant parameters associated with gamma, the ratio of specific heats.
CG**	constant parameters associated with Reynolds number

3.5 SUBROUTINE SDATA - CALCULATION OF CONSTANT PARAMETERS AND
THE INITIAL DATA

```
SUBROUTINE SDATA
  DIMENSION VR(26), VX(26)
  LOGICAL DIFFPR
  COMMON/AREAD/VZERO, PSTAR, TSTAR, VISC, COND, WBAR, RUJ, HSTAR, CP,
+ CFL, RSTAR, XSTAR, XO, IPRT1, IPRDT(2), ICORR(2), INC(3), ITMAX, VO, PO, RB
  COMMON/AREA1/GAMA, GAM1, GAM2, GAM3, GAM3T, C61, C62, C63, C64, C65,
+ REQ, EMO, EMO2, PI, PIT, EKM, RHOG, SSND, PRN, DX, TODX, DX2, RR(26), DRR(25),
+ R2(26), R3(26), XX(26), DT, EPS
  COMMON/AREA2/MXX, JRR, KXX, JRM1, KXM1, KXPR(6), KXPMAX, JRPR(6),
+ JRPMAX, DGX(4, 26, 26), DFR(4, 26, 26), VIC(4, 26, 26), HWD, HWP, RRS, RSM1
  COMMON/AREA3/U(4, 12, 12), UB(4, 12, 12), S(4, 12, 12), SB(4, 12, 12)
  COMMON/AREA4/DIFFPR
```

Continued

All of the information calculated herein is passed to the
remainder of the program through the labelled common blocks.

Continued

3.4.2 Subroutines XPRNT1 and XPRNT2

```

SUBROUTINE XPRNT1(MF,JF,KF,UP,ZX,ZY)
  DIMENSION UP(MF,JF,26),ZX(JF),ZY(26)
101  FORMAT(/,2X,'RHO = DIM. LESS DENSITY')
      WRITE(6,101)
      WRITE(6,102)(ZX(N),N=1,JF)
      DO 1 K=1,KF
1      WRITE(6,103)ZY(K),(UP(1,J,K),J=1,JF)
104  FORMAT(/,2X,'VR = DIM. LESS RADIAL VELOCITY')
      WRITE(6,104)
      WRITE(6,102)(ZX(N),N=1,JF)
      DO 2 K=1,KF
2      WRITE(6,103)ZY(K),(UP(2,J,K),J=1,JF)
105  FORMAT(/,2X,'VX = DIM. LESS AXIAL VELOCITY')
      WRITE(6,105)
      WRITE(6,102)(ZX(N),N=1,JF)
      DO 3 K=1,KF
3      WRITE(6,103)ZY(K),(UP(3,J,K),J=1,JF)
106  FORMAT(/,2X,'P = DIM. LESS STATIC PRESSURE')
      WRITE(6,106)
      WRITE(6,102)(ZX(N),N=1,JF)
      DO 4 K=1,KF
4      WRITE(6,103)ZY(K),(UP(4,J,K),J=1,JF)
102  FORMAT(6X,'YZ',6(2X,'XZ=',F7.4))
103  FORMAT(2X,F6.3,5(1PE12.4))
      RETURN
END

```

```

SUBROUTINE XPRNT2(ST,CF,FLX,XX,KXX)
  DIMENSION ST(KXX),CF(KXX),FLX(KXX),XX(KXX)
  WRITE(6,201)
201  FORMAT(/,2X,'SKIN FRICTION(CF) & STANTON NO. (ST)',/)
      WRITE(6,202)
202  FORMAT(6X,'X',8X,'CF',10X,'ST',2X,'U1(W)/U2(CL)',/)
      DO 204 I=2,KXX
      WRITE(6,203)XX(I),CF(I),ST(I),FLX(I)
204  CONTINUE
203  FORMAT(2X,F5.2,5(1PE12.4))
      RETURN
END

```

```

C-----NOTE: THE VR AND DVR ARRAYS ARE TRANSPOSED (ROTATED ABOUT THE
C-----MAJOR AXIS) RELATIVE TO THE PARENT U-ARRAY. THIS IS ONLY FOR
C-----PRINTOUT REASONS
      WRITE(6,90)TIME,L
C-----X-MAPS
      WRITE(6,100)
      CALL XPRNT1(MXX,JRPMAX,KXX,VX,RP,XX)
      IF(DIFFPR)GO TO 5000
      WRITE(6,201)L
      WRITE(6,100)
      CALL XPRNT1(MXX,JRPMAX,KXX,DVX,RP,XX)
      CALL XPRNT2(ST,CF,FLX1,XX,KXX)
C-----R-MAPS
5000  WRITE(6,200)
      CALL XPRNT1(MXX,KXPMAX,JRR,VR,XP,RR)
      IF(DIFFPR) GO TO 5001
      WRITE(6,201)L
      WRITE(6,200)
      CALL XPRNT1(MXX,KXPMAX,JRR,DVR,XP,RR)
5001  CONTINUE
100   FORMAT(/,2X,'X-MAP, AT DISTINCT RADIAL POSITIONS',/,1X,75(' '),/)
200   FORMAT(/,2X,'R-MAP, AT DISTINCT AXIAL POSITIONS',/,1X,75(' '),/)
201   FORMAT(/,2X,'DIFFERENCES BETWEEN CURRENT TIMESTEP NO.',I4,/,2X,
*AND THE INITIAL DATA  U(M,J,K)-UINITIAL(M,J,K) :' )
90    FORMAT(/,2X,'TIME =',1PE12.4,5X,'TIMESTEP NO. =',I4,/)
      RETURN
      END

```

For ease of carrying out the printing, the radial maps VR(J,K) and DVR(J,K) are transposed (rotated about the major axis); this allows use of exactly the same printout procedure in subroutine XPRNT1, for both axial and radial variable maps. Following the appropriate Table Header printouts, the four consecutive calls to subroutine XPRNT1 affect printout, with four table groups, each containing four single tables (one for each variable). The call to subroutine XPRNT2 affects printout of the friction coefficient and Stanton number Table, following the X-maps.

Note that the length of each table is not limited; the only self-imposed format limitation used in the design is the compatibility with a printer page width of 80 columns. Consequently, there is no attempt to fit printout groups into any particular page length.

```
DO 2000 J=1,JRR
DO 2000 K=1,KXPMAX
KK=KXPR(K)
RHO=U(1,J,KK)
VR(1,K,J)=RHO
VR(2,K,J)=U(2,J,KK)/RHO
VR(3,K,J)=U(3,J,KK)/RHO
VR(4,K,J)=U(4,J,KK)
XP(K)=XX(KK)
DO 2100 M=1,MXX
2100 DVR(M,K,J)=VR(M,K,J)-VIC(M,J,KK)
IF(KK.GT.1)GO TO 2200
DVR(3,1,J)=0.
GO TO 2000
2200 DVR(3,K,J)=DVR(3,K,J)/(PI*XP(K))
2000 CONTINUE
```

Continued

A similar procedure is carried out within Do-loop #2000, for the radial printout map, VR, and its corresponding difference-map, DVR. Distinct axial positions are now used, as specified in the integer vector KXPR, again with an imposed maximum of 6 positions; for each of these, the radial dependent variable distributions are printed out, with XP denoting the corresponding normalized, distinct axial stations. Note that in this instance the radial pressure difference map (not normalized) is calculated instead of the aforementioned axial pressure drop.

Continued

```

C—— LOAD X-MAP ARRAYS
DO 1000 K=1,KXX
DO 1000 J=1,JRPMAX
JJ=JRPR(J)
RHO=L(1,JJ,K)
VX(1,J,K)=RHO
VX(2,J,K)=U(2,JJ,K)/RHO
VX(3,J,K)=U(3,JJ,K)/RHO
VX(4,J,K)=U(4,JJ,K)
RP(J)=RR(JJ)
MXM=MXM-1
DO 1100 M=1,MXM
1100 DVX(M,J,K)=VX(M,J,K)-VIC(M,JJ,K)
DVX(4,J,K)=(VX(4,1,1)-VX(4,J,K))/(VX(4,J,K)*EPS)
IF(K.GT.1)GO TO 1200
DVX(3,J,1)=0.
GO TO 1000
1200 DVX(3,J,K)=DVX(3,J,K)/(PI*XX(K))
1000 CONTINUE

```

Continued

In Do-loop #1000, the primitive dependent variable array VX is calculated (still dimensionless), namely, the axial and radial fluxes are replaced by the respective velocities. The purpose is to create an X-map, in which the full axial distributions of each variable are printed, at distinct, preselected radial positions; up to 6 such distinct radial positions are available with the current setup, to facilitate printing with an 80-column nominal page width. The integer vector JRPR stores the distinct radial positions to be printed; RP denotes the radial position values, normalized.

In the nested Do-loop #1100 the difference array DVX (departure from initial data) is calculated, for the density and the two velocities; the fourth variable calculated therein is the dimensionless axial pressure drop, normalized by the small parameter epsilon (EPS). The axial velocity difference is normalized by $PI \cdot X$, to factor out the linear growth (due to accumulated injection) along the axis.

3.4 OUTPUT SECTION

3.4.1 Subroutine PRINT

```

SUBROUTINE PRINT2(TIME,L)
  DIMENSION VX(4,6,26),DVX(4,6,26),XP(6),VR(4,6,26),DVR(4,6,26)
  + ,RP(6),ST(26),CF(26),FLXI(26)
  COMMON/AREAD/VZERO,PSTAR,TSTAR,VISC,COND,WBAR,RWJ,HSTAR,CP,
  +CFL,RSTAR,XSTAR,XD,IPRNT1,IPRNT2,ICORR(2),INC(3),ITMAX,VO,PO,RO
  COMMON/AREA1/GAMA,GAM1,GAM2,GAM3,GAM3T,C61,C62,C63,C64,C65,
  +REQ,EMO,EMD2,P1,PIT,EKM,RHOG,SSND,PRN,DX,TODX,DX2,RR(26),DRR(26),
  +R2(26),R3(26),XX(26),DT,ERS
  COMMON/AREA2/MXX,JRR,KXX,JRM1,KXM1,KXPR(6),KXPMAX,JRRP(6),
  +JRPMAX,DGX(4,26,26),DFR(4,26,26),VIC(4,26,26),HMO,HMP,RRS,RSM1
  COMMON/AREA3/U(4,12,12),UB(4,12,12),S(4,12,12),SB(4,12,12)
  COMMON/AREA4/DIFFPR
  LOGICAL DIFFPR
C-----CALCULATION OF SKIN FRICTION & STANTON NUMBER
  DO 500 K=2,KXX
    RHO1=U(1,JRM1,K)
    WALLH=U(4,JRR,K)/U(1,JRR,K)
    CENH=U(4,1,K)/U(1,1,K)
    CF(K)=VISC*U(3,JRM1,K)/(RHO1*DRR(JRM1))/(.5*U(3,1,K)**2/U(1,1,K))
    ST(K)=-COND/CP*(U(4,JRM1,K)/RHO1-WALLH)/DRR(JRM1)
    IF(CENH.EQ.WALLH)GO TO 500
    ST(K)=ST(K)/(U(3,1,K)*(CENH-WALLH))
    FLXI(K)=U(2,JRR,K)/U(3,1,K)
500  CONTINUE

```

Continued

Subroutine PRINT loads the output maps, calls for their actual printing (through subroutines XPRNT1 and XPRNT2), and prints the header for each output table.

Skin friction coefficient (CF) and heat transfer coefficient (ST, Stanton number) at the porous injected sidewalls are calculated first, using 2-point differencing. The resulting CF and ST vectors will be printed out through subroutine XPRNT2, vs the axial injection (mass flux) ratio, FLXI, also calculated herein.

Continued

3.3.5 Subroutine BNDRY

```

SUBROUTINE BNDRY(MF,JF,KF,W)
  DIMENSION U(MF,JF,KF)
  COMMON/AREA2/MXX,JRR,KXX,JRM1,KXM1,KXPR(6),KXPMAX,JRPR(6),
    +JRPMAX,DGX(4,26,26),DFR(4,26,26),VIC(4,26,26),HMD,HMP,RRS,RSM1
C--- MBR-VERSION OF BOUNDARY DATA TREATMENT. 12/13/83
C--- CENTERLINE, R=0. NOTE: U2=0 ALWAYS.
C--- DU1/DR=DU3/DR=DU4/DR=0 TO MAINTAIN AXIAL SYMMETRY.
  DO 1 K=2,KXX
    U(1,1,K)=U(1,2,K)
    U(3,1,K)=U(3,2,K)
    1 U(4,1,K)=U(4,2,K)
C--- POROUS SURFACE: PRESSURE EXTRAPOLATED. WALL ENTHALP=HMP.
  DO 3 K=2,KXX
    U(4,JRR,K)=(RRS*U(4,JRM1,K)-U(4,JRM1-1,K))/RSM1
    3 U(1,JRR,K)=U(4,JRR,K)/HMP
C--- HEAD END: X=0. NOTE: U2=0 AND U3=0, ALWAYS. WALL TEMP.=HMF(R).
  DO 2 J=1,JRM1
    U(4,J,1)=U(4,J,2)*2.-U(4,J,3)
    U(1,J,1)=U(4,J,1)/HMD
    DO 2 M=1,MXX
      U(M,J,KXX)=U(M,J,KXM1)*2.-U(M,J,KXM1-1)
    2 CONTINUE
  RETURN
  END

```

Subroutine BNDRY is called following the predictor and the corrector steps, from subroutine TIMINT. The mode of operation is fully explained in the previous chapter of this manual.

3.3.4 Special Functions

```
FUNCTION DDZ(A,B,D)
  DDZ=(B-A)/D
  RETURN
END

FUNCTION DDR2(A,B,C,D1,D2)
C---SECOND DERIVATIVE FINITE DIFF.--NONUNIFORM MESH.
  DDR2=2.*(DDZ(B,C,D2)-DDZ(A,B,D1))/(D1+D2)
  RETURN
END

FUNCTION CDX2(A,B,C,D2)
C---SECOND DERIVATIVE FINITE DIFF.--UNIFORM MESH, CENTRAL DIFF.
  CDX2=(A-2.*B+C)/D2
  RETURN
END

FUNCTION DBAR(A,B,C,D1,D2)
  DBAR=(D2*DDZ(A,B,D1)+D1*DDZ(B,C,D2))/(D1+D2)
  RETURN
END

FUNCTION DDRX1(MF,Q,D1,D2,DXT)
C---MIXED-UP SECOND DERIV., UNIFORM X, NON-UNIFORM R.
  DIMENSION Q(MF,MF)
  DU1=DDZ(Q(1,1),Q(1,3),DXT)
  DU2=DDZ(Q(2,1),Q(2,3),DXT)
  DU3=DDZ(Q(3,1),Q(3,3),DXT)
  DDRX1=DBAR(DU1,DU2,DU3,D1,D2)
  RETURN
END
```

C---LIBRARY OF FINITE DIFFERENCE FUNCTIONS:

```

D2VDX=DDZ(VT(2,1),VT(2,3),TODX)
D2UDX=DDZ(UT(2,1),UT(2,3),TODX)
D2PDX=DDZ(U(4,J,K-1),U(4,J,K+1),TODX)
D2VDR=DBAR(VT(1,2),VT(2,2),VT(3,2),DR1,DR2)
D2UDR=DBAR(UT(1,2),UT(2,2),UT(3,2),DR1,DR2)
D2HDR=DBAR(HT(1,2),HT(2,2),HT(3,2),DR1,DR2)
D2PDR=DBAR(U(4,J-1,K),U(4,J,K),U(4,J+1,K),DR1,DR2)
D2VDX=CDX2(VT(2,1),VT(2,2),VT(2,3),DX2)
D2UDX=CDX2(UT(2,1),UT(2,2),UT(2,3),DX2)
D2HDX=CDX2(HT(2,1),HT(2,2),HT(2,3),DX2)
D2VDR=DDR2(VT(1,2),VT(2,2),VT(3,2),DR1,DR2)
D2UDR=DDR2(UT(1,2),UT(2,2),UT(3,2),DR1,DR2)
D2HDR=DDR2(HT(1,2),HT(2,2),HT(3,2),DR1,DR2)
D2VDRX=DDR1(3,VT,DR1,DR2,TODX)
D2UDRX=DDR1(3,UT,DR1,DR2,TODX)
VOR=VT(2,2)/RR(J)

```

C---SOURCE TERMS:

```

S(1,J,K)=0.
S(2,J,K)=-C61*DPDR + C62*(D2VDR-VOR)/RR(J)
+ C63*(D2VDX+D2UDRX/3.)/RR(J)+C62*D2VDR
S(3,J,K)=C63*(D2UDR+D2VDX/3.)/RR(J)+D2UDR+D2VDRX/3.)+C62*D2UDX
S(4,J,K)=GAM1*(VT(2,2)*DPDR+UT(2,2)*D2PDX)
+ C64*(D2HDR+D2HDX+D2HDR/RR(J))
+ C65*(2.*(D2UDX**2+D2VDR**2+VOR**2)+(D2UDR+D2VDX)**2
- (2./3.)*(D2VDR+VOR+D2UDX)**2)
1 CONTINUE
RETURN
END

```

Following the "LIBRARY OF FINITE DIFFERENCE FUNCTIONS", first order and second order derivatives are calculated, using central differences with the utility functions specially constructed for this purpose. The variable names used are similar to the actual differential expressions. This form allows for easy detection of errors.

The source terms, $S(M,J,K)$, are finally calculated. The parameters involving gamma, injection Mach No, and Reynolds number, are all pre-calculated in SDATA.

3.3.3 Subroutine SORCE

```

SUBROUTINE SORCE1 (MF, JF, KF, U, S)
  DIMENSION U(MF, JF, KF), S(MF, JF, KF)
  DIMENSION VT(3, 3), UT(3, 3), HT(3, 3)
C----- MBR VERSION OF SOURCE (DISSIPATIVE) TERMS IN MACCORMACK SCHEME
C----- 12/9/83
  COMMON/AREA0/VZERO, PSTAR, TSTAR, VISC, COND, MBAR, RUJ, HSTAR, CP,
+ CFL, RSTAR, XSTAR, XD, IPRNT1, IPRDT(2), ICORR(2), INC(3), ITMAX, VO, PO, RO
  COMMON/AREA1/GAMA, GAM1, GAM2, GAM3, GAM3T, CS1, CS2, CS3, CS4, CS5,
+ RED, EMO, EMO2, P1, P1T, EKM, RHOG, SSND, PRA, DX, TODX, DX2, RR(26), DRR(25),
+ R2(26), R3(26), XX(26), DT, EMS
  COMMON/AREA2/MXX, JRR, KXX, JRM1, KXM1, KXPR(6), KXPMA, JRPR(6),
+ JRPMA, D6X(4, 26, 26), DFR(4, 26, 26), VIC(4, 26, 26), HMO, HMP, RRS, RSM:
C   INC(1)=-1, INC(2)=0, INC(3)=1 INDEX SHIFT OPERATOR.
C   M=THE X-SHIFT DUM., N=THE R-SHIFT DUM.
  DO 1 K=2, KXM1
  DO 1 J=2, JRM1
  DO 3 M=1, 3
    KK=K+INC(M)
  DO 3 N=1, 3
    JJ=J+INC(N)
    RHO=U(1, JJ, KK)
    VT(N, M)=U(2, JJ, KK)/RHO
    UT(N, M)=U(3, JJ, KK)/RHO
  3 HT(N, M)=U(4, JJ, KK)/RHO
  DR1=DRR(J-1)
  DR2=DRR(J)

```

Continued

Subroutine SORCE carries out the calculation of the source terms for the differential system. dissipative terms of first and second order are calculated by use of central differencing. A dummy index shift integer vector is used, INC=(-1,0,+1), to facilitate keeping merely an array of 3x3 of each dependent variable (temporarily, to facilitate the local calculations), these are the local arrays RHO, VT, UT and HT, with (JJ, KK) serving as the 3x3 dummy indices. This facilitates great savings in core and storage requirement.

Continued

```

SUBROUTINE DFDR(MF,JF,KF,U,IF,JTR)
C-----MFR VERSION OF RADIAL FLUX TERM GENERATOR. 12/9/83
DIMENSION U(MF,JF,KF),JTR(IF),F(4,2)
COMMON/AREA2/MXX,JRR,KXX,JRM1,KXM1,KXPR(6),KXPMAX,JRPR(6),
+JRPMAX,DGX(4,26,26),DFR(4,26,26),VIC(4,26,26),HMD,HMF,RRS,RSM1
COMMON/AREA1/GAMA,GAM1,GAM2,GAM3,GAM3T,C61,C62,C63,C64,C65,
+RED,EMD,EMD2,PI,PIT,EKM,RHOG,SSND,PRN,DX,TODX,DX2,RR(26),DRR(25),
+R2(26),R3(26),XX(26),DT,EPS
DO 1 K=2,KXM1
DO 1 J=2,JRM1
DRO=DRR(J+JTR(1))
DR1=R3(J)*DRO/DRR(J-JTR(2))
DO 2 N=1,IF
JJ=J+JTR(N)
F(1,N)=RR(J)*U(2,JJ,K)
V2=F(1,N)/U(1,JJ,K)
IF(N.GT.1)GO TO 6
VM2=V2
GO TO 7
6 J1=JJ-JTR(1)
VM2=(RR(J1)*U(2,J1,K)/U(1,J1,K)+RR(J)*U(2,J,K)/U(1,J,K))/2.
7 F(2,N)=VM2*U(2,JJ,K)
F(3,N)=V2*U(3,JJ,K)
2 F(4,N)=V2+GAMA*U(4,JJ,K)
DO 3 M=1,MF
3 DFR(M,J,K)=(F(M,2)-F(M,1))/DR1
1 CONTINUE
RETURN
END

```

Subroutine DFDR carries out the radial differencing to calculate the radial flux array, DFR. Operation is very similar to DGDG, with JTR=(-1,0) for the predictor step, and JTR=(0,+1) in the corrector step, acting as the appropriate radial index shift. The parameter VM2 is the mean radial advective velocity, analogous to the UM2-term discussed earlier.

The differencing is not symmetrical overall, as the parameter DR1 is different for backward and for forward differences, to account for the variable radial mesh size, and maintain second-order accuracy overall; "overall" herein means when the backward and forward terms are combined, in the calculation of the U-array following the predictor step, cf Do-loop #7 in subroutine TIMINT. When a uniform radial meshsize is imposed, however, the calculation automatically becomes similar to the overall-central differencing in DGDG.

3.3.2 Subroutines DGD_X and DFDR

```

SUBROUTINE DGDX(MF, JF, KF, U, IF, KTR)
C--- MBR VERSION OF AXIAL FLUX TERM GENERATOR. 12/9/83.
  DIMENSION U(MF, JF, KF), KTR(IF), G(4, 2)
  COMMON/AREA1/GAMA, GAM1, GAM2, GAM3, GAM3T, CG1, CG2, CG3, CG4, CG5,
+R2(26), R3(26), XX(26), DT, EPS
  COMMON/AREA2/MXX, JRR, KXX, JRM1, KXM1, KXPR(6), KXPMAX, JRPR(6),
+JRPMAX, DGX(4, 26, 26), DFR(4, 26, 26), VIC(4, 26, 26), HMD, HWP, RRS, RSM1
  DO 1 J=2, JRM1
  DO 1 K=2, KXM1
  DO 2 N=1, IF
    KK=K+KTR(N)
    U3=U(3, J, KK)/U(1, J, KK)
    G(1, N)=U(3, J, KK)
    G(2, N)=U3*U(2, J, KK)
    IF(N.GT.1)GO TO 6
    UM3=U3
  GO TO 7
6 K1=KK-KTR(1)
  UM3=(U(3, J, K1)/U(1, J, K1)+U(3, J, K)/U(1, J, K))/2.
7 G(3, N)=UM3*U(3, J, KK)+CG1*U(4, J, KK)
2 G(4, N)=U3*GAMA+U(4, J, KK)
  DO 3 M=1, MF
3 DGX(M, J, K)=(G(M, 2)-G(M, 1))/DX
1 CONTINUE
  RETURN
END

```

Subroutine DGD_X calculates the four axial flux terms in discretized form. KTR=(-1,0) for the predictor phase, and KTR=(0,+1) for the corrector phase. This integer vector is used as an index transform, to calculate the dummy axial mesh index KK. This way, both predictor (backward differencing) and corrector (forward differencing) can be facilitated in the same subroutine.

G(4,2) is the temporary advective term array, reloaded at each new meshpoint. DGX is the axial flux array arising from this calculation.

Note that the use of the mean axial velocity UM3 for the axial advective term G(3,n) has been suggested by MacCormack(1974), to alleviate problems inherent in the non-conservative nature of the $\rho U \cdot U$ terms.

The corrector step is similar in structure, and is carried out after the call to subroutine BNDRY establishes the variable boundary data corresponding to the predicted interior UB-values. Thus calls to subroutines DFDR, DGDX and SORCE establish the corrected flux terms and source terms respectively. The value of the integer vector ICORR=(0,1), passed in the argument lists of DFDR and DGDX, insures that the same subroutines will carry out forward differencing in the corrector phase. Do-loop #7 is used to calculate the entire inner variable array, followed by a call to BNDRY to re-calculate the variable boundary data. Note that both predicted and corrected values of the source term vector (S and SB respectively) are used in the corrector step, which requires storage of the S array.

C-----CALCULATION OF TIMESTEP,DT, USING THE COURANT-F-L CONDITION:

```
ENX=XD/RO
UMAX=2.*ENX
CX=UMAX+1./EMO
CR=1.+1./EMO
DTXX=CFL*DX/CX
DREF=DRR(JRM1)
DTRR=CFL*DREF/CR
DT=AMIN1(DTXX,DTRR)
```

C-----MOR VERSION, MACCORMACK INTEGRATION OF COLD FLO. 12/5/83

C.....FOR SDATA1. NONUNIFORM DR-MESH. NOTE: DRR(J)=INPUT VECTOR.

```
SUM=0.
DO 1 J=1,JRM1
1 SUM=SUM+DRR(J)
RR(1)=0.
DO 2 J=2,JRM1
J=J-1
DRR(I)=DRR(I)/SUM
RR(J)=RR(I)+DRR(I)
R3(J)=(DRR(I)+DRR(J))*RR(J)/2.
2 R2(I)=RR(J)**2-RR(I)**2
RR(JRR)=RR(JRM1)+DRR(JRM1)
R2(JRR)=RR(JRR)**2-RR(JRM1)**2
RRS=(RR(JRR)-RR(JRR-2))/DRR(JRM1)
RSM1=RRS-1.
```

C-----UNIFORM X-MESH:

```
XX(1)=0.
DO 3 K=2,KXX
3 XX(K)=(K-1)*DX
```

C-----INITIAL DATA--PRIMITIVE VARIABLES FIRST:DENSITY, RAD. VEL,

C AXIAL VEL., PRESSURE. FROM CULICK'S (1966) ANALYSIS.

```
PI=4.*ATAN(1.)
PIT=PI/2.
VR(1)=0.
VX(1)=1.
DO 4 J=2,JRR
ARG=PIT*RR(J)**2
VR(J)=-SIN(ARG)/RR(J)
4 VX(J)=COS(ARG)
VX(JRR)=0.
DO 5 K=1,KXX
ARG=PI*XX(K)
ARG2=ARG**2
ARG3=1./(1.+(1.+ARG2)*GAM3T)
ARG3=1.-GAM3T*(1.+ARG2)
DO 5 J=1,JRR
VIC(1,J,K)=1.
VIC(2,J,K)=VR(J)
VIC(3,J,K)=VX(J)*ARG
5 VIC(4,J,K)=ARG3
```

Continued

```

C-----TEMPORARY INPUT: THE WALL ENTHALPIES, AT X=0, HMD. AT R=1, HMP
HMD=1.
HMP=HMD
C-----AT X=0, THE RADIAL VELOCITY=0:
DO 51 J=2, JRM1
51 VIC(2,J,1)=0.
C-----THE INITIAL DATA--ACTUAL DEPENDENT VARIABLES:
DO 6 J=1, JRR
DO 6 K=1, KXX
RHO=VIC(1,J,K)
UB(1,J,K)=RHO
UB(2,J,K)=RHO*VIC(2,J,K)
UB(3,J,K)=RHO*VIC(3,J,K)
6 UB(4,J,K)=VIC(4,J,K)
DO 7 J=1, JRR
DO 7 K=1, KXX
DO 7 M=1, MXX
7 U(M,J,K)=UB(M,J,K)
C.....NOTE: THE FOREGOING INCLUDES THE BOUNDARY DATA. ALL OF THE
C ABOVE SOLUTIONS SATISFY THE INITIAL SET OF BCS.
WRITE(6,1000) RSTAR, RD, XSTAR, XD, VZERO, VO, PSTAR, PO
TSCALE=RSTAR/VZERO
WRITE(6,1005) RHO0, SSND, TSTAR, RUJ, WBAR, HSTAR, CP,
* REO, IPRT1, PRN, ITMAX, EMO, TSCALE, GAMA, RSTAR, CFL, DREF, DX, DT
1000 FORMAT(1H1,8X,'MOTOR RADIUS(M)=' ,F5.2,10X,'RD(DIMENSIONLESS)='
* ,F5.2/9X,'MOTOR LENGTH(M)=' ,F5.2,12X,'XD(DIMENSIONLESS)=' ,F5.2/
* ,9X,'INJECTION VELOCITY(M/SEC)=' ,F5.2,' VO(DIMENSIONLESS)=' ,F5.2
* ,/9X,'GAS PRESSURE(N/M**2)=' ,1PE9.2,3X,'PO(DIMENSIONLESS)=' ,
* @PF5.2)
1005 FORMAT(9X,'GAS DENSITY(KG/M**3)=' ,F6.3/
* 9X,'SPEED OF SOUND(M/SEC)=' ,1PE9.2/
* 9X,'TSTAR=' ,@PF7.3,/,9X,'RUJ=' ,F6.3,/,9X,
* 'WBAR=' ,F6.3,/,9X,'HSTAR=' ,1PE9.2,/,9X,
* 'CP=' ,1PE9.2,/,
* 9X,'REO=' ,1PE9.2,8X,'PRINTOUT EACH=' ,15,' Timesteps'
* ,/9X,'PRN=' ,@PF6.3,11X,'TOTAL RUN DURATION=' ,15,' Timesteps'
* ,/9X,'EMO=' ,1PE9.2,8X,'TSCALE(SEC)=' ,1PE9.2
* ,/9X,'GAMA=' ,@PF6.3,10X,'XSCALE(M)=' ,1PE9.2
* ,/9X,'CFL=' ,@PF6.3/9X,'DREF=' ,F7.4/9X,'DX=' ,F7.4/9X,'DT=' ,1PE9.
* 2,////)
DIFFPR=.TRUE.
TIME=0.
L=0
CALL PRINT2(TIME,L)
DIFFPR=.FALSE.
RETURN
END

```

following the printout of the constant parameters at the last section of Subroutine SDATA, subroutine PRINT is called to dump the initial profiles, in the form of X-maps and R-maps.

3.6 PRINTOUT

3.6.1 Input Data and Parameters Calculated in 'SDADA'

C-----MOSCO5 OUTPUT FILE/3.25.1984-----

MOTOR RADIUS(M)= 0.05	RO(DIMENSIONLESS)= 1.00
MOTOR LENGTH(M)= 0.55	XO(DIMENSIONLESS)=11.00
INJECTION VELOCITY(M/SEC)= 1.00	VO(DIMENSIONLESS)= 1.00
GAS PRESSURE(N/M**2)= 2.00E+05	PO(DIMENSIONLESS)= 1.00
GAS DENSITY(KG/M**3)= 2.423	
SPEED OF SOUND(M/SEC)= 3.40E+02	
TSTAR=278.000	
RIJ= 8.314	
WBAR= 0.020	
WSTAR= 2.89E+05	
CP= 1.04E+03	
REO= 1.21E+04	PRINTOUT EACH= 200 TIMESTEPS
PRN= 0.626	TOTAL RUN DURATION= 1201TIMESTEPS
EYO= 2.94E-03	TSCALE(SEC)= 5.00E-02
GAMA= 1.400	XSCALE(M)= 5.00E-02
CFL= 0.500	
DREF= 0.0050	
DX= 1.0000	
DT= 7.33E-06	

3.6.2 Initial Data (Culick Profiles) for Datum Case

TIME = 0.0 TIMESTEP NO. = 0

X-MAP, AT DISTINCT RADIAL POSITIONS

RHO = DIM. LESS DENSITY

YZ	XZ= 0.0	XZ= 0.2000	XZ= 0.5500	XZ= 0.8000	XZ= 0.9600	XZ= 0.9950
0.0	1.0000E+00	1.0000E+00	1.0000E+00	1.0000E+00	1.0000E+00	1.0000E+00
1.000	1.0000E+00	1.0000E+00	1.0000E+00	1.0000E+00	1.0000E+00	1.0000E+00
2.000	1.0000E+00	1.0000E+00	1.0000E+00	1.0000E+00	1.0000E+00	1.0000E+00
3.000	1.0000E+00	1.0000E+00	1.0000E+00	1.0000E+00	1.0000E+00	1.0000E+00
4.000	1.0000E+00	1.0000E+00	1.0000E+00	1.0000E+00	1.0000E+00	1.0000E+00
5.000	1.0000E+00	1.0000E+00	1.0000E+00	1.0000E+00	1.0000E+00	1.0000E+00
6.000	1.0000E+00	1.0000E+00	1.0000E+00	1.0000E+00	1.0000E+00	1.0000E+00
7.000	1.0000E+00	1.0000E+00	1.0000E+00	1.0000E+00	1.0000E+00	1.0000E+00
8.000	1.0000E+00	1.0000E+00	1.0000E+00	1.0000E+00	1.0000E+00	1.0000E+00
9.000	1.0000E+00	1.0000E+00	1.0000E+00	1.0000E+00	1.0000E+00	1.0000E+00
10.000	1.0000E+00	1.0000E+00	1.0000E+00	1.0000E+00	1.0000E+00	1.0000E+00
11.000	1.0000E+00	1.0000E+00	1.0000E+00	1.0000E+00	1.0000E+00	1.0000E+00

VR = DIM. LESS RADIAL VELOCITY

YZ	XZ= 0.0	XZ= 0.2000	XZ= 0.5500	XZ= 0.8000	XZ= 0.9600	XZ= 0.9950
0.0	0.0	0.0	0.0	0.0	0.0	0.0
1.000	0.0	-3.1395E-01	-8.3179E-01	-1.0554E+00	-1.0338E+00	-1.0049E+00
2.000	0.0	-3.1395E-01	-8.3179E-01	-1.0554E+00	-1.0338E+00	-1.0049E+00
3.000	0.0	-3.1395E-01	-8.3179E-01	-1.0554E+00	-1.0338E+00	-1.0049E+00
4.000	0.0	-3.1395E-01	-8.3179E-01	-1.0554E+00	-1.0338E+00	-1.0049E+00
5.000	0.0	-3.1395E-01	-8.3179E-01	-1.0554E+00	-1.0338E+00	-1.0049E+00
6.000	0.0	-3.1395E-01	-8.3179E-01	-1.0554E+00	-1.0338E+00	-1.0049E+00
7.000	0.0	-3.1395E-01	-8.3179E-01	-1.0554E+00	-1.0338E+00	-1.0049E+00
8.000	0.0	-3.1395E-01	-8.3179E-01	-1.0554E+00	-1.0338E+00	-1.0049E+00
9.000	0.0	-3.1395E-01	-8.3179E-01	-1.0554E+00	-1.0338E+00	-1.0049E+00
10.000	0.0	-3.1395E-01	-8.3179E-01	-1.0554E+00	-1.0338E+00	-1.0049E+00
11.000	0.0	-3.1395E-01	-8.3179E-01	-1.0554E+00	-1.0338E+00	-1.0049E+00

VX = DIM. LESS AXIAL VELOCITY

YZ	XZ= 0.0	XZ= 0.2000	XZ= 0.5500	XZ= 0.8000	XZ= 0.9600	XZ= 0.9950
0.0	0.0	0.0	0.0	0.0	0.0	0.0
1.000	3.1416E+00	3.1354E+00	2.7936E+00	1.6833E+00	3.8591E-01	4.9227E-02
2.000	6.2832E+00	6.2708E+00	5.5871E+00	3.3667E+00	7.7183E-01	9.8454E-02
3.000	9.4248E+00	9.4062E+00	8.3807E+00	5.0501E+00	1.1577E+00	1.4768E-01
4.000	1.2566E+01	1.2542E+01	1.1174E+01	6.7334E+00	1.5437E+00	1.9691E-01
5.000	1.5708E+01	1.5677E+01	1.3968E+01	8.4168E+00	1.9296E+00	2.4614E-01
6.000	1.8850E+01	1.8812E+01	1.6761E+01	1.0100E+01	2.3155E+00	2.9536E-01
7.000	2.1991E+01	2.1948E+01	1.9555E+01	1.1783E+01	2.7014E+00	3.4459E-01
8.000	2.5133E+01	2.5083E+01	2.2348E+01	1.3467E+01	3.0873E+00	3.9382E-01
9.000	2.8274E+01	2.8219E+01	2.5142E+01	1.5150E+01	3.4732E+00	4.4304E-01
10.000	3.1416E+01	3.1354E+01	2.7936E+01	1.6833E+01	3.8591E+00	4.9227E-01
11.000	3.4558E+01	3.4489E+01	3.0729E+01	1.8517E+01	4.2450E+00	5.4150E-01

Continued

P = DIM. LESS STATIC PRESSURE

YZ	XZ= 0.0	XZ= 0.2000	XZ= 0.5500	XZ= 0.8000	XZ= 0.9600	XZ= 0.9950
0.0	9.9999E-01	9.9999E-01	9.9999E-01	9.9999E-01	9.9999E-01	9.9999E-01
1.000	9.9993E-01	9.9993E-01	9.9993E-01	9.9993E-01	9.9993E-01	9.9993E-01
2.000	9.9975E-01	9.9975E-01	9.9975E-01	9.9975E-01	9.9975E-01	9.9975E-01
3.000	9.9946E-01	9.9946E-01	9.9946E-01	9.9946E-01	9.9946E-01	9.9946E-01
4.000	9.9904E-01	9.9904E-01	9.9904E-01	9.9904E-01	9.9904E-01	9.9904E-01
5.000	9.9850E-01	9.9850E-01	9.9850E-01	9.9850E-01	9.9850E-01	9.9850E-01
6.000	9.9784E-01	9.9784E-01	9.9784E-01	9.9784E-01	9.9784E-01	9.9784E-01
7.000	9.9706E-01	9.9706E-01	9.9706E-01	9.9706E-01	9.9706E-01	9.9706E-01
8.000	9.9617E-01	9.9617E-01	9.9617E-01	9.9617E-01	9.9617E-01	9.9617E-01
9.000	9.9515E-01	9.9515E-01	9.9515E-01	9.9515E-01	9.9515E-01	9.9515E-01
10.000	9.9402E-01	9.9402E-01	9.9402E-01	9.9402E-01	9.9402E-01	9.9402E-01
11.000	9.9276E-01	9.9276E-01	9.9276E-01	9.9276E-01	9.9276E-01	9.9276E-01

R-RAP, AT DISTINCT AXIAL POSITIONS

RHO = DIM. LESS DENSITY

YZ	XZ= 0.0	XZ= 2.0000	XZ= 4.0000	XZ= 6.0000	XZ= 8.0000	XZ=10.0000
0.0	1.0000E+00	1.0000E+00	1.0000E+00	1.0000E+00	1.0000E+00	1.0000E+00
0.050	1.0000E+00	1.0000E+00	1.0000E+00	1.0000E+00	1.0000E+00	1.0000E+00
0.200	1.0000E+00	1.0000E+00	1.0000E+00	1.0000E+00	1.0000E+00	1.0000E+00
0.400	1.0000E+00	1.0000E+00	1.0000E+00	1.0000E+00	1.0000E+00	1.0000E+00
0.550	1.0000E+00	1.0000E+00	1.0000E+00	1.0000E+00	1.0000E+00	1.0000E+00
0.700	1.0000E+00	1.0000E+00	1.0000E+00	1.0000E+00	1.0000E+00	1.0000E+00
0.800	1.0000E+00	1.0000E+00	1.0000E+00	1.0000E+00	1.0000E+00	1.0000E+00
0.900	1.0000E+00	1.0000E+00	1.0000E+00	1.0000E+00	1.0000E+00	1.0000E+00
0.960	1.0000E+00	1.0000E+00	1.0000E+00	1.0000E+00	1.0000E+00	1.0000E+00
0.985	1.0000E+00	1.0000E+00	1.0000E+00	1.0000E+00	1.0000E+00	1.0000E+00
0.995	1.0000E+00	1.0000E+00	1.0000E+00	1.0000E+00	1.0000E+00	1.0000E+00
1.000	1.0000E+00	1.0000E+00	1.0000E+00	1.0000E+00	1.0000E+00	1.0000E+00

VR = DIM. LESS RADIAL VELOCITY

YZ	XZ= 0.0	XZ= 2.0000	XZ= 4.0000	XZ= 6.0000	XZ= 8.0000	XZ=10.0000
0.0	0.0	0.0	0.0	0.0	0.0	0.0
0.050	0.0	-7.8539E-02	-7.8539E-02	-7.8539E-02	-7.8539E-02	-7.8539E-02
0.200	0.0	-3.1395E-01	-3.1395E-01	-3.1395E-01	-3.1395E-01	-3.1395E-01
0.400	0.0	-6.2172E-01	-6.2172E-01	-6.2172E-01	-6.2172E-01	-6.2172E-01
0.550	0.0	-8.3179E-01	-8.3179E-01	-8.3179E-01	-8.3179E-01	-8.3179E-01
0.700	0.0	-9.9416E-01	-9.9416E-01	-9.9416E-01	-9.9416E-01	-9.9416E-01
0.800	0.0	-1.0554E+00	-1.0554E+00	-1.0554E+00	-1.0554E+00	-1.0554E+00
0.900	0.0	-1.0620E+00	-1.0620E+00	-1.0620E+00	-1.0620E+00	-1.0620E+00
0.960	0.0	-1.0338E+00	-1.0338E+00	-1.0338E+00	-1.0338E+00	-1.0338E+00
0.985	0.0	-1.0141E+00	-1.0141E+00	-1.0141E+00	-1.0141E+00	-1.0141E+00
0.995	0.0	-1.0049E+00	-1.0049E+00	-1.0049E+00	-1.0049E+00	-1.0049E+00
1.000	-1.0000E+00	-1.0000E+00	-1.0000E+00	-1.0000E+00	-1.0000E+00	-1.0000E+00

Continued

VX = DIM. LESS AXIAL VELOCITY

YZ	XZ= 0.0	XZ= 2.0000	XZ= 4.0000	XZ= 6.0000	XZ= 8.0000	XZ=10.0000
0.0	0.0	6.2832E+00	1.2566E+01	1.8850E+01	2.5133E+01	3.1416E+01
0.050	0.0	6.2831E+00	1.2566E+01	1.8849E+01	2.5133E+01	3.1416E+01
0.200	0.0	6.2708E+00	1.2542E+01	1.8812E+01	2.5083E+01	3.1354E+01
0.400	0.0	6.0858E+00	1.2172E+01	1.8257E+01	2.4343E+01	3.0429E+01
0.550	0.0	5.5871E+00	1.1174E+01	1.6761E+01	2.2348E+01	2.7936E+01
0.700	0.0	4.5121E+00	9.0242E+00	1.3536E+01	1.8048E+01	2.2561E+01
0.800	0.0	3.3667E+00	6.7334E+00	1.0100E+01	1.3467E+01	1.6833E+01
0.900	0.0	1.8475E+00	3.6950E+00	5.5426E+00	7.3901E+00	9.2376E+00
0.960	0.0	7.7183E-01	1.5437E+00	2.3155E+00	3.0873E+00	3.8591E+00
0.985	0.0	2.9377E-01	5.8753E-01	8.8138E-01	1.1751E+00	1.4688E+00
0.995	0.0	9.8454E-02	1.9691E-01	2.9536E-01	3.9382E-01	4.9227E-01
1.000	0.0	0.0	0.0	0.0	0.0	0.0

P = DIM. LESS STATIC PRESSURE

YZ	XZ= 0.0	XZ= 2.0000	XZ= 4.0000	XZ= 6.0000	XZ= 8.0000	XZ=10.0000
0.0	9.9999E-01	9.9975E-01	9.9904E-01	9.9784E-01	9.9617E-01	9.9402E-01
0.050	9.9999E-01	9.9975E-01	9.9904E-01	9.9784E-01	9.9617E-01	9.9402E-01
0.200	9.9999E-01	9.9975E-01	9.9904E-01	9.9784E-01	9.9617E-01	9.9402E-01
0.400	9.9999E-01	9.9975E-01	9.9904E-01	9.9784E-01	9.9617E-01	9.9402E-01
0.550	9.9999E-01	9.9975E-01	9.9904E-01	9.9784E-01	9.9617E-01	9.9402E-01
0.700	9.9999E-01	9.9975E-01	9.9904E-01	9.9784E-01	9.9617E-01	9.9402E-01
0.800	9.9999E-01	9.9975E-01	9.9904E-01	9.9784E-01	9.9617E-01	9.9402E-01
0.900	9.9999E-01	9.9975E-01	9.9904E-01	9.9784E-01	9.9617E-01	9.9402E-01
0.960	9.9999E-01	9.9975E-01	9.9904E-01	9.9784E-01	9.9617E-01	9.9402E-01
0.985	9.9999E-01	9.9975E-01	9.9904E-01	9.9784E-01	9.9617E-01	9.9402E-01
0.995	9.9999E-01	9.9975E-01	9.9904E-01	9.9784E-01	9.9617E-01	9.9402E-01
1.000	9.9999E-01	9.9975E-01	9.9904E-01	9.9784E-01	9.9617E-01	9.9402E-01

INTERMEDIATE STEPS PRINTOUT FOLLOWS . . .

(FOR n < ITMAX)

3.6.3 Final Step Printout, Datum Case (Step No. 1201)

TIME = 8.7981E-03 TIMESTL -1201

X-MAP, AT DISTINCT RADIAL POSITIONS

RHO = DIM. LESS DENSITY

YZ	XZ= 0.0	XZ= 0.2000	XZ= 0.5500	XZ= 0.8000	XZ= 0.9600	XZ= 0.9950
0.0	9.8137E-01	9.8133E-01	9.8133E-01	9.8135E-01	9.8181E-01	9.8198E-01
1.000	9.8650E-01	9.8651E-01	9.8655E-01	9.8659E-01	9.8684E-01	9.8463E-01
2.000	9.8653E-01	9.8653E-01	9.8667E-01	9.8666E-01	9.8689E-01	9.8461E-01
3.000	9.8653E-01	9.8652E-01	9.8657E-01	9.8662E-01	9.8687E-01	9.8437E-01
4.000	9.8658E-01	9.8652E-01	9.8665E-01	9.8666E-01	9.8676E-01	9.8389E-01
5.000	9.8658E-01	9.8653E-01	9.8662E-01	9.8663E-01	9.8690E-01	9.8373E-01
6.000	9.8656E-01	9.8653E-01	9.8660E-01	9.8663E-01	9.8699E-01	9.8336E-01
7.000	9.8658E-01	9.8653E-01	9.8662E-01	9.8670E-01	9.8673E-01	9.8235E-01
8.000	9.8658E-01	9.8654E-01	9.8663E-01	9.8670E-01	9.8701E-01	9.8218E-01
9.000	9.8660E-01	9.8659E-01	9.8668E-01	9.8679E-01	9.8717E-01	9.8165E-01
10.000	9.8665E-01	9.8669E-01	9.8678E-01	9.8686E-01	9.8717E-01	9.8077E-01
11.000	9.8671E-01	9.8680E-01	9.8689E-01	9.8693E-01	9.8717E-01	9.7989E-01

VR = DIM. LESS RADIAL VELOCITY

YZ	XZ= 0.0	XZ= 0.2000	XZ= 0.5500	XZ= 0.8000	XZ= 0.9600	XZ= 0.9950
0.0	0.0	0.0	0.0	0.0	0.0	0.0
1.000	0.0	-2.4673E-01	-9.7828E-01	-1.1914E+00	-9.0368E-01	-1.0036E+00
2.000	0.0	-2.4820E-01	-9.7119E-01	-1.1660E+00	-1.0278E+00	-1.0188E+00
3.000	0.0	-2.4336E-01	-9.7252E-01	-1.1697E+00	-9.6994E-01	-1.0136E+00
4.000	0.0	-2.4487E-01	-9.6701E-01	-1.1661E+00	-1.0551E+00	-1.0237E+00
5.000	0.0	-2.4837E-01	-9.7014E-01	-1.1758E+00	-1.0231E+00	-1.0199E+00
6.000	0.0	-2.5339E-01	-9.7000E-01	-1.1627E+00	-1.0118E+00	-1.0192E+00
7.000	0.0	-2.4248E-01	-9.7718E-01	-1.1691E+00	-1.0146E+00	-1.0206E+00
8.000	0.0	-2.5518E-01	-9.8039E-01	-1.1653E+00	-1.0057E+00	-1.0189E+00
9.000	0.0	-2.4381E-01	-9.7789E-01	-1.1697E+00	-9.4666E-01	-1.0129E+00
10.000	0.0	-2.5297E-01	-9.6403E-01	-1.1675E+00	-1.0771E+00	-1.0305E+00
11.000	0.0	-2.6213E-01	-9.5017E-01	-1.1653E+00	-1.2076E+00	-1.0481E+00

VX = DIM. LESS AXIAL VELOCITY

YZ	XZ= 0.0	XZ= 0.2000	XZ= 0.5500	XZ= 0.8000	XZ= 0.9600	XZ= 0.9950
0.0	0.0	0.0	0.0	0.0	0.0	0.0
1.000	3.1669E+00	3.1613E+00	2.8102E+00	1.6932E+00	3.8718E-01	3.9751E-02
2.000	6.2929E+00	6.2794E+00	5.5849E+00	3.3570E+00	7.5780E-01	8.8714E-02
3.000	9.4458E+00	9.4238E+00	8.3856E+00	5.0507E+00	1.1542E+00	1.4690E-01
4.000	1.2574E+01	1.2547E+01	1.1161E+01	6.7178E+00	1.5228E+00	1.8374E-01
5.000	1.5716E+01	1.5682E+01	1.3951E+01	8.3328E+00	1.9080E+00	2.3510E-01
6.000	1.8845E+01	1.8805E+01	1.6732E+01	1.0075E+01	2.2930E+00	2.8389E-01
7.000	2.1987E+01	2.1938E+01	1.9519E+01	1.1752E+01	2.6719E+00	3.2844E-01
8.000	2.5115E+01	2.5057E+01	2.2291E+01	1.3417E+01	3.0407E+00	3.6721E-01
9.000	2.8243E+01	2.8180E+01	2.5073E+01	1.5088E+01	3.4100E+00	4.0293E-01
10.000	3.1348E+01	3.1274E+01	2.7820E+01	1.6717E+01	3.7468E+00	4.2128E-01
11.000	3.4452E+01	3.4367E+01	3.0566E+01	1.8345E+01	4.0635E+00	4.3959E-01

Continued

P = DIM. LESS STATIC PRESSURE

YZ	XZ= 0.0	XZ= 0.2000	XZ= 0.5500	XZ= 0.8000	XZ= 0.9600	XZ= 0.9950
0.0	9.8137E-01	9.8133E-01	9.8133E-01	9.8135E-01	9.8181E-01	9.8198E-01
1.000	9.8125E-01	9.8123E-01	9.8128E-01	9.8132E-01	9.8172E-01	9.8193E-01
2.000	9.8114E-01	9.8113E-01	9.8124E-01	9.8129E-01	9.8164E-01	9.8189E-01
3.000	9.8085E-01	9.8083E-01	9.8088E-01	9.8092E-01	9.8133E-01	9.8159E-01
4.000	9.8047E-01	9.8044E-01	9.8052E-01	9.8059E-01	9.8078E-01	9.8094E-01
5.000	9.7998E-01	9.7995E-01	9.8002E-01	9.8005E-01	9.8047E-01	9.8076E-01
6.000	9.7935E-01	9.7934E-01	9.7938E-01	9.7944E-01	9.7996E-01	9.8029E-01
7.000	9.7866E-01	9.7861E-01	9.7870E-01	9.7875E-01	9.7886E-01	9.7896E-01
8.000	9.7782E-01	9.7780E-01	9.7787E-01	9.7791E-01	9.7841E-01	9.7877E-01
9.000	9.7693E-01	9.7693E-01	9.7702E-01	9.7704E-01	9.7767E-01	9.7810E-01
10.000	9.7596E-01	9.7596E-01	9.7605E-01	9.7607E-01	9.7659E-01	9.7693E-01
11.000	9.7499E-01	9.7500E-01	9.7507E-01	9.7512E-01	9.7558E-01	9.7575E-01

DIFFERENCES BETWEEN CURRENT TIMESTEP NO. 1201
AND THE INITIAL DATA U(M,J,K)-UINITIAL(M,J,K) :

X-MAP, AT DISTINCT RADIAL POSITIONS

RHO = DIM. LESS DENSITY

YZ	XZ= 0.0	XZ= 0.2000	XZ= 0.5500	XZ= 0.8000	XZ= 0.9600	XZ= 0.9950
0.0	-1.8634E-02	-1.8672E-02	-1.8675E-02	-1.8647E-02	-1.8193E-02	-1.8021E-02
1.000	-1.3495E-02	-1.3494E-02	-1.3447E-02	-1.3410E-02	-1.3165E-02	-1.5371E-02
2.000	-1.3474E-02	-1.3468E-02	-1.3333E-02	-1.3337E-02	-1.3106E-02	-1.5389E-02
3.000	-1.3466E-02	-1.3483E-02	-1.3430E-02	-1.3379E-02	-1.3129E-02	-1.5633E-02
4.000	-1.3424E-02	-1.3482E-02	-1.3354E-02	-1.3339E-02	-1.3239E-02	-1.6114E-02
5.000	-1.3416E-02	-1.3472E-02	-1.3377E-02	-1.3368E-02	-1.3103E-02	-1.6266E-02
6.000	-1.3436E-02	-1.3469E-02	-1.3404E-02	-1.3372E-02	-1.3008E-02	-1.6644E-02
7.000	-1.3423E-02	-1.3471E-02	-1.3381E-02	-1.3304E-02	-1.3273E-02	-1.7637E-02
8.000	-1.3425E-02	-1.3462E-02	-1.3368E-02	-1.3303E-02	-1.2994E-02	-1.7821E-02
9.000	-1.3402E-02	-1.3412E-02	-1.3321E-02	-1.3212E-02	-1.2827E-02	-1.8349E-02
10.000	-1.3346E-02	-1.3306E-02	-1.3215E-02	-1.3143E-02	-1.2828E-02	-1.9231E-02
11.000	-1.3291E-02	-1.3201E-02	-1.3110E-02	-1.3073E-02	-1.2830E-02	-2.0114E-02

VR = DIM. LESS RADIAL VELOCITY

YZ	XZ= 0.0	XZ= 0.2000	XZ= 0.5500	XZ= 0.8000	XZ= 0.9600	XZ= 0.9950
0.0	0.0	0.0	0.0	0.0	0.0	0.0
1.000	0.0	6.7218E-02	-1.4649E-01	-1.3595E-01	1.2990E-01	1.2789E-03
2.000	0.0	6.5748E-02	-1.3940E-01	-1.1056E-01	6.8110E-03	-1.3935E-02
3.000	0.0	7.0591E-02	-1.4072E-01	-1.1428E-01	6.3634E-02	-8.6832E-03
4.000	0.0	6.9083E-02	-1.3522E-01	-1.1065E-01	-2.1356E-02	-1.8764E-02
5.000	0.0	6.5582E-02	-1.3835E-01	-1.2044E-01	1.0669E-02	-1.5005E-02
6.000	0.0	6.0562E-02	-1.3901E-01	-1.0731E-01	2.1954E-02	-1.4344E-02
7.000	0.0	7.1472E-02	-1.4539E-01	-1.1369E-01	1.9144E-02	-1.5697E-02
8.000	0.0	5.8774E-02	-1.4860E-01	-1.0994E-01	2.8033E-02	-1.3985E-02
9.000	0.0	7.0144E-02	-1.4610E-01	-1.1433E-01	8.7116E-02	-7.9870E-03
10.000	0.0	6.0981E-02	-1.3224E-01	-1.1214E-01	-4.3362E-02	-2.5578E-02
11.000	0.0	5.1820E-02	-1.1838E-01	-1.0994E-01	-1.7384E-01	-4.3202E-02

Continued

VX = DIM. LESS AXIAL VELOCITY

YZ	XZ= 0.0	XZ= 0.2000	XZ= 0.5500	XZ= 0.8000	XZ= 0.9600	XZ= 0.9950
0.0	0.0	0.0	0.0	0.0	0.0	0.0
1.000	8.0469E-03	8.2381E-03	5.2969E-03	3.1428E-03	4.8304E-04	-3.0165E-03
2.000	1.5430E-03	1.3724E-03	-3.5836E-04	-1.5509E-03	-2.2320E-03	-1.5502E-03
3.000	2.2320E-03	1.8676E-03	5.2112E-04	7.2349E-05	-3.7106E-04	-8.2405E-05
4.000	6.4227E-04	3.9873E-04	-1.0218E-03	-1.2396E-03	-1.6592E-03	-1.0483E-03
5.000	5.2626E-04	2.9045E-04	-1.0530E-03	-1.5270E-03	-1.3711E-03	-7.0257E-04
6.000	-2.3314E-04	-3.7075E-04	-1.5332E-03	-1.3195E-03	-1.1910E-03	-6.0887E-04
7.000	-2.0955E-04	-4.3089E-04	-1.6521E-03	-1.4108E-03	-1.3402E-03	-7.3455E-04
8.000	-7.1641E-04	-1.0376E-03	-2.2949E-03	-1.9693E-03	-1.8538E-03	-1.0586E-03
9.000	-1.0928E-03	-1.3567E-03	-2.4447E-03	-2.2133E-03	-2.2342E-03	-1.4165E-03
10.000	-2.1643E-03	-2.5446E-03	-3.6875E-03	-3.7215E-03	-3.5760E-03	-2.2598E-03
11.000	-3.0511E-03	-3.5359E-03	-4.7210E-03	-4.9626E-03	-4.6739E-03	-2.9489E-03

P = DIM. LESS STATIC PRESSURE

YZ	XZ= 0.0	XZ= 0.2000	XZ= 0.5500	XZ= 0.8000	XZ= 0.9600	XZ= 0.9950
0.0	0.0	4.2251E-03	4.5995E-03	1.4373E-03	-4.9407E-02	-6.8672E-02
1.000	1.2502E-02	1.5103E-02	9.1191E-03	4.9404E-03	-3.9095E-02	-6.3684E-02
2.000	2.5021E-02	2.6038E-02	1.3679E-02	8.4973E-03	-3.0360E-02	-5.0656E-02
3.000	5.7909E-02	6.0486E-02	5.4590E-02	4.9919E-02	3.8641E-03	-2.5471E-02
4.000	1.0046E-01	1.0394E-01	9.4486E-02	8.6820E-02	6.6107E-02	4.8334E-02
5.000	1.5614E-01	1.5882E-01	1.5077E-01	1.4825E-01	1.0105E-01	6.8129E-02
6.000	2.2692E-01	2.2732E-01	2.2348E-01	2.1655E-01	1.5806E-01	1.2088E-01
7.000	3.0426E-01	3.0967E-01	3.0031E-01	2.9458E-01	2.8170E-01	2.7067E-01
8.000	3.9891E-01	4.0168E-01	3.9403E-01	3.8955E-01	3.3267E-01	2.9215E-01
9.000	4.9924E-01	4.9971E-01	4.8981E-01	4.8739E-01	4.1575E-01	3.6752E-01
10.000	6.0954E-01	6.0913E-01	5.9994E-01	5.9723E-01	5.3840E-01	5.0007E-01
11.000	7.2007E-01	7.1884E-01	7.1036E-01	7.0737E-01	6.6139E-01	6.3300E-01

SKIN FRICTION(CF) & STANTON NO. (ST)

X	CF	ST	U1(W)/U2(CL)
1.00	1.6071E-05	-5.2580E-04	-3.2009E-01
2.00	9.0834E-06	-2.6062E-04	-1.6108E-01
3.00	6.6758E-06	-1.6765E-04	-1.0731E-01
4.00	4.7113E-06	-1.2481E-04	-8.0608E-02
5.00	3.8591E-06	-9.3045E-05	-6.4494E-02
6.00	3.2410E-06	-7.3240E-05	-5.3787E-02
7.00	2.7547E-06	-6.3609E-05	-4.6101E-02
8.00	2.3604E-06	-5.0464E-05	-4.0359E-02
9.00	2.0482E-06	-4.2344E-05	-3.5887E-02
10.00	1.7380E-06	-3.7332E-05	-3.2332E-02
11.00	1.5014E-06	-3.3357E-05	-2.9417E-02

Continued

R-RAP, AT DISTINCT AXIAL POSITIONS

RHO = DIM. LESS DENSITY

Y2	XZ= 0.0	XZ= 2.0000	XZ= 4.0000	XZ= 6.0000	XZ= 8.0000	XZ=10.0000
0.0	9.8137E-01	9.8653E-01	9.8658E-01	9.8656E-01	9.8658E-01	9.8665E-01
0.050	9.8137E-01	9.8653E-01	9.8658E-01	9.8656E-01	9.8658E-01	9.8665E-01
0.200	9.8133E-01	9.8653E-01	9.8652E-01	9.8653E-01	9.8654E-01	9.8669E-01
0.400	9.8111E-01	9.8641E-01	9.8640E-01	9.8641E-01	9.8638E-01	9.8660E-01
0.550	9.8133E-01	9.8667E-01	9.8665E-01	9.8660E-01	9.8663E-01	9.8678E-01
0.700	9.8118E-01	9.8664E-01	9.8655E-01	9.8660E-01	9.8663E-01	9.8679E-01
0.800	9.8135E-01	9.8666E-01	9.8666E-01	9.8663E-01	9.8670E-01	9.8686E-01
0.900	9.8131E-01	9.8653E-01	9.8657E-01	9.8655E-01	9.8657E-01	9.8680E-01
0.960	9.8181E-01	9.8689E-01	9.8676E-01	9.8699E-01	9.8701E-01	9.8717E-01
0.985	9.8198E-01	9.8657E-01	9.8623E-01	9.8631E-01	9.8600E-01	9.8569E-01
0.995	9.8198E-01	9.8461E-01	9.8389E-01	9.8336E-01	9.8218E-01	9.8077E-01
1.000	1.0000E+00	9.8190E-01	9.8094E-01	9.8030E-01	9.7878E-01	9.7694E-01

VR = DIM. LESS RADIAL VELOCITY

Y2	XZ= 0.0	XZ= 2.0000	XZ= 4.0000	XZ= 6.0000	XZ= 8.0000	XZ=10.0000
0.0	0.0	0.0	0.0	0.0	0.0	0.0
0.050	0.0	-9.4916E-02	-9.4648E-02	-9.7096E-02	-9.6149E-02	-9.6113E-02
0.200	0.0	-2.4820E-01	-2.4487E-01	-2.5339E-01	-2.5518E-01	-2.5297E-01
0.400	0.0	-8.0947E-01	-8.0589E-01	-8.0669E-01	-8.1320E-01	-8.0785E-01
0.550	0.0	-9.7119E-01	-9.6701E-01	-9.7080E-01	-9.8039E-01	-9.6403E-01
0.700	0.0	-1.1952E+00	-1.1947E+00	-1.1980E+00	-1.2012E+00	-1.1969E+00
0.800	0.0	-1.1660E+00	-1.1661E+00	-1.1627E+00	-1.1653E+00	-1.1675E+00
0.900	0.0	-1.1461E+00	-1.1614E+00	-1.1378E+00	-1.1373E+00	-1.1752E+00
0.960	0.0	-1.0278E+00	-1.0551E+00	-1.0118E+00	-1.0057E+00	-1.0771E+00
0.985	0.0	-1.0227E+00	-1.0343E+00	-1.0176E+00	-1.0155E+00	-1.0450E+00
0.995	0.0	-1.0188E+00	-1.0237E+00	-1.0192E+00	-1.0189E+00	-1.0305E+00
1.000	-1.0000E+00	-1.0184E+00	-1.0194E+00	-1.0201E+00	-1.0217E+00	-1.0236E+00

VX = DIM. LESS AXIAL VELOCITY

Y2	XZ= 0.0	XZ= 2.0000	XZ= 4.0000	XZ= 6.0000	XZ= 8.0000	XZ=10.0000
0.0	0.0	6.2929E+00	1.2574E+01	1.8845E+01	2.5115E+01	3.1348E+01
0.050	0.0	6.2929E+00	1.2574E+01	1.8845E+01	2.5115E+01	3.1348E+01
0.200	0.0	6.2794E+00	1.2547E+01	1.8805E+01	2.5057E+01	3.1274E+01
0.400	0.0	6.0096E+00	1.2169E+01	1.8240E+01	2.4303E+01	3.0332E+01
0.550	0.0	5.5849E+00	1.1161E+01	1.6732E+01	2.2291E+01	2.7820E+01
0.700	0.0	4.5071E+00	9.0119E+00	1.3519E+01	1.7997E+01	2.2453E+01
0.800	0.0	3.3570E+00	6.7178E+00	1.0075E+01	1.3417E+01	1.6717E+01
0.900	0.0	1.8378E+00	3.6810E+00	5.5279E+00	7.3526E+00	9.1419E+00
0.960	0.0	7.5780E-01	1.5228E+00	2.2930E+00	3.0407E+00	3.7468E+00
0.985	0.0	2.8026E-01	5.6903E-01	8.6322E-01	1.1352E+00	1.3641E+00
0.995	0.0	8.8714E-02	1.8374E-01	2.8389E-01	3.6721E-01	4.2128E-01
1.000	0.0	0.0	0.0	0.0	0.0	0.0

Continued

P = DIM. LESS STATIC PRESSURE

YZ	XZ= 0.0	XZ= 2.0000	XZ= 4.0000	XZ= 6.0000	XZ= 8.0000	XZ=10.0000
0.0	9.8137E-01	9.8114E-01	9.8047E-01	9.7935E-01	9.7782E-01	9.7596E-01
0.050	9.8137E-01	9.8114E-01	9.8047E-01	9.7935E-01	9.7782E-01	9.7596E-01
0.200	9.8133E-01	9.8113E-01	9.8044E-01	9.7934E-01	9.7780E-01	9.7596E-01
0.400	9.8111E-01	9.8094E-01	9.8025E-01	9.7913E-01	9.7755E-01	9.7581E-01
0.550	9.8133E-01	9.8124E-01	9.8052E-01	9.7938E-01	9.7787E-01	9.7605E-01
0.700	9.8110E-01	9.8123E-01	9.8051E-01	9.7935E-01	9.7785E-01	9.7594E-01
0.800	9.8135E-01	9.8129E-01	9.8059E-01	9.7944E-01	9.7791E-01	9.7607E-01
0.900	9.8131E-01	9.8109E-01	9.8044E-01	9.7926E-01	9.7768E-01	9.7591E-01
0.960	9.8101E-01	9.8164E-01	9.8078E-01	9.7996E-01	9.7841E-01	9.7659E-01
0.985	9.8198E-01	9.8187E-01	9.8093E-01	9.8027E-01	9.7875E-01	9.7691E-01
0.995	9.8198E-01	9.8189E-01	9.8094E-01	9.8029E-01	9.7877E-01	9.7693E-01
1.000	9.9999E-01	9.8198E-01	9.8094E-01	9.8030E-01	9.7878E-01	9.7694E-01

DIFFERENCES BETWEEN CURRENT TIMESTEP NO.1201
AND THE INITIAL DATA U(M,J,K)-UINITIAL(M,J,K) :

R-MAP, AT DISTINCT AXIAL POSITIONS

RHO = DIM. LESS DENSITY

YZ	XZ= 0.0	XZ= 2.0000	XZ= 4.0000	XZ= 6.0000	XZ= 8.0000	XZ=10.0000
0.0	-1.8634E-02	-1.3474E-02	-1.3424E-02	-1.3436E-02	-1.3425E-02	-1.3346E-02
0.050	-1.8634E-02	-1.3474E-02	-1.3424E-02	-1.3436E-02	-1.3425E-02	-1.3346E-02
0.200	-1.8672E-02	-1.3468E-02	-1.3482E-02	-1.3469E-02	-1.3462E-02	-1.3386E-02
0.400	-1.8887E-02	-1.3586E-02	-1.3598E-02	-1.3591E-02	-1.3624E-02	-1.3400E-02
0.550	-1.8675E-02	-1.3333E-02	-1.3354E-02	-1.3404E-02	-1.3368E-02	-1.3215E-02
0.700	-1.8816E-02	-1.3364E-02	-1.3451E-02	-1.3408E-02	-1.3367E-02	-1.3212E-02
0.800	-1.8647E-02	-1.3337E-02	-1.3339E-02	-1.3372E-02	-1.3383E-02	-1.3143E-02
0.900	-1.8689E-02	-1.3471E-02	-1.3438E-02	-1.3452E-02	-1.3438E-02	-1.3199E-02
0.960	-1.8193E-02	-1.3186E-02	-1.3239E-02	-1.3088E-02	-1.2994E-02	-1.2828E-02
0.985	-1.8023E-02	-1.3428E-02	-1.3778E-02	-1.3689E-02	-1.4002E-02	-1.4312E-02
0.995	-1.8021E-02	-1.5389E-02	-1.6114E-02	-1.6644E-02	-1.7821E-02	-1.9231E-02
1.000	0.0	-1.8183E-02	-1.9062E-02	-1.9782E-02	-2.1222E-02	-2.3064E-02

VR = DIM. LESS RADIAL VELOCITY

YZ	XZ= 0.0	XZ= 2.0000	XZ= 4.0000	XZ= 6.0000	XZ= 8.0000	XZ=10.0000
0.0	0.0	0.0	0.0	0.0	0.0	0.0
0.050	0.0	-1.6377E-02	-1.6189E-02	-1.8557E-02	-1.7689E-02	-1.7573E-02
0.200	0.0	6.5748E-02	6.9883E-02	6.8562E-02	5.8774E-02	6.8981E-02
0.400	0.0	-1.8775E-01	-1.8416E-01	-1.8497E-01	-1.9148E-01	-1.8612E-01
0.550	0.0	-1.3940E-01	-1.3522E-01	-1.3501E-01	-1.4860E-01	-1.3224E-01
0.700	0.0	-2.0184E-01	-2.0051E-01	-2.0382E-01	-2.0702E-01	-2.0271E-01
0.800	0.0	-1.1056E-01	-1.1065E-01	-1.0731E-01	-1.0994E-01	-1.1214E-01
0.900	0.0	-8.4158E-02	-9.9361E-02	-7.5805E-02	-7.5351E-02	-1.1319E-01
0.960	0.0	6.0110E-03	-2.1356E-02	2.1954E-02	2.8033E-02	-4.3362E-02
0.985	0.0	-8.5726E-03	-2.0153E-02	-3.4389E-03	-1.4185E-03	-3.0882E-02
0.995	0.0	-1.3935E-02	-1.8764E-02	-1.4344E-02	-1.3985E-02	-2.5578E-02
1.000	0.0	-1.8436E-02	-1.9432E-02	-2.0098E-02	-2.1682E-02	-2.3608E-02

Continued

VX = DIM. LESS AXIAL VELOCITY

YZ	XZ= 0.0	XZ= 2.0000	XZ= 4.0000	XZ= 6.0000	XZ= 8.0000	XZ=10.0000
0.0	0.0	1.5438E-03	6.4227E-04	-2.3314E-04	-7.1641E-04	-2.1643E-03
0.050	0.0	1.5508E-03	6.5001E-04	-2.2504E-04	-7.0052E-04	-2.1565E-03
0.200	0.0	1.3724E-03	3.9873E-04	-3.7075E-04	-1.0376E-03	-2.5446E-03
0.400	0.0	6.0500E-04	-2.0954E-04	-9.3336E-04	-1.5852E-03	-3.0052E-03
0.550	0.0	-3.5836E-04	-1.0218E-03	-1.5332E-03	-2.2949E-03	-3.6875E-03
0.700	0.0	-0.0596E-04	-9.0226E-04	-9.3594E-04	-2.0375E-03	-3.4140E-03
0.800	0.0	-1.5509E-03	-1.2396E-03	-1.3195E-03	-1.9693E-03	-3.7215E-03
0.900	0.0	-1.5503E-03	-1.1163E-03	-7.7586E-04	-1.4915E-03	-3.0464E-03
0.960	0.0	-2.2329E-03	-1.6592E-03	-1.1910E-03	-1.0538E-03	-3.5760E-03
0.985	0.0	-2.1492E-03	-1.4725E-03	-9.5097E-04	-1.5066E-03	-3.3346E-03
0.995	0.0	-1.5502E-03	-1.0483E-03	-6.0087E-04	-1.0586E-03	-2.2598E-03
1.000	0.0	0.0	0.0	0.0	0.0	0.0

P = DIM. LESS STATIC PRESSURE

YZ	XZ= 0.0	XZ= 2.0000	XZ= 4.0000	XZ= 6.0000	XZ= 8.0000	XZ=10.0000
0.0	-1.0628E-02	-1.0612E-02	-1.0566E-02	-1.0495E-02	-1.0346E-02	-1.0054E-02
0.050	-1.0628E-02	-1.0612E-02	-1.0566E-02	-1.0495E-02	-1.0346E-02	-1.0054E-02
0.200	-1.0666E-02	-1.0621E-02	-1.0597E-02	-1.0498E-02	-1.0370E-02	-1.0051E-02
0.400	-1.0881E-02	-1.0819E-02	-1.0790E-02	-1.0709E-02	-1.0617E-02	-1.0204E-02
0.550	-1.0669E-02	-1.0511E-02	-1.0513E-02	-1.0464E-02	-1.0303E-02	-1.7970E-02
0.700	-1.0010E-02	-1.0522E-02	-1.0532E-02	-1.0496E-02	-1.0317E-02	-1.0024E-02
0.800	-1.0641E-02	-1.0465E-02	-1.0445E-02	-1.0403E-02	-1.0263E-02	-1.7946E-02
0.900	-1.0683E-02	-1.0663E-02	-1.0598E-02	-1.0581E-02	-1.0491E-02	-1.0108E-02
0.960	-1.0187E-02	-1.0118E-02	-1.0260E-02	-1.7883E-02	-1.7759E-02	-1.7427E-02
0.985	-1.0017E-02	-1.7882E-02	-1.0108E-02	-1.7570E-02	-1.7421E-02	-1.7106E-02
0.995	-1.0015E-02	-1.7865E-02	-1.0102E-02	-1.7552E-02	-1.7400E-02	-1.7088E-02
1.000	0.0	-1.7858E-02	-1.0100E-02	-1.7544E-02	-1.7390E-02	-1.7080E-02

END OUTPUT

APPENDIX A

IAA'84

IAA-84-0289

**Nonlinear Combustion Instability in Solid
Propellant Motors: Visco-Acoustic Coupling**

M. Ben-Reuven, Princeton Combustion
Research Lab., Monmouth Junction, NJ

AIAA 22nd Aerospace Sciences Meeting

January 9-12, 1984/Reno, Nevada

UNCLASSIFIED

Recently Flandro [15] has carried out a theoretical analysis for a burning propellant in a cylindrical grain, under the effect of incident acoustic waves. Detailed formulation was derived with a double expansion, in terms of both inverse Reynolds number as well as Mach number (independent small parameters). The unsteady premixed combustion zone was considered near the propellant surface; an assumption is made, however, that flow within the combustion zone is purely radial, i.e., zero axial component to all orders. Thus it could be anticipated that the results resemble (regarding nonsteady combustion behavior) those of Flandro [16], and there seems to be only small differences between the response to tangential and to perpendicular wave incidence. The problem is finally solved iteratively, and details of the inner/outer matching process were not given.

In the remainder of this paper, the viscous, injected wall layer simulation is derived, in perturbation form. Analytical near field solutions are obtained for all variables up to second order, regarding the radial coordinate dependence; the remaining (x,t) -dependence is shown to be governed by a relatively simple partial differential system. These solutions are discussed, with particular attention to the resultant (first order) pressure distribution and wall shear stress, for which experimental data are available.

ANALYSIS

Analytical Model of the Coreflow

The equations of motion pertaining to the core-flow simulation are presented, for an axisymmetric flow field. The objective is to simulate the cold-flow experiments of Dr. Brown at UTC/CSD, which utilize cylindrical geometry. For the coreflow region, with typical injection Reynolds numbers of order 104, we assumed constant and uniform thermophysical properties. A schematic of the physical configuration is shown in Fig. 1. Turbulence and combustion are precluded from the present formulation, for reasons discussed earlier. Other than these simplifications, the full compressible, nonsteady, viscous equations of motion are considered, with all the dissipative terms included.

The five equations of motion, for continuity, radial momentum, axial momentum and energy are presented in differential form. A caloric equation of state (pertaining to perfect gas) completes the model to form closure of the dependent variables.

The following dimensionless independent variables are introduced, based on the two physical scales of reference inner chamber radius, R_0^* , and reference injection velocity, v_0^* :

$$r = r^*/R_0^*, \quad x = x^*/R_0^*, \quad t = t^*/t_0^* \quad (1)$$

$$\text{where } t_0^* = R_0^*/v_0^* \quad (2)$$

The dependent variables are:

$$\rho = \rho^*/\rho_0^*, \quad v = v^*/v_0^*, \quad u = u^*/v_0^*, \quad h = h^*/h_0^* \\ \text{and } p = p^*/p_0^* \quad (3)$$

In the last equations, the properties used for non-dimensionalization are the reference (injected) density, ρ_0^* , and the reference chamber pressure, p_0^* ; the corresponding thermal enthalpy, h_0^* , is calculated from the caloric equation of state,

$$p_0^* = \frac{\gamma-1}{\gamma} \rho_0^* h_0^* \quad (4)$$

where $\gamma = C_p/C_v$ is the specific heat ratio, is considered as constant. The reference speed of sound is

$$a_0^* = \left(\frac{\gamma p_0^*}{\rho_0^*} \right)^{1/2} = \sqrt{(\gamma-1)h_0^*} \quad (5)$$

UNCLASSIFIED

UNCLASSIFIED

being inviscid, could obtain a solution for the axial velocity component which satisfied the no-slip boundary condition at the wall. The solution which satisfies the boundary data, namely, $u(x=0)=0$, $u(r=1)=0$, and $v(r=1)=1$, yields:

$$v = -\sin\left(\frac{\pi}{2}r^2\right)/r$$

$$u = \pi x \cos\left(\frac{\pi}{2}r^2\right)$$

Of the general family of solutions obtainable, only that which allows full determination of the vorticity (the azimuthal component alone remains,) by the available boundary data, is physically meaningful; the rest were therefore rejected. The axial pressure distribution obtained from the momentum equation is parabolic,

$$[P_0 - P(x)]/\rho V_0^2 = \frac{\pi}{2}x^2$$

This type of injected flow field has been investigated previously both experimentally and theoretically. In particular the early theoretical work of Herman [2], who arrived at a power-series solution to the perturbation problem of suction in a flat, porous-walled channel, with the suction Reynolds number serving as small-perturbation quantity. The analytical results of G. Taylor [3] and Wageman and Guevara [4] more closely resemble the cosine terms of Culick [1]; both [3,4] have carried out experiments as well, and both demonstrated very good agreement between the measured axial velocity profiles and the calculated ones. It appears that Culick [1] has arrived at his results independently, since no reference was made to any of the previous works. In the experiments by Dunlap, Willoughby and Hermesen [5], the formulation derived by Culick [1] was used to correlate the measured data, again with considerable success, regarding the coreflow axial velocity profile, that is, away from the close neighborhood of the wall.

Other experiments by Olson and Eckert [6] and later by Huesman and Eckert [7] tend likewise to verify the validity of this formulation, in particular regarding the radial velocity profile, which indeed exhibits a peak near the porous surface [6], as well as the axial pressure distribution (the latter shown as a linear correlation between the friction coefficient, C_f , and the inverse mean axial velocity, which are both proportional to $1/x$).

The recent (and ongoing) experimental study by Brown, et al [8] provides valuable information regarding the steady state axial pressure profile and the axial velocity distribution, as well as nonsteady wall heat transfer (obtained by exciting the standing acoustic modes in the tube). Departure of the steady state data from the predictions of the aforementioned formulation by Culick [1] was attributed to possible transition to turbulence. As will be shown in this study, the pressure data obtained can be simulated very well with a first-order pressure perturbation, arising from the laminar viscous wall-layer analysis.

Earlier, Yagodkin [9] reported an experimental cold flow setup, with an injected porous pipe. The maximal injection Reynolds number was 250, which is 2-3 orders of magnitude less than that corresponding to actual internal rocket flows. Hot-wire anemometry was used to obtain axial velocity and axial velocity fluctuation vs axial and radial distance. Turbulence intensity seems to peak near the surface, and decrease toward the centerline and toward the pipe wall. These observations are qualitatively similar to those obtained later by Yamada, et al [10]. Although a transition region, at $Re_0=100-150$, was speculated [9] to involve "large eddy structures", no such evidence appears in the experimental data reported [9].

Further studies by Yagodkin, with Varapaev [11] and Sviridenkov [12] are theoretical, and address the problem of laminar stability of injected channel flows, i.e., transition to turbulence. Thus, modified versions of the Orr-Sommerfeld problem were investigated analytically [11] and numerically [12]. Two related laminar flow stability analyses are by Goldshtik, et al [13] and Alekseev, et al [14]. None of these theoretical analyses indicates the presence of large turbulent eddy structures prior to a full transition point, neither do they obtain an origin of such turbulence on the centerline upstream.

20th JANNAF Combustion Meeting, October 17-21, 1983, Monterey, CA

UNCLASSIFIED

FLUID-DYNAMICALLY COUPLED SOLID PROPELLANT COMBUSTION INSTABILITY - COLD FLOW SIMULATION*

Dr. Moshe Ben-Reuven
Princeton Combustion Research Laboratories, Inc.
Monmouth Junction, New Jersey

ABSTRACT

This analysis is aimed at the near-wall processes in an injected, axisymmetric, viscous flow. It is a part of an overall study of solid propellant rocket instability, in which cold flow simulation is evaluated as a tool to elucidate possible instability-driving mechanisms. One such prominent mechanism seems to be visco-acoustic coupling, as indicated by earlier detailed order of magnitude analysis. The major component of the overall study, not reported herein, involves numerical simulation of the full coreflow equations of motion (nonsteady, axisymmetric) by a modified MacCormack integration technique. The formulation is presented in terms of a singular boundary layer problem, with detail (up to second order) given only to the near-wall region. The injection Reynolds number is assumed large, and its inverse square root serves as an appropriate small-perturbation quantity. The injected Mach number is also small, and taken of the same order as the aforesaid small quantity. The radial-dependence of the inner solutions up to second order is solved, in polynomial form. This leaves the (x,t) dependence to much simpler partial differential equations. Particular results demonstrate the existence of a first-order pressure perturbation, which arises due to the dissipative near-wall processes. This pressure and the associated viscous friction coefficient are shown to agree very well with experimental injected flow data.

INTRODUCTION

This is part of a study aimed at elucidation of the physical mechanisms capable of driving acoustic instability in solid propellant motors, particularly of the type termed velocity-coupled instability. Previous studies on the coupling between velocity oscillations and the combustion process in solid propellant motors have demonstrated the complexity of the overall phenomenon, but have not yet defined the basic mechanisms nor how they operate under flow conditions prevailing in rocket chambers. Critical literature review and order of magnitude analyses of velocity coupling mechanisms have been carried out, including visco-acoustic coupling and turbulence combustion coupling. The major goal of the study is the analytical simulation of the interior flow field within a solid propellant grain. The focus is on the Stokes layer, with the objective of investigating the particular instability mechanism of visco-acoustic coupling. Preliminary analysis has indicated that this mechanism is both plausible and sufficiently powerful to drive nonlinear vibrations; it has been shown that the frequency-dependent surface heat feedback component, due to viscous/acoustic coupling, has both phase amplitude ranges which would enable driving of acoustic vibrations; its amplitude tends to increase as the mean coreflow Mach number and the frequency become higher. A comprehensive analytical model of the flow field within the viscous wall layer region has been derived, for an axisymmetric, nonsteady flow field configuration. For a simulation of the cold flow test results generated at UTC/CSD, four conservation equations are incorporated for continuity, momentum and energy.

The major aspect of the near-wall behavior from the visco-acoustic point of view, is the laminar dissipative processes typical to that region. This analysis is focused on the near-wall processes. Although the solutions derived are nonsteady in general, the radial wall-layer distributions obtained could best be demonstrated at steady state. For this reason, the review herein is limited to steady behavior.

Culick [1] derived a solution to the Stokes stream function equation or flow in a pipe with injected sidewalls. The flow is rotational, and despite

*This work was supported by the Air Force Office of Scientific Research, Bolling Air Force Base, Washington, DC, under Contract F49620-81-C-0018.

This paper is Unclassified. Distribution unlimited.

UNCLASSIFIED

APPENDIX B

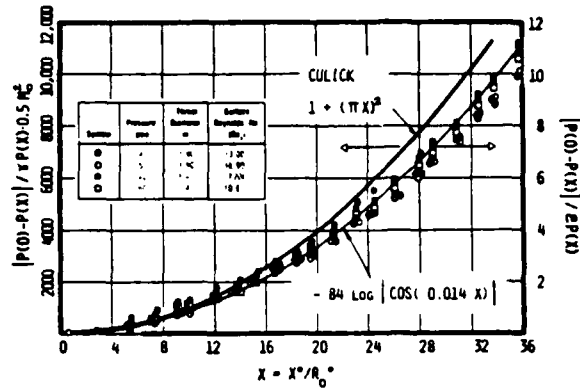


FIGURE 3. DIMENSIONLESS FIRST ORDER AXIAL PRESSURE DISTRIBUTION, FROM THE NEAR-FIELD ANALYSIS HEREIN. THE CURRENT RESULT IS PLOTTED OVER THE ORIGINAL FIGURE OF CSD/UTC (1982), WHICH ALSO SHOWS THE PARABOLIC FORMULA OF CULICK.

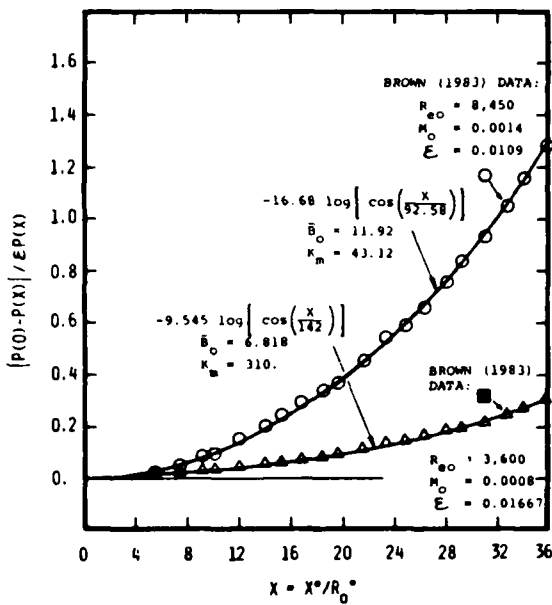


FIGURE 4. SENSITIVITY OF THE MEASURED AXIAL PRESSURE DROP TO REYNOLDS NO. (OR TO THE PARAMETERS K_m AND E HEREIN) IS DEMONSTRATED BY RE-SCALING OF TWO DISTINCT DATA GROUPS PLOTTED IN FIG. 3. EXCELLENT CORRELATIONS ARE OBTAINED BY USE OF EQ. (64).

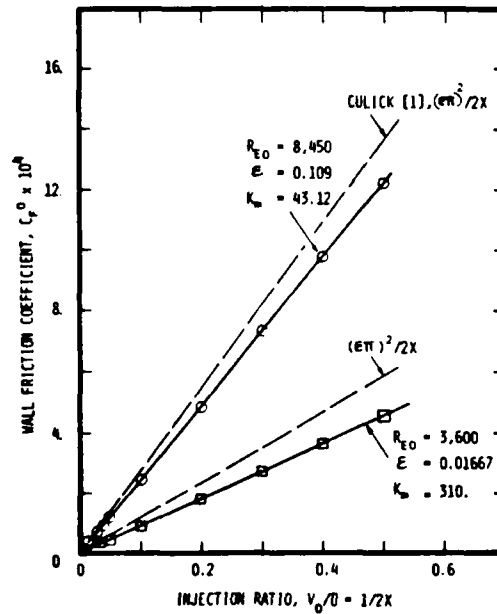


FIGURE 5. FRICTION COEFFICIENT CALCULATED FOR THE 2 CASES SHOWN IN FIG. 4. DEVIATIONS FROM LINEAR BEHAVIOR AT LARGE VALUES OF x ARE EVIDENT, IN AGREEMENT WITH THE MEASUREMENTS OF OLSON AND ECHERT[6] WHICH WOULD NOT BE POSSIBLE WITH PURE INVISCID THEORY.

as $U=2x$ was used, for a cylindrical port, and subscript zero denotes zeroth order convention.

Now, from Eqs. (29) and (62),

$$C_{f0} = \frac{E}{2} \left(\frac{\delta p_0}{\bar{S}_0} \cdot \frac{K_m}{F_0} \right)^{1/2} \cdot \frac{t_g \sqrt{b \cdot b_1} X}{X^2} \quad (66)$$

This parameter is plotted against $1/2x$ (which denotes the ratio of blowing to mean axial velocity) in Fig. 5. A nearly linear relationship is obtained, using the coefficient values obtained from the two data groups in Fig. 3. In comparison, the data obtained by Olson and Eckert [6] is considered. Ref. 6 includes a plot of the ratio of (axial pressure gradient)/(mean dynamic axial head) vs $v_0^*/u_0^* = 1/2x$. This obtains an almost linear correlation, as would be expected from a parabolic pressure drop. The slight curvature however, particularly apparent at small values of $1/2x < 0.01$, can be followed only with the present formulation, not with any parabolic pressure profile. Thus, the first order pressure distribution, obtained from the viscous wall layer analysis, agrees well with the measured data of Brown, et al [8], while the associated wall friction coefficient follows the same trend as that measured by Olson and Eckert [6].

CONCLUSIONS

A derivation of the viscous wall layer regime has been presented, pertaining to injected flow in an axial porous tube, in simulation of interior solid propellant rocket flows.

Solutions for the radial coordinate (or y-dependence) of all the dependent variables up to the first order have been generated, in polynomial form. The (x,t) -dependence is defined in terms of a relatively simple partial differential system.

Particular results of the analysis for the special case of steady state, are: (1) the first order pressure perturbation was solved for uniform B_0 , and its axial distribution is given explicitly; this term is entirely due to the laminar dissipative wall-layer processes, and (2) the blown wall friction coefficient was likewise defined. Both results correlate well the available experimental data. Finally, (3) the zeroth order axial velocity distribution within the layer is linear radially; thus, to lowest order, viscous dissipation is negligible in the axial momentum balance. This indicates why inviscid, rotational solutions (such as those of Culick [1] and others, chosen so as to satisfy the no-slip condition at the wall) are so successful in representing this family of flows - to zeroth order.

ACKNOWLEDGMENT

This study was supported by the U.S. Air Force Office of Scientific Research, Contract No. F49620-81-C-0018. Technical cognizance was provided by Dr. Leonard H. Cavenv.

REFERENCES

1. Culick, F.E.C., "Rotational, Axisymmetric Mean Flow and Damping of Acoustic Waves in a Solid Propellant Rocket", *AIAA Journal*, Vol. 4, No. 8, August 1966, pp. 1462-1464.
2. Berman, A.S., "Laminar Flow in Channels with Porous Walls", *Journal of Applied Physics*, Vol. 24, No. 9, September 1953, pp. 1232-1235.
3. Sir Geoffrey Taylor, "Fluid Flow in Regions Bound by Porous Surfaces", *Proc. Royal Soc. of London, Ser. A*, Vol. 234, No. 1199 (1956), pp. 456-475.
4. Wageman, W.E., and Guevara, F.A., "Fluid Flow Through a Porous Channel", *The Physics of Fluids*, Vol. 3, No. 6, November-December 1960, pp. 878-881.
5. Dunlap, R., Willoughby, P.G., and Hermesen, R.W., "Flowfield in the Combustion Chamber of a Solid Propellant Rocket Motor", *AIAA Journal*, Vol. 12, No. 10, October 1974, pp. 1440-1442.
6. Olson, R.M., and Eckert, E.R.G., "Experimental Studies of Turbulent Flow in a Porous Circular Tube with Uniform Fluid Injection Through the Tube Walls", *Jour. of Appl. Mech./Transactions of the ASME*, March 1966, pp. 7-17.
7. Huesman, R., and Eckert, E.R.G., "Studies of the Laminar Flow and Transition to Turbulence in Porous Tubes, with Uniform Injection Through the Tube Wall", (Translation), *Warme und Stoffubertrannung*, Bd. 1 (1968), pp. 2-9.
8. Brown, R.S., Waugh, R.C., Willoughby, P.G., and Dunlap, R., "Coupling Between Velocity Oscillations and Solid Propellant Combustion", 19th JANNAF Combustion Meeting, October 1982, CPIA Publication 366, Vol. 1, pp. 191-208.
9. Yagodkin, V.I., "Use of Channels with Porous Walls for Studying Flows Which Occur During Combustion of Solid Propellants", *Proc. 18th Aeronautics Congress*, Vol. 3, 1967, pp. 69-79. (Trans.)
10. Yamada, K. Goto, M., and Ishikawa, N., "Simulative Study on the Erosive Burning of Solid Rocket Motors", *AIAA Journal*, Vol. 14, No. 9, September 1976, pp. 1170-1177.
11. Varapaev, V.N. and Yagodkin, V.I., "Flow Instability in a Channel with Porous Walls", *AN, SSSR, Mekhanika Zhidkosti i Gaza*, Vol. 4, No. 5, pp. 91-95, 1969. (Trans.)
12. Sviridenkov, A.A., and Yagodkin, V.I., "Flow in the Initial Sections of Channels with Permeable Walls", *Izv. AN, SSSR, Mekhanika Zhidkosti i Gaza*, No. 5, pp. 43-48, September-October 1976 (Moscow). (Trans.)
13. Goldshtik, M.A., and Sapozhnikov, V.A., "Laminar Flow Stability in a Mass Force Field", *Izv. AN, SSSR, Mekhanika Zhidkosti i Gaza*, Vol. 3, No. 5, pp. 42-46, 1968.

The experimental data of Brown [8] also demonstrates, as evident in Fig. 3, that significant departures from the parabolic axial pressure-drop profile (as predicted by the inviscid formulation) evolve at sufficiently large x . In the meantime, departures from the self-similar cosine velocity profiles are evident, which become more appreciable with increasing x . Elucidation of the first-order pressure perturbation seems therefore highly important for proper understanding of this type of injected flows. This is undertaken in the remainder of the present section, for steady state.

To resolve the axial variation of p_1 by the wall layer formulation, the second compatibility condition in Eq. (51) can be used, corresponding to the y -term:

$$0 = -\frac{\partial}{\partial x} \left(\frac{B_0 U_0}{F_0} \right) + V_0 + \frac{C_1 - V_0 C_0}{F_0} + \frac{U_1}{\gamma P_0} \frac{\partial}{\partial x}. \quad (58)$$

For the special case of uniform (zeroth order) injection at steady state, the presence of a nonzero first-order pressure perturbation would imply physically a corresponding nonzero perturbation upon the mass flux injected, i.e.,

$$B_0 = F_1(0, x, t) \neq 0$$

as given by Eq. (42). Now at steady state, although B_0 is expected to vary with x , we will (as a first step), assume for simplicity that $B_0(x) = \bar{B}_0 = \text{const.}$

With the foregoing steady state assumptions, Eq. (58) can be readily turned into an ordinary differential equation, for $0 < x < L$:

$$\frac{d^2 p_1}{dx^2} + b_1 \left(\frac{dp_1}{dx} \right)^2 + b_0 = 0 \quad (59)$$

where uniform injection, $F_0 = \text{const.}$, was assumed; the coefficients are:

$$b_0 \equiv -\frac{F_0^2 / \bar{B}_0}{K_m / V_0} > 0, \quad b_1 \equiv -\frac{F_0 / \bar{B}_0}{\gamma P_0} > 0. \quad (60)$$

Note that at steady state, according to Eqs. (39) and (44), $C_1 - C_0 V_0 = 0$. The boundary data are,

$$dp_1/dx(0) = 0, \quad \text{and} \quad p_1(x=L) = p_L \quad (61)$$

The solution is straightforward; for positive b_1 and b_0 :

$$dp_1/dx = -\sqrt{\frac{b_0}{b_1}} \tanh(\sqrt{b_0 b_1} x) \quad (62)$$

$$p_1(x) = p_1(0) + \frac{1}{b_1} \ln |\cos(\sqrt{b_0 b_1} x)| \quad (63)$$

This concludes the derivation of the injected, viscous wall layer, up to second order. Full solutions, namely, matching between inner and outer expansions will not be attempted herein. Important insights are obtained already from resolving the near-field behavior up to second order, in terms of the y -polynomials.

DISCUSSION OF RESULTS

To facilitate comparison with the experimental data reported by Brown, et al [8], one may form the normalized axial pressure drop,

$$\frac{P(0) - P(x)}{\epsilon P(x)} = \frac{-1}{b_1 P_0} \ln |\cos(\sqrt{b_0 b_1} x)| + O(\epsilon) \quad (64)$$

This formula is used to correlate the experimental data of Brown, et al [8], as shown in Fig. 3. Clearly, the measured pressure profile is correlated very well by Eq. (64), which is obviously superior to the inviscid expression [1], shown as well.

A single point of the data (x ; p_1) has been utilized to obtain a scale for the comparison (this is necessary, since no physical input is available regarding the value of B_0 , the injected mass flux perturbation, necessary for defining b_1 , b_0), along with $p_0=1$, $F_0=V_0=1$, and $\gamma=1.4$. Suppose now that $R_m=1$, and we select a value of $B_0=60$. (This is based on some trial and error - but shows how the correlation was obtained without any regression analysis); then,

$$b_0 = 1/B_0 = 1/60, \quad b_1 = 1/\gamma B_0 = 1/1.4 \times 60, = 0.012$$

$$b_0 b_1 = 1/\sqrt{\gamma} B_0 = 0.014$$

To demonstrate the sensitivity of the axial pressure drop to Reynolds number (or to the parameters R_m and ϵ), the experimental points of Fig. 3 were converted from their original scale,

$$\Delta P / \frac{1}{2} \gamma P M_0^2,$$

to the $\Delta p_1/\epsilon$ -form herein, using the relevant values of M_0 and R_{e0} given. The results of this conversion, for two distinct data groups, are plotted in Fig. 4, along with their excellent correlation by Eq. (64).

In Fig. 4, the differences between high R_m (low R_{e0}) and low R_m (high R_{e0}) are amplified. High R_{e0} measurements appear on top, closest to the inviscid pressure profile.

Two important observations can therefore be made: (1) axial pressure variation to lowest order is $O(\epsilon)$, and is governed by the dissipative wall layer processes, as derived in the analysis herein. The behavior obtained in x differs from the parabolic pressure drop formula of Culick [1]; also, (2) one need not invoke local turbulence generation to explain the departure of measured p_1 from the predicted inviscid behavior.

Another property of interest is the wall friction coefficient, or dimensionless wall shear stress,

$$C_f = \tau_w^* / \frac{1}{2} \rho^* \bar{u}^{*2} = \mu^* \frac{\partial u^*}{\partial y} / \frac{1}{2} \rho^* \bar{u}^{*2}$$

where \bar{u}^* denotes the mean axial coreflow velocity. Using dimensionless convention employed herein, along with the wall layer coordinate,

$$C_{f0} = \epsilon \frac{\partial u_0}{\partial y} / 2x^2 \quad (65)$$

Thus, $h_1(y, x, t)$ is second order in y , like φ_1 ; the appropriate boundary condition is,

$$B_2(x, t) = h_1(0, x, t) - h_0(B_0 - \varphi_0 B_1)/F_0 \quad (48)$$

The axial momentum balance, Eq. (33), after dividing through by F_0 and following integration, yields:

$$u_1(x, t; y) = \frac{U_0}{F_0} \left[\varphi_0 \frac{\partial u_0}{\partial x} - \frac{1}{2} \frac{\partial (\varphi_0 u_0)}{\partial x} \right] y^{3/3} + \left(\frac{1}{V_0} \frac{\partial u_0}{\partial x} - \frac{C_1 U_0}{F_0} \right) y^{1/2} - \frac{B_2 U_0}{F_0} y \quad (49)$$

and

$$u_1(0, x, t) = 0$$

satisfying the no-slip condition at the wall. Thus, the perturbed axial velocity is third order in its y -dependence, and the corresponding viscous dissipation term (unlike its zeroth-order counterpart), does not vanish within the layer.

With the foregoing derived results, the zeroth order energy equation can be shown to yield merely a condition connecting U_0 and V_0 timewise. One may turn now to the first-order energy equation, which seems to yield some simple and highly useful results even without full solution. After some manipulation, Eq. (38) obtains:

$$\frac{\partial p_1}{\partial t} + \gamma p_1 \left(\frac{\partial u_0}{\partial x} - \frac{\gamma_1}{\gamma} + V_0 \right) + \gamma p_0 \left(\frac{\partial u_1}{\partial x} + V_0 y + V_1 \right) + u_0 \frac{\partial p_1}{\partial x} - \frac{\gamma-1}{\gamma} \frac{\partial^2 h_1}{\partial y^2} = 0 \quad (50)$$

The first bracketed term, after using the foregoing results, is simply

$$V_0 - (C_1 - V_0 C_0)/F_0$$

Using the appropriate first order expressions obtained herein (for u_1 , v_1 , and h_1) in Eq. (50), and collection of equal powers of y yields:

$$\begin{aligned} & \gamma p_0 \left\{ \frac{1}{F_0} \frac{\partial p_1}{\partial t} + \frac{p_1}{F_0} \left(V_0 - \frac{C_1 - V_0 C_0}{F_0} \right) - \frac{1}{F_0} \frac{\partial}{\partial x} (p_0 u_0) + B_0 \right\} + \\ & \gamma p_0 \left\{ - \frac{\partial}{\partial x} \left(\frac{B_0 u_0}{F_0} \right) + V_0 + \frac{C_1 - V_0 C_0}{F_0} + \frac{U_0}{F_0} \frac{\partial p_1}{\partial x} \right\} y + \\ & \gamma p_0 \left\{ \frac{U_0}{V_0} \frac{\partial V_0}{\partial x} + \frac{\partial}{\partial x} \left(\frac{1}{V_0} \frac{\partial u_0}{\partial t} - \frac{C_0 u_0}{F_0} \right) \right\} y^{1/2} + \\ & \frac{\partial}{\partial x} \left\{ \frac{U_0}{V_0} \frac{p_0}{2} \frac{\partial (u_0 \varphi_0)}{\partial x} \right\} y^{3/3} = 0 \end{aligned} \quad (51)$$

Compatibility with the foregoing derivation (in which y and (x, t) variable separation was implemented), can be maintained, provided each of the bracketed terms in Eq. (51) vanishes identically. The resulting four compatibility relations, in partial differential form, would determine the behavior of the wall sublayer system up to the first order in ϵ , the small perturbation quantity. However, a total of three

undetermined coefficients should arise necessarily, to accommodate coupling with the outer, inviscid (core) flowfield, through inner/outer asymptotic matching.

THE FIRST ORDER PRESSURE PERTURBATION

In the outer inviscid flow (coreflow), the pressure difference is balanced by the axial acceleration, as

$$[p^*(0) - p^*(x)] / \frac{1}{2} \varphi_0^* \bar{u}^{*2} \sim O(1) \quad (52)$$

In the meantime, the available CSD experimental data clearly shows that the seemingly equivalent representation,

$$[p^*(0) - p^*(x)] / \frac{1}{2} \gamma p^*(x) M_0^2 \sim \left(\frac{L^*}{R^*} \right)^2 \sim O\left(\frac{1}{\epsilon}\right) \quad (53)$$

where $0 < \epsilon \ll 1$. Therefore, within the range of flow conditions simulated herein, it is inferred that the mean axial coreflow velocity can become considerably larger than the radial (or injected) velocity, such that, from Eqs. (52) and (53):

$$u^*(OUTER)/V_0^*(INJECTION) \sim O\left(\frac{1}{\sqrt{\epsilon}}\right) \quad (54)$$

and furthermore,

$$[p^*(0) - p^*(x)] / p^*(x) \sim M_0 \sim O(\epsilon).$$

Recall that $p_0 = p_0(t)$ and $p_1 = p_1(x, t)$ as derived in wall layer analysis. Hence, up to first order, no radial pressure gradients arise, and the inner and outer pressures must be equal, viz.,

$$p_0(0) = p_0(1), \quad p_1(0) = p_1(1) \quad (55)$$

Suppose now that the leading term in the outer axial velocity expansion is, according to Eq. (54),

$$u^{(0)}(x, r, t) \sim \frac{u_{-1}^{(0)}}{\sqrt{\epsilon}} + u_0^{(0)} + h.o.t. \quad (56)$$

while the remaining outer variables are of simpler form, e.g.,

$$v^{(0)}(x, r, t) \sim V_0^{(0)} + \sqrt{\epsilon} V_1^{(0)} + h.o.t.$$

Therefore, the outer axial momentum balance, derived from Eqs. (7)-(12) yields, at order $1/\epsilon$:

$$\frac{\partial}{\partial x} \left\{ \varphi_0^{(0)} u_{-1}^{(0)} u_1^{(0)} + K_m p_1^{(0)} \right\} = 0 \quad (57)$$

which shows that indeed the outer flow can support this first-order pressure perturbation. To conclude, a first-order pressure perturbation within the flow field, $\epsilon p_1(x, t)$, has been postulated, following the viscous wall layer analysis. This pressure is common to both inner (wall layer) and outer (coreflow) regions. Within the wall layer, it is balanced by the shear force, or zeroth-order vorticity generation, as shown in Eq. (28). In the coreflow, it is balanced by the lowest-order axial acceleration.

position (x, t) . Even more striking is the vanishing of the viscous dissipation term at zeroth order:

$$\partial^2 u_0 / \partial y^2 = 0$$

which leaves in the zeroth-order axial momentum equation a balance of inertial terms, strictly. This explains physically the success (up to first order) of modeling this family of injected flows by assuming rotational, inviscid motions; such modeling indeed obtains solutions for the axial velocity profile, which satisfy the no-slip condition at the wall $(r=1)$.

It further appears that the shear stress, Eq. (30), is proportional to the first-order axial pressure gradient, while being inversely proportional to the injected mass flux, as would be expected. Of course, $\partial p_1 / \partial x$ depends on F_0 , and one expects their ratio to be finite at the limit as zero injection is approached.

The zeroth-order differential system reads:

$$\frac{\partial F_0}{\partial t} + \frac{\partial G_0}{\partial x} - \frac{\partial F_1}{\partial y} = -F_2 \quad (31)$$

$$\frac{\partial F_0}{\partial t} + \frac{\partial}{\partial x} (F_0 u_0) - \frac{\partial}{\partial y} (F_0 v_1 + F_1 v_0) = -F_0 v_0 + \frac{4}{3} \frac{\partial^2 v_0}{\partial y^2} \quad (32)$$

$$\frac{\partial G_0}{\partial t} + \frac{\partial G_0 u_0}{\partial x} - \frac{\partial}{\partial y} (G_0 v_1 + G_1 v_0) = -G_0 v_0 + \partial^2 u_0 / \partial y^2 \quad (33)$$

$$\frac{\partial F_1}{\partial t} + \frac{\partial}{\partial x} (F_1 u_0) - \frac{\partial}{\partial y} (F_1 v_0 + F_0 v_1) = -F_0 v_0 + (1-\gamma) \left[u_0 \frac{\partial F_0}{\partial x} - (v_1 \frac{\partial F_0}{\partial y} + v_0 \frac{\partial F_1}{\partial y}) \right] + \frac{\gamma}{F_0} \frac{\partial^2 h_0}{\partial y^2} \quad (34)$$

The corresponding first-order formulation reads:

$$\frac{\partial F_1}{\partial t} + \frac{\partial G_1}{\partial x} - \frac{\partial F_2}{\partial y} = -F_1 - \gamma F_0 \quad (35)$$

$$\frac{\partial F_1}{\partial t} + \frac{\partial}{\partial x} (F_0 u_1 + F_1 u_0) - \frac{\partial}{\partial y} [v_1 (F_1 + F_0 v_0)] = -[F_0 v_0 y + (F_0 v_1 + F_1 v_0)] + \frac{4}{3} \frac{\partial^2 v_1}{\partial y^2} + \frac{4}{3} \frac{\partial v_1}{\partial y} - \frac{1}{3} \frac{\partial^2 u_0}{\partial x \partial y} \quad (36)$$

$$\frac{\partial G_1}{\partial t} + \frac{\partial}{\partial x} (G_0 u_1 + G_1 u_0) - \frac{\partial}{\partial y} (G_1 v_1 + F_1 v_0 u_1) = -(G_1 v_0 + G_0 v_1) - G_0 v_0 y + \frac{\partial^2 u_1}{\partial y^2} - \frac{\partial u_1}{\partial y} - \frac{1}{3} \frac{\partial^2 v_0}{\partial x \partial y} \quad (37)$$

$$\frac{\partial F_1}{\partial t} + \frac{\partial}{\partial x} (F_1 u_0 + F_0 u_1) - \frac{\partial}{\partial y} (F_1 v_1) = -F_0 v_0 y + \gamma (F_0 v_1 + F_1 v_0) + \frac{\gamma}{F_0} \left(-\frac{\partial h_0}{\partial y} + \frac{\partial h_1}{\partial y} \right) + (\gamma-1) \left(u_1 \frac{\partial F_0}{\partial x} + u_0 \frac{\partial F_1}{\partial x} - v_1 \frac{\partial F_1}{\partial y} \right) \quad (38)$$

With the foregoing result for axial velocity, the zeroth order formulation can be utilized to solve for the y -dependence of the other dependent variables. The zeroth order continuity equation can be written in split form, since F_0 and G_0 are independent of y :

$$\partial F_0 / \partial t + F_0(x, t) = C_0(x, t) \quad (39)$$

$$\frac{\partial}{\partial x} \left(\frac{K_{xy}}{V_0} \frac{\partial F_1}{\partial x} \right) y - \frac{\partial F_1}{\partial y} = -C_0(x, t) \quad (40)$$

where $C_0(x, t)$ is a common separation parameter, with a range of values uniquely corresponding to the boundary data. The second equation yields

$$F_1(y, x, t) = B_0(x, t) + C_0(x, t) y + \frac{1}{2} \frac{\partial}{\partial x} (K_{xy}) y^2 \quad (41)$$

where:

$$B_0(x, t) = F_1(0, x, t) \quad (42)$$

$$u_0(x, t) = \frac{K_{xy}}{F_0} \partial F_1 / \partial x \quad (43)$$

Similarly, the zeroth order radial momentum equation yields, after splitting:

$$\partial F_0 / \partial t + F_0 v_0 = C_1(x, t) \quad (44)$$

$$v_1(x, t; y) = B_1(x, t) + \frac{C_1 - v_0 C_0}{F_0} y + \frac{1}{2} v_0 \cdot \frac{1}{V_0} \frac{\partial v_0}{\partial x} y^2$$

$$B_1(x, t) = v_1(x, t; 0) \quad (45)$$

The foregoing results for F_1 and v_1 yield for the first-order density:

$$\rho_1(x, t; y) = (B_0 - F_0 B_1) / V_0 + (2C_0 - C_1 / v_0) y + \frac{1}{2} \frac{K_{xy}}{V_0^2} \left[\frac{\partial^2 F_1}{\partial x^2} - 2 \frac{\partial F_1}{\partial x} \frac{\partial \ln v_0}{\partial x} \right] y^2 \quad (46)$$

Note that: $\rho_1(0, x, t) = (B_0 - F_0 B_1) / V_0$

so that ρ_1 is uniquely defined and an additional integration constant is not necessary. Now, following the definition of ρ_1 and since

$$\partial \rho_1 / \partial y = \partial h_0 / \partial y = \partial \rho_0 / \partial y = 0,$$

then:

$$h_1(y; x, t) = \frac{h_0}{F_0} \rho_1(y; x, t) + B_2(x, t) \quad (47)$$

(c) At the (nonpermeable solid) head-end closure, $(t, r, x=0)$:

$$v = 0, \quad u = 0, \quad h = h_H(r, t) \quad (16)$$

The functions $v_0(x, t)$, $h_0(x, t)$ and $h_H(r, t)$ are arbitrary imposed distributions.

(d) The exit plane, defined by $(t, r, x=L)$, forms an entrance into a short, convergent nozzle section.

THE INJECTED SIDEWALL LAYER

The flow region of interest is close to the surface, where viscous forces are expected to be appreciable within a thin layer.

For the neighborhood of $r=1$, the following transform is proposed for the radial coordinate:

$$y = (1-r)/\epsilon \quad (17)$$

which magnifies the wall layer, with

$$0 < \epsilon \equiv 1/\sqrt{Re_0} \ll 1 \quad (18)$$

Thus,

$$\partial/\partial r = -\frac{1}{\epsilon} \frac{\partial}{\partial y}, \quad \partial^2/\partial r^2 = \frac{1}{\epsilon^2} \frac{\partial^2}{\partial y^2} \quad (19)$$

and

$$r = 1 - \epsilon y$$

The assumption for small injection Mach number is constrained as follows. Obviously, the injection Mach number appears as an additional parameter in the formulation (equations of momentum and energy). In the flow types of interest for simulation herein, M_0 is also very small; in consideration of typical experimental configurations at CSD/UTC, we find

$$M_0^2 \sim O(1/Re_0) \sim O(\epsilon^2)$$

which adequately represents a range of cold-flow conditions. This offers great simplification in the analysis, although at the cost of narrower range of general application (considering the relative freedom of the two major flow parameters, Re_0 and M_0). Therefore, a parameter is introduced,

$$K_m \equiv \frac{1/Re_0}{\partial M_0^2} = \frac{\epsilon^2}{\gamma M_0^2} \sim O(1) \quad (20)$$

The question of timescale depends upon the range of frequencies of interest. The following reasoning will demonstrate that for the range of conditions considered for the present simulation, the timescale can remain the same one as in the coreflow. The viscous layer thickness is

$$\delta_v \sim R_0^*/\sqrt{Re_0} \quad (21)$$

The Stokes Layer thickness (for acoustic perturbations with a frequency f_0)

$$\delta_{STO} \sim (\nu/f_0)^{1/2} \quad (22)$$

The ratio of these two thickness scales is,

$$\delta_v/\delta_{STO} \sim \sqrt{f_0 R_0^*/\nu} = \sqrt{S_{RO}} \quad (23)$$

where S_{RO} is the relevant (injection) Strouhal number. The range of Strouhal numbers considered is $S_{RO} \sim O(1)$, so one need not introduce any additional timescales.

The independent variables are (x, y, t) , while the associated dependent variables, in the wall-layer, are perturbed,

$$\begin{aligned} \rho &= \rho_0 + \epsilon \rho_1, \quad v = v_0 + \epsilon v_1, \quad u = u_0 + \epsilon u_1, \\ h &= h_0 + \epsilon h_1, \end{aligned} \quad (24)$$

while the following abbreviations are introduced,

$$\begin{aligned} F_0 &\equiv \rho_0 v_0, \quad F_1 \equiv \rho_0 v_1 + \rho_1 v_0, \\ G_0 &\equiv \rho_0 u_0, \quad G_1 \equiv \rho_0 u_1 + \rho_1 u_0 \end{aligned} \quad (25)$$

It should be stressed that the $O(\epsilon)$ terms represent perturbation quantities which may be later considered as series expansions. The present analysis is concerned with the two lowest orders only. This in no way implies limitation to so-called "linear" considerations.

For the perturbation variables of Eqs. (17)-(25), the continuity equation yields

$$\begin{aligned} \frac{\partial}{\partial x}(\rho_0 + \epsilon \rho_1) - \frac{1}{\epsilon} \frac{\partial}{\partial y}(F_0 + \epsilon F_1 + \epsilon^2 F_2) + \\ \frac{\partial}{\partial x}(G_0 + \epsilon G_1) = -(1 + \epsilon y)(F_0 + \epsilon F_1) \end{aligned} \quad (26)$$

Similar substitution of perturbed variables is also carried out for the remaining equations of motion; a detailed derivation is available in Ref. 17. A hierarchy of equations can then be collected, for equal powers of the small quantity ϵ .

The lower-order analysis (concerning negative powers of ϵ) readily yields the following simple results:

$$\begin{aligned} F_0 &= F_0(x, t), \quad v_0 = v_0(x, t), \quad \rho_0 = \rho_0(t), \\ P_1 &= P_1(x, t) \end{aligned} \quad (27)$$

Also, the following differential equation arises from the axial momentum balance at order $1/\epsilon$:

$$K_m \frac{\partial P_1}{\partial x} - \frac{\partial}{\partial y}(F_0 u_0) = 0 \quad (28)$$

which can be integrated to reveal the y -dependence of u_0 :

$$u_0(x, t; y) = \frac{K_m}{F_0} \left(\partial P_1 / \partial x \right) y \quad (29)$$

with

$$u_0(x, t; 0) = 0.$$

Of course, the (x, t) dependence of u_0 still remains to be found. However, its dependence upon the layer coordinate, y , is found to be linear; this result has several important implications. The axial shear stress component within the layer,

$$\tau_{xy} \sim \frac{\partial u_0}{\partial y} = \frac{K_m}{F_0} \frac{\partial P_1}{\partial x}, \quad (30)$$

is obviously nonzero in general, while being independent of distance from the wall at any given

ANALYSIS

Analytical Model of the Coreflow

The equations of motion pertaining to the core-flow simulation are presented, for an axisymmetric flow field. The objective is to simulate the cold-flow experiments of Dr. Brown at UTC/CSD, which utilize cylindrical geometry. For the coreflow region, with typical injection Reynolds numbers of order 10^4 , we assumed constant and uniform thermophysical properties. A schematic of the physical configuration is shown in Fig. 1. Turbulence and combustion are precluded from the present formulation, for reasons discussed earlier. Other than these simplifications, the full compressible, nonsteady, viscous equations of motion are considered, with all the dissipative terms included.

The five equations of motion, for continuity, radial momentum, axial momentum and energy are presented in differential form. A caloric equation of state (pertaining to perfect gas) completes the model to form closure of the dependent variables.

The following dimensionless independent variables are introduced, based on the two physical scales of reference inner chamber radius, R_0^* , and reference injection velocity, v_0^* :

$$r = r^*/R_0^*, \quad x = x^*/R_0^*, \quad t = t^*/t_0^* \quad (1)$$

where $t_0^* = R_0^*/v_0^*$

The dependent variables are:

$$\begin{aligned} v &= v^*/v_0^*, \quad u = u^*/v_0^*, \\ \rho &= \rho^*/\rho_0^*, \quad h = h^*/h_0^*, \quad p = p^*/p_0^* \end{aligned} \quad (2)$$

The properties used for non-dimensionalization are the reference (injected) density, ρ_0^* , and the reference chamber pressure, p_0^* ; the corresponding thermal enthalpy, h_0^* , is calculated from the caloric equation of state,

$$p_0^* = \frac{\gamma-1}{\gamma} \rho_0^* h_0^* \quad (3)$$

where $\gamma = C_p/C_v$ is the specific heat ratio, is considered a constant. The reference speed of sound is

$$a_0^* = (\gamma p_0^*/\rho_0^*)^{1/2} = \sqrt{(\gamma-1)h_0^*} \quad (4)$$

The corresponding injection Mach number is

$$M_0 = v_0^*/a_0^* \quad (5)$$

The reference (injection) Reynolds number, and Prandtl number are, respectively,

$$Re_0 = \frac{\rho_0^* v_0^* R_0^*}{\mu^*}, \quad Pr = \mu^* C_p / \lambda^* \quad (6)$$

Recall that the viscosity, thermal conductivity and isobaric specific heat are all uniform and constant within the present cold-flow simulation.

These idealizations are incorporated merely for convenience, in allowing clear identification of physical interactions within the coreflow, at low (axial) Mach numbers; sharp pressure and temperature variations are obviously precluded. The dimensionless equations of motion are as follows, for the region

$$0 < x < 1, \quad 0 < r < 1, \quad t > 0:$$

$$\frac{\partial U}{\partial t} + \frac{1}{r} \frac{\partial}{\partial r}(rF) + \frac{\partial G}{\partial x} = S \quad (7)$$

where the dependent variable vector is,

$$U^T = (\rho, \rho v, \rho u, \rho h) \quad (8)$$

The radial and axial flux terms are, respectively,

$$F^T = (\rho v, \rho v^2, \rho uv, \gamma \rho hv) \quad (9)$$

$$G^T = (\rho u, \rho vu, \rho u^2 + \frac{p}{M_0^2}, \gamma \rho hu) \quad (10)$$

where superscript T denotes vector transpose. The right-hand side (source) terms are defined: $S_1=0$,

$$\begin{aligned} S_2 &= \frac{4/3}{Re_0} \frac{1}{r} \left(\frac{\partial v}{\partial r} - \frac{v}{r} \right) - \frac{1}{\partial x^2} \frac{\partial \rho}{\partial r} + \\ &\left[\frac{\partial^2 v}{\partial x^2} + \frac{1}{3} \frac{\partial}{\partial r} \left(\frac{\partial u}{\partial x} + 4 \frac{\partial v}{\partial r} \right) \right] \cdot \frac{1}{Re_0} \end{aligned} \quad (11)$$

$$\begin{aligned} S_3 &= \frac{1/r}{Re_0} \left(\frac{\partial u}{\partial r} + \frac{1}{3} \frac{\partial v}{\partial x} \right) + \\ &\left[\frac{\partial^2 u}{\partial x^2} + \frac{1}{3} \frac{\partial}{\partial x} \left(\frac{\partial u}{\partial x} + \frac{\partial v}{\partial r} \right) \right] \cdot \frac{1}{Re_0} \end{aligned} \quad (12)$$

$$\begin{aligned} S_4 &= \gamma \left(v \frac{\partial \rho}{\partial r} + u \frac{\partial \rho}{\partial x} \right) + \frac{\gamma Pr}{Re_0} \left(\frac{1}{r} \frac{\partial h}{\partial r} + \frac{\partial^2 h}{\partial r^2} + \frac{\partial^2 h}{\partial x^2} \right) + \\ &\frac{\gamma(\gamma-1)M_0^2}{Re_0} \left\{ \frac{4}{3} \left[\left(\frac{\partial u}{\partial x} \right)^2 + \left(\frac{\partial v}{\partial r} \right)^2 + \left(\frac{v}{r} \right)^2 \right] - \right. \\ &\left. \frac{4}{3} \left[\left(\frac{\partial v}{\partial r} - \frac{v}{r} \right) \frac{\partial u}{\partial x} + \frac{v}{r} \frac{\partial v}{\partial r} \right] + \right. \\ &\left. \left(\frac{\partial u}{\partial r} + \frac{\partial v}{\partial x} \right)^2 \right\} \end{aligned} \quad (13)$$

The following physical boundary data are available, for the cold-flow simulation:

(a) On the centerline, $(t, r=0, x)$:

$$v=0, \quad \frac{\partial u}{\partial r}=0, \quad \frac{\partial \rho}{\partial r}=0, \quad \frac{\partial h}{\partial r}=0. \quad (14)$$

(b) At the porous (injected) surface, $(t, r=1, x)$:

$$v = -v_0(x, t), \quad u = 0, \quad h = h_0(x, t) \quad (15)$$

The major aspect of the near-wall behavior from the visco-acoustic point of view, is the laminar dissipative processes typical to that region. This analysis is focused on the near-wall processes. Although the solutions derived are nonsteady in general, the radial wall-layer distributions obtained could best be demonstrated at steady state. For this reason, the review herein is limited to steady behavior.

Culick [1] derived a solution to the Stokes stream function equation or flow in a pipe with injected sidewalls. The flow is rotational, and despite being inviscid, could obtain a solution for the axial velocity component which satisfied the no-slip boundary condition at the wall. The solution which satisfies the boundary data, namely, $u(x=0)=0$, $u(r=1)=0$, and $v(r=1)=1$, yields:

$$V = -\sin\left(\frac{\pi}{2}r^2\right)/r$$

$$u = \pi x \cos\left(\frac{\pi}{2}r^2\right)$$

Of the general family of solutions obtainable, only that which allows full determination of the vorticity (the azimuthal component alone remains,) by the available boundary data, is physically meaningful; the rest were therefore rejected. The axial pressure distribution obtained from the momentum equation is parabolic,

$$[p^*(0) - p^*(x)] / \frac{1}{2} \rho^* V^*{}^2 = (\pi x)^2$$

This type of injected flow field has been investigated previously both experimentally and theoretically. In particular the early theoretical work of Berman [2], who arrived at a power-series solution to the perturbation problem of suction in a flat, porous-walled channel, with the suction Reynolds number serving as small-perturbation quantity. The analytical results of G. Taylor [3] and Wageman and Guevara [4] more closely resemble the cosine terms of Culick [1]; both [3,4] have carried out experiments as well, and both demonstrated very good agreement between the measured axial velocity profiles and the calculated ones. It appears that Culick [1] has arrived at his results independently, since no reference was made to any of the previous works. In the experiments by Dunlap, Willoughby and Hermesen [5], the formulation derived by Culick [1] was used to correlate the measured data, again with considerable success, regarding the coreflow axial velocity profile, that is, away from the close neighborhood of the wall.

Other experiments by Olson and Eckert [6] and later by Huesman and Eckert [7] tend likewise to verify the validity of this formulation, in particular regarding the radial velocity profile, which indeed exhibits a peak near the porous surface [6], as well as the axial pressure distribution (the latter shown as a linear correlation between the friction coefficient, C_f , and the inverse mean axial velocity, which are both proportional to $1/x$).

The recent (and ongoing) experimental study by Brown, et al [8] provides valuable information regarding the steady state axial pressure profile and the axial velocity distribution, as well as nonsteady wall heat transfer (obtained by exciting the standing acoustic modes in the tube).

Departure of the steady state data from the predictions of the aforementioned formulation by Culick [1] was attributed to possible transition to turbulence. As will be shown in this study, the pressure data obtained can be simulated very well with a first-order pressure perturbation, arising from the laminar viscous wall-layer analysis.

Earlier, Yagodkin [9] reported an experimental cold flow setup, with an injected porous pipe. The maximal injection Reynolds number was 250, which is 2-3 orders of magnitude less than that corresponding to actual internal rocket flows. Hot-wire anemometry was used to obtain axial velocity and axial velocity fluctuation vs axial and radial distance. Turbulence intensity seems to peak near the surface, and decrease toward the centerline and toward the pipe wall. These observations are qualitatively similar to those obtained later by Yamada, et al [10]. Although a transition region, at $Re_{in}=100-150$, was speculated [9] to involve "large eddy structures", no such evidence appears in the experimental data reported [9].

Further studies by Yagodkin, with Varapaev [11] and Sviridenkov [12] are theoretical, and address the problem of laminar stability of injected channel flows, i.e., transition to turbulence. Thus, modified versions of the Orr-Sommerfeld problem were investigated analytically [11] and numerically [12]. Two related laminar flow stability analyses are by Goldshtik, et al [13] and Alekseev, et al [14]. None of these theoretical analyses indicates the presence of large turbulent eddy structures prior to a full transition point, neither do they obtain an origin of such turbulence on the centerline upstream.

Recently Flandro [15] has carried out a theoretical analysis for a burning propellant in a cylindrical grain, under the effect of incident acoustic waves. A detailed formulation was derived with a double expansion, in terms of both inverse Reynolds number as well as Mach number (independent small parameters). A nonsteady premixed combustion zone was considered near the propellant surface; the assumption is made, however, that flow within the combustion zone is pure radial, i.e., zero axial component to all orders. Thus it could be anticipated that the results resemble (regarding nonsteady combustion behavior) those of T'ien [16], and there seems to be only small differences between the response to tangent and to perpendicular wave incidence. The problem is finally solved numerically, and details of the inner/outer matching process were not given.

In the remainder of this paper, the viscous, injected wall layer formulation is derived, in perturbation form. Analytical near field solutions are obtained for all variables up to second order, regarding the radial coordinate dependence; the remaining (x,t) -dependence is shown to be governed by relatively simple partial differential system. These solutions are discussed, with particular attention to the resultant (first order) pressure distribution and wall shear stress, for which experimental data are available.

NONLINEAR COMBUSTION INSTABILITY IN SOLID PROPELLANT MOTORS: VISCO-ACOUSTIC COUPLING

Dr. Moshe Ben-Reuven*
Princeton Combustion Research Laboratories, Inc.
Monmouth Junction, New Jersey

ABSTRACT

This analysis is aimed at the near-wall processes in an injected, axisymmetric, viscous flow. It is a part of an overall study of solid propellant rocket instability, in which cold flow simulation is evaluated as a tool to elucidate possible instability-driving mechanisms. One such prominent mechanism seems to be visco-acoustic coupling, as indicated by earlier detailed order of magnitude analysis. The major component of the overall study, not reported herein, involves numerical simulation of the full coreflow equations of motion (nonsteady, axisymmetric) by a modified MacCormack integration technique. The formulation is presented in terms of a singular boundary layer problem, with detail (up to second order) given only to the near-wall region. The injection Reynolds number is assumed large, and its inverse square root serves as an appropriate small-perturbation quantity. The injected Mach number is also small, and taken of the same order as the aforesaid small quantity. The radial-dependence of the inner solutions up to second order is solved, in polynomial form. This leaves the (x,t) dependence to much simpler partial differential equations. Particular results demonstrate the existence of a first-order pressure perturbation, which arises due to the dissipative near-wall processes. This pressure and the associated viscous friction coefficient are shown to agree very well with experimental injected flow data.

NOMENCLATURE

A_t, A	= nozzle throat area and port exit area, respectively
a	= adiabatic velocity of sound
C_f	= wall friction coefficient
C_v, C_p	= isochoric and isobaric specific heats (J/kg-K)
F	= radial mass flux (dimensionless)
G	= axial mass flux (dimensionless)
h	= thermal enthalpy, dimensionless
R_m	= ratio of inverse Reynolds number and Mach number squared
L	= chamber length
M	= Mach number
p	= pressure
P_r	= Prandtl number
R_0^*	= channel radius
Re_0	= injected Reynolds number
r	= radial coordinate
$S_{1,2,3}$	= "source"-terms in the equations of motion for coreflow
St_0	= Strouhal number, injected
t	= time (dimensionless)
U_0	= parameter defining (x,t) - variation of wall layer axial velocity component
u, u	= axial velocity, and mean axial coreflow velocity respectively

*Research Scientist
Member, AIAA

v	= radial velocity component
x	= axial distance (dimensionless)
y	= radial, magnified wall layer coordinate, perpendicular to surface,

Greek Symbols:

γ	= C_p/C_v , specific heat ratio
Δ	= difference, increment
δ	= length scales
ϵ	= small perturbation quantity
λ	= thermal conductivity of gas (air), J/K-m-s
μ	= viscosity coefficient, kg/m-s
ρ	= density

Subscripts, Superscripts:

$()_0$	= denotes zeroth order (perturbation)
$()_1$	= denotes first order perturbation
$()^*$	= denotes dimensional quantity

BACKGROUND

This is part of a study aimed at elucidation of the physical mechanisms capable of driving acoustic instability in solid propellant motors, particularly of the type termed velocity-coupled instability. Previous studies on the coupling between velocity oscillations and the combustion process in solid propellant motors have demonstrated the complexity of the overall phenomenon, but have not yet defined the basic mechanisms nor how they operate under flow conditions prevailing in rocket chambers. Critical literature review and order of magnitude analyses of velocity coupling mechanisms have been carried out, including visco-acoustic coupling and turbulence combustion coupling. The major goal of the study is the analytical simulation of the interior flow field within a solid propellant grain. The focus is on the Stokes layer, with the objective of investigating the particular instability mechanism of visco-acoustic coupling. Preliminary analysis has indicated that this mechanism is both plausible and sufficiently powerful to drive nonlinear vibrations; it has been shown that the frequency-dependent surface heat feedback component, due to viscous/acoustic coupling, has both phase and amplitude ranges which would enable driving of acoustic vibrations; its amplitude tends to increase as the mean coreflow Mach number and the frequency become higher. A comprehensive analytical model of the flow field within the viscous wall layer region has been derived, for an axisymmetric, nonsteady flow field configuration. For a simulation of the cold flow test results generated at UTC/CSD, four conservation equations are incorporated for continuity, momentum and energy.

UNCLASSIFIED

The corresponding injection Mach number is

$$M_o = v_o^* / a^* \quad (6)$$

The reference (injection) Reynolds number and Prandtl number are, respectively,

$$Re_o \equiv \rho_o^* v_o^* R_o^* / \mu^*, \quad Pr \equiv \mu^* c_p^* / \lambda^* \quad (7)$$

Recall that the viscosity, thermal conductivity and isobaric specific heat are all uniform and constant within the present cold-flow simulation. These idealizations are incorporated merely for convenience, in allowing clear identification of physical interactions within the coreflow, at low (axial) Mach numbers; sharp pressure and temperature variation are obviously precluded.

The dimensionless equations of motion are as follows, for the region

$$0 < x < 1, \quad 0 < r < 1, \quad t > 0:$$

$$\frac{\partial U}{\partial t} + \frac{1}{r} \frac{\partial}{\partial r}(rF) + \frac{\partial G}{\partial x} = S \quad (8)$$

where the dependent variable vector is,

$$U^T = (\rho \quad \rho v \quad \rho u \quad \rho h) \quad (9)$$

The radial and axial flux terms are, respectively,

$$F^T = (\rho v, \rho v^2, \rho uv, \sigma \rho h v) \quad (10)$$

$$G^T = (\rho u, \rho v u, \rho u^2 + \frac{p}{Re_o}, \sigma \rho h u) \quad (11)$$

where superscript T denotes vector transpose. The right-hand side (source) terms are defined: $S_1=0$,

$$S_2 = \frac{+1/3}{Re_o} \left(\frac{1}{r} \left(\frac{\partial v}{\partial r} - \frac{v}{r} \right) + \frac{1}{Re_o} \left(\frac{\partial^2 v}{\partial x^2} + \frac{1}{3} \frac{\partial^2 u}{\partial r \partial x} + \frac{4}{3} \frac{\partial^2 v}{\partial r^2} \right) - \frac{\sigma p / \sigma r}{Re_o^2} \right) \quad (12)$$

$$S_3 = \frac{1/r}{Re_o} \left(\frac{\partial u}{\partial r} + \frac{1}{3} \frac{\partial v}{\partial r} \right) + \frac{1}{Re_o} \left(\frac{\partial^2 u}{\partial r^2} + \frac{4}{3} \frac{\partial^2 u}{\partial x^2} + \frac{1}{3} \frac{\partial^2 v}{\partial r \partial x} \right) \quad (13)$$

$$S_4 = \sigma \left(v \frac{\partial p}{\partial r} + u \frac{\partial p}{\partial x} \right) + \frac{\sigma / Pr}{Re_o} \left(\frac{1}{r} \frac{\partial h}{\partial r} + \frac{\partial^2 h}{\partial r^2} + \frac{\partial^2 h}{\partial x^2} \right) + \frac{Mo^2}{Re_o} \sigma(r-1) \left\{ \frac{4}{3} \left[\frac{\partial^2 u}{\partial x^2} + \left(\frac{\partial v}{\partial r} \right)^2 + \left(\frac{v}{r} \right)^2 \right] + \left(\frac{\partial u}{\partial r} \right)^2 + \left(\frac{\partial v}{\partial x} \right)^2 - 4 \left[\frac{v}{r} \left(\frac{\partial v}{\partial r} + \frac{\partial u}{\partial x} \right) + \frac{\partial v}{\partial r} \cdot \frac{\partial u}{\partial x} \right] \right\} \quad (14)$$

The parameters, γ , Pr , Mo^2 , Re_o are all constants. Note that incorporation of the pressure gradient within the S_2 source term in the radial momentum equation, while the axial pressure gradient is included within the axial flux component, G_x , is merely for convenience. In the meantime, the viscous and thermal dissipative terms, $O(1/Re_o)$, are expected to be very small over most of the coreflow domain, excluding the neighborhood of the walls.

UNCLASSIFIED

UNCLASSIFIED

The following physical boundary data are available, for the cold-flow simulation:

(a) On the centerline, $(t, r=0, x)$:

$$v=0, \quad \partial u / \partial r = 0, \quad \partial p / \partial r = 0, \quad \partial h / \partial r = 0 \quad (15)$$

(b) At the porous (injected) surface, $(t, r=1, x)$:

$$v = -v_0(x,t), \quad u=0, \quad h = h_0(x,t) \quad (16)$$

(c) At the (nonpermeable solid) head-end closure, $(t, r, x=0)$:

$$v = 0, \quad u = 0, \quad h = h_H(r,t) \quad (17)$$

The functions $v_0(x,t)$, $h_0(x,t)$ and $h_H(r,t)$ are arbitrary imposed distributions.

(d) The exit plane, defined by $(t, r, x=L)$, forms an entrance into a short, convergent nozzle section. This nozzle section is treated separately from the rest of the flow field.

The foregoing discussion has summarized the coreflow analytical model, including the equations of motion and the relevant boundary data.

THE INJECTED SIDEWALL LAYER

The flow region of interest is close to the surface, where viscous forces are expected to be appreciable within a thin layer, as shown in Fig. 2.

For the neighborhood of $r=1$, the following transform is proposed for the radial coordinate:

$$y = (1-r)/\epsilon \quad (18)$$

which magnifies the wall layer, with

$$0 < \epsilon = 1/\sqrt{Re_0} \ll 1 \quad (19)$$

$$\partial / \partial r = -\frac{1}{\epsilon} \frac{\partial}{\partial y}, \quad \partial^2 / \partial r^2 = \frac{1}{\epsilon^2} \frac{\partial^2}{\partial y^2} \quad (20)$$

and

$$r = 1 - \epsilon y$$

The assumption for small injection Mach number is constrained as follows. Obviously, the injection Mach number appears as an additional parameter in the formulation (equations of momentum and energy). In the flow fields of interest for simulation herein, M_0 is also very small; in consideration of typical experiments at CSD/UTC with air injection, we find

$$M_0^2 \sim O(1/Re_0) \sim O(\epsilon^2)$$

which adequately represents a range of cold-flow conditions. This offers great simplification in the analysis, although at the cost of narrower range of general application (considering the relative freedom of the two major flow parameters, Re_0 and M_0). Therefore, a parameter is introduced,

$$K_m = (1/Re_0) / M_0^2 = \frac{\epsilon^2}{M_0^2} \sim O(1) \quad (21)$$

The question of timescale depends upon the range of frequencies of interest. The following reasoning will demonstrate that for the range of

UNCLASSIFIED

conditions considered for the present simulation, the timescale can remain the same one as in the coreflow. The viscous layer thickness is

$$\delta_v = R_0^* / \sqrt{Re_0} \quad (22)$$

The Stokes Layer thickness (for acoustic perturbations with a frequency f_0)

$$\delta_{STO} = (\nu^* / f_0)^{1/2} \quad (23)$$

The ratio of these two thickness scales is,

$$\delta_v / \delta_{STO} = \sqrt{f_0 R_0^* / \nu^*} = \sqrt{S_{RO}} \quad (24)$$

where S_{RO} is the relevant (injection) Strouhal number. The range of Strouhal numbers considered is $S_{RO} \sim 0(1)$, so one need not introduce any additional timescales.

The independent variables are (x, y, t) , while the associated dependent variables, in the wall-layer, are perturbed,

$$\xi = \xi_0 + \epsilon \xi_1, \quad v = v_0 + \epsilon v_1, \quad u = u_0 + \epsilon u_1, \quad h = h_0 + \epsilon h_1 \quad (25)$$

while the following abbreviations are introduced,

$$F_0 \equiv \rho_0 v_0, \quad G_0 \equiv \rho_0 u_0, \quad F_1 \equiv \rho_0 v_1 + \rho_1 v_0, \quad G_1 \equiv \rho_0 u_1 + \rho_1 u_0 \quad (26)$$

For the perturbation variables of Eqs. (18)-(26), the continuity equation yields

$$\frac{\partial}{\partial t}(\rho_0 + \epsilon \rho_1) - \frac{1}{\epsilon} \frac{\partial}{\partial y}(F_0 + \epsilon F_1 + \epsilon^2 \rho_1 v_1) + \frac{\partial}{\partial x}(G_0 + \epsilon G_1) = -(1 + \epsilon \gamma)(F_0 + \epsilon F_1) \quad (27)$$

The following hierarchy is collected:

ORDER $1/\epsilon$

$$-\partial F_0 / \partial y = 0 \Rightarrow F_0 = F_0(x, t) \quad (28)$$

ORDER ϵ^0 (ZEROth)

$$\frac{\partial \rho_0}{\partial t} + \frac{\partial G_0}{\partial x} - \frac{\partial F_1}{\partial y} = -F_0 \quad (29)$$

ORDER ϵ^1 (FIRST)

$$\frac{\partial \rho_1}{\partial t} + \frac{\partial G_1}{\partial x} - \frac{\partial \rho_1 v_1}{\partial y} = -F_1 - \gamma F_0. \quad (30)$$

The radial momentum balance, after similar substitution, yields the following hierarchy.

ORDER $1/\epsilon^3$:

$$-K_m \partial \rho_0 / \partial y = 0 \Rightarrow \rho_0 = \rho_0(x, t) \quad (31)$$

ORDER $1/\epsilon^2$:

$$-K_m \partial \rho_1 / \partial y = 0 \Rightarrow \rho_1 = \rho_1(x, t) \quad (32)$$

UNCLASSIFIED

ORDER $1/\epsilon$:

$$-\partial(F_0 v_0)/\partial y = 0 \quad (33)$$

ORDER ϵ^0 (ZEROth):

$$\frac{\partial F_0}{\partial t} + \frac{\partial}{\partial x}(F_0 u_0) - \frac{\partial}{\partial y}(F_0 v_1 + F_1 v_0) = -F_0 v_0 + \frac{4}{3} \frac{\partial^2 v_0}{\partial y^2} \quad (34)$$

ORDER ϵ^1 (FIRST):

$$\begin{aligned} \frac{\partial F_1}{\partial t} + \frac{\partial}{\partial x}(F_0 u_1 + F_1 u_0) - \frac{\partial}{\partial y}(v_1(F_1 + p_1 v_0)) = \\ -[F_0 v_0 y + (F_0 v_1 + F_1 v_0)] + \frac{4}{3} \frac{\partial^2 v_1}{\partial y^2} + \frac{4}{3} \frac{\partial v_0}{\partial y} - \frac{1}{3} \frac{\partial^2 u_0}{\partial y \partial x} \end{aligned} \quad (35)$$

Similarly, the axial momentum balance yields the associated hierarchy:

ORDER $1/\epsilon^2$:

$$K_m \partial p_0 / \partial x = 0 \Rightarrow p_0 = p_0(t) \quad (36)$$

ORDER $1/\epsilon$:

$$K_m \frac{\partial p_1}{\partial x} - \frac{\partial}{\partial y}(F_0 u_0) = 0 \quad (37)$$

where we used $F_0 u_0 = G_0 v_0$. This equation is of great importance, as will be shown later.

ORDER ϵ^0 (ZEROth):

$$\frac{\partial G_0}{\partial t} + \frac{\partial}{\partial x}(G_0 u_1 + G_1 u_0) - \frac{\partial}{\partial y}(G_0 v_1 + G_1 v_0) = -G_0 v_0 + \frac{\partial^2 u_0}{\partial y^2} \quad (38)$$

ORDER ϵ^1 (FIRST):

$$\begin{aligned} \frac{\partial G_1}{\partial t} + \frac{\partial}{\partial x}(G_1 u_0 + G_0 u_1) - \frac{\partial}{\partial y}(G_1 v_1 + p_1 v_0 u_1) = -(G_1 v_0 + G_0 v_1) \\ - G_0 v_0 y + \frac{\partial^2 u_1}{\partial y^2} - \frac{\partial u_0}{\partial y} - \frac{1}{3} \frac{\partial v_0}{\partial y} - \frac{1}{3} \frac{\partial^2 v_0}{\partial x \partial y} \end{aligned} \quad (39)$$

After similar substitution, the enthalpy equation in the wall layer yields the following hierarchy, for

$$\phi_0 \equiv p_0 h_0, \quad \phi_1 \equiv p_0 h_1 + p_1 h_0 \quad (40)$$

ORDER $1/\epsilon$:

$$-\tau \frac{\partial \phi_0 v_0}{\partial y} = -v_0 \frac{\partial \phi_0}{\partial y} \quad (41)$$

UNCLASSIFIED

Note that on the left hand side, according to Eqs. (28), (33)

$$\partial v_0 / \partial y = 0$$

(since $F_0 \neq 0$ in general). Now, according to Eq. (36), $p_0 = p_0(t)$, so that both sides are identically zero, as

$$\phi_0 = \phi_0(t) = \gamma p_0(t) / (\gamma - 1)$$

Therefore, Eq. (41) does not yield any new information.

ORDER ϵ^0 (ZEROth)

$$\begin{aligned} \frac{\partial \phi_0}{\partial t} + \frac{\partial}{\partial x} (\gamma \phi_0 u_0) - \frac{\partial}{\partial y} (\gamma \phi_0 v_0 + \gamma \phi_0 v_1) = -\gamma \phi_0 v_0 \\ + (\gamma - 1) \left[u_0 \frac{\partial \phi_0}{\partial x} - (v_1 \frac{\partial \phi_0}{\partial y} + v_0 \frac{\partial \phi_1}{\partial y}) \right] + \frac{\gamma}{Pr} \frac{\partial^2 \phi_0}{\partial y^2} \end{aligned}$$

(42)

ORDER ϵ^1 (FIRST)

$$\begin{aligned} \frac{\partial \phi_1}{\partial t} + \frac{\partial}{\partial x} (\gamma \phi_1 u_0 + \gamma u_1 \phi_0) - \frac{\partial}{\partial y} (\gamma \phi_1 v_1) = -\gamma \phi_0 v_0 \gamma + \gamma (\phi_0 v_1 + \phi_1 v_0) \\ + (\gamma - 1) \left\{ u_1 \frac{\partial \phi_0}{\partial x} + u_0 \frac{\partial \phi_1}{\partial x} - v_1 \frac{\partial \phi_1}{\partial y} \right\} \\ + \frac{\gamma}{Pr} \left(-\frac{\partial u_1}{\partial y} + \frac{\partial^2 \phi_1}{\partial y^2} \right). \end{aligned}$$

(43)

This concludes the derivation of the perturbed equations of motion.

The results of lower-order analysis can be summarized as follows. From Eq. (28),

$$\rho_0 v_0 = F_0 = F_0(x, t)$$

while from Eq. (2.87), using the last equation,

$$v_0 = v_0(x, t) \quad (44)$$

Thus ρ_0 , v_0 and F_0 are all independent of y . Further, from Eqs. (31) and (36) clearly

$$p_0 = p_0(t), \quad \phi_0 = \phi_0(t)$$

while from Eq. (32),

$$p_1 = p_1(x, t); \quad (45)$$

so that both p_0 and p_1 are independent of y . As a consequence of Eq. (45),

$$\rho_0 u_1 + \rho_1 u_0 = \phi_1(x, t) \quad (46)$$

One may now proceed to solve Eq. (37) directly for u_0 :

$$K_m \frac{\partial p_1}{\partial x} = F_0 \frac{\partial u_0}{\partial y} \Rightarrow u_0(x, y, t) = \frac{K_m}{F_0} \frac{\partial p_1}{\partial x} \cdot y$$

(47)

UNCLASSIFIED

with the boundary condition, (no-slip):

$$u_0(x, 0, t) = 0 \quad (48)$$

Of course, the (x, t) dependence of u_0 still remains to be found. However, its dependence upon the layer coordinate, y , is found to be linear; this result is certainly not obvious, and has several important implications.

The shear stress within the layer,

$$-\tau_{xy}^0 \sim \mu u_0 / \partial y = \frac{K_m}{F_0} \frac{\partial P}{\partial x} \quad (49)$$

is obviously nonzero in general, while being independent of distance from the wall at any given station (x, t) . Even more striking is the vanishing of the viscous dissipation term at zeroth order:

$$\partial^2 u_0 / \partial y^2 = 0$$

which leaves in the zeroth-order axial momentum equation a balance of inertial terms, strictly, cf. Eq. (38). This explains physically the success (up to first order) of modeling this family of injected flows by assuming rotational, inviscid motions; such modeling indeed obtains solutions for the axial velocity profile, which satisfy the no-slip condition at the wall ($r=1$).

It further appears that the shear stress, Eq. (49), is proportional to the first-order axial pressure gradient, while being inversely proportional to the injected mass flux, as would be expected. Of course, $\partial P / \partial x$ depends on F_0 , and one expects their ratio to be finite at the limit as zero injection is approached.

In addition to the foregoing result for axial velocity, the zeroth order formulation can be utilized to solve for the y -dependence of the other dependent variables. The zeroth order continuity equation can be written now as

$$\partial g_0 / \partial x + \partial (G_0) / \partial x - \partial F_1 / \partial y + F_0 = 0$$

Now, since F_0 and g_0 are independent of y , hence, one may split the foregoing equation,

$$\partial g_0 / \partial x + F_0(x, t) = C_0(x, t) \quad (50)$$

$$\frac{\partial}{\partial x} \left(\frac{K_m}{V_0} \frac{\partial P}{\partial x} \right) y - \frac{\partial F_1}{\partial y} = -C_0(x, t) \quad (51)$$

where $C_0(x, t)$ is a common separation parameter, with a range of values uniquely corresponding to the boundary data.

The second equation yields

$$F_1(y, x, t) = B_0(x, t) + C_0(x, t) \cdot y + \frac{1}{2} \frac{\partial g_0}{\partial x} y^2 \quad (52)$$

where:

$$B_0(x, t) = F_1(0, x, t) \quad (53)$$

$$g_0(x, t) = \frac{K_m}{V_0} \frac{\partial P}{\partial x} \quad (54)$$

Similarly, from the zeroth order radial momentum equation:

$$\partial F_0 / \partial x + F_0 V_0 = C_1(x, t) \quad (55)$$

UNCLASSIFIED

$$\frac{\partial}{\partial x} \left(K_m \frac{\partial \rho_1}{\partial x} \right) y - \frac{\partial}{\partial y} (V_0 F_1 + V_1 F_0) = -C_1(x, t) \quad (56)$$

The last equation can be integrated,

$$V_1(y, x, t) = B_1(x, t) + \frac{C_1 - V_0 C_0}{F_0} y + \frac{1}{2} \frac{K_m}{F_0} \frac{\partial \rho_1}{\partial x} \left(\frac{\partial h_1 V_0}{\partial x} \right) y^2, \quad (57)$$

$$B_1 = V_1(0, x, t).$$

The foregoing results for F_1 and V_1 yield for the first-order density:

$$\rho_1(y, x, t) = (B_0 - \rho_0 B_1)/V_0 + (2C_0 - C_1/V_0) y + \frac{1}{2} \frac{K_m}{V_0^2} \left[\frac{\partial^2 \rho_1}{\partial x^2} - 2 \frac{\partial \rho_1}{\partial x} \frac{\partial h_1 V_0}{\partial x} \right] y^2 \quad (58)$$

Note that: $\rho_1(0, x, t) = (B_0 - \rho_0 B_1)/V_0$

so that ρ_1 is uniquely defined and an additional integration constant is not necessary.

Now, following the definition of ϕ_1 and since

$$\partial \phi_1 / \partial y = 0, \quad \partial h_0 / \partial y = \partial \rho_0 / \partial y = 0,$$

then:

$$h_1(y, x, t) = \frac{h_0}{\rho_0} \rho_1(y, x, t) + B_2(x, t) \quad (59)$$

Thus, $h_1(y, x, t)$ is second order in y , like ρ_1 ; the appropriate boundary condition is,

$$B_2(x, t) = h_1(0, x, t) - h_0(B_0 - \rho_0 B_1)/F_0 \quad (60)$$

The axial momentum, after dividing through by F_0 , Eq. (38) leads to:

$$\frac{1}{F_0} \frac{\partial \rho_0}{\partial t} + \frac{1}{V_0} \frac{\partial h_1 u_0}{\partial t} + \frac{u_0}{F_0} \frac{\partial \rho_0}{\partial x} + \frac{2}{V_0} \frac{\partial u_0}{\partial x} - \frac{1}{u_0} \frac{\partial u_1}{\partial y} - \frac{1}{F_0} \frac{\partial F_1}{\partial y} - \frac{F_1}{F_0} \frac{\partial h_1 u_0}{\partial y} = -1. \quad (61)$$

Now, according to the foregoing results:

$$\frac{1}{F_0} \frac{\partial \rho_0}{\partial t} = \frac{C_0}{F_0} - 1 \quad (62)$$

$$-\frac{1}{F_0} \frac{\partial F_1}{\partial y} = -\frac{1}{F_0} \frac{\partial \rho_0}{\partial x} y - \frac{C_0}{F_0} \quad (63)$$

$$-\frac{F_1}{F_0} \frac{\partial h_1 u_0}{\partial y} = -F_1/F_0 y \quad (64)$$

Substitution into Eq. (61) yields, after some manipulation:

$$\frac{\partial u_1}{\partial y} = \left[\rho_0 \frac{\partial u_0}{\partial x} - \frac{1}{2} \frac{\partial \rho_0}{\partial x} \right] \frac{U_0}{F_0} y^2 + \left(\frac{1}{V_0} \frac{\partial u_0}{\partial t} - \frac{C_0 U_0}{F_0} \right) y - \frac{B_0 U_0}{F_0} \quad (65)$$

UNCLASSIFIED

UNCLASSIFIED

where

$$U_0(x,t) \equiv \frac{k_m}{F_0} \left(\frac{\partial p_1}{\partial x} \right) = g_0 / \rho_0 \quad (66)$$

thus,

$$u_1(y,x,t) = \frac{U_0}{F_0} \left[\rho_0 \frac{\partial u}{\partial x} - \frac{1}{2} \frac{\partial^2 p_0}{\partial x^2} \right] \frac{y^3}{3} + \left(\frac{1}{V_0} \frac{\partial U_0}{\partial t} - \frac{C_0 U_0}{F_0} \right) \frac{y^2}{2} - \frac{B_0 U_0}{F_0} y \quad (67)$$

and

$$u_1(0,x,t) = 0$$

satisfying the no-slip condition at the wall. Thus, the perturbed axial velocity is third order in its y-dependence, and the corresponding viscous dissipation term (unlike its zeroth-order counterpart), does not vanish within the layer.

With the foregoing derived results, the zeroth order energy equation can be shown to yield merely a condition connecting U_0 and V_0 timewise:

$$U_0/V_0 = C_4(t) \quad (68)$$

One may turn now to the first-order energy equation, which seems to yield some simply and highly useful results even without full solution. Equation (43) written in terms of pressure, reads:

$$\begin{aligned} \frac{\partial p_1}{\partial t} + \gamma \frac{\partial}{\partial x} [p_1 u_0 + p_0 u_1] - \gamma \frac{\partial}{\partial y} p_1 v_1 = -\gamma \{ p_0 v_0 y + p_1 v_0 + p_0 v_1 \} \\ + (\gamma-1) u_0 \frac{\partial p_1}{\partial x} + \frac{\gamma-1}{P_r} \frac{\partial^2 h_1}{\partial y^2} \end{aligned} \quad (69)$$

After some manipulation one obtains:

$$\frac{\partial p_1}{\partial t} + \gamma p_1 \left(\frac{\partial u_0}{\partial x} - \frac{\partial v_1}{\partial y} + v_0 \right) + \gamma p_0 \left(\frac{\partial u_1}{\partial x} + v_0 y + v_1 \right) + u_0 \frac{\partial p_1}{\partial x} - \frac{\gamma-1}{P_r} \frac{\partial^2 h_1}{\partial y^2} \quad (70)$$

The first bracketed term, after using Eq. (68) and the foregoing results, is simply

$$v_0 = (C_1 - v_0 C_0) / F_0$$

The enthalpy term, according to Eqs. (58) and (59) is:

$$\frac{\partial^2 h_1}{\partial y^2} = \frac{h_0}{V_0} \left(\frac{\partial^2 p_1}{\partial x^2} - 2 \frac{\partial p_1}{\partial x} \frac{\partial u_0}{\partial x} \right) \frac{k_m}{V_0} = h_0 \frac{\partial}{\partial x} \left(\frac{\partial p_0}{\partial x} \right). \quad (71)$$

The first order axial velocity gradient can be found from Eq. (67). Substitution of the last results along with the appropriate expression for v_1 , into Eq. (70) and collection of equal powers of y yields:

UNCLASSIFIED

$$\begin{aligned} & \left\{ \frac{\partial p_1}{\partial t} + \gamma p_1 (V_0 - \frac{C_1 - V_0 C_0}{F_0}) - \frac{\gamma - 1}{\gamma} h_0 \frac{\partial}{\partial x} \left(\frac{q_0}{V_0} \right) + \gamma p_0 B_1 \right\} y^0 \\ & + \left\{ -\gamma p_0 \frac{\partial}{\partial x} \left(\frac{B_0 U_0}{F_0} \right) + \gamma p_0 V_0 + \frac{C_1 - C_0 V_0}{F_0} \gamma p_0 + U_0 \frac{\partial p_1}{\partial x} \right\} y \\ & + \left\{ \gamma p_0 U_0 \frac{\partial h_0 V_0}{\partial x} + \gamma p_0 \frac{\partial}{\partial x} \left[\frac{1}{V_0} \frac{\partial U_0}{\partial t} - \frac{C_0 U_0}{F_0} \right] \right\} y^{3/2} \\ & + \frac{\partial}{\partial x} \left\{ \frac{U_0}{V_0} \frac{p_0}{2} \frac{\partial}{\partial x} (U_0 / p_0) \right\} y^{3/3} = 0. \end{aligned} \quad (72)$$

Compatibility with the foregoing derivation (in which y and (x,t) variable separation was implemented), can be maintained, provided each of the bracketed terms in Eq. (72) vanishes identically. The resulting four compatibility relations (partial differential) would determine the behavior of the wall sublayer system up to the first order in ϵ , the small perturbation quantity. However, a total of three undetermined coefficients should arise necessarily, to accommodate coupling with the outer, inviscid (core) flowfield, through inner/outer asymptotic matching.

THE FIRST ORDER PRESSURE PERTURBATION

Of particular interest in the present analysis is the pressure,

$$p(y, x, t) = p_0(t) + \epsilon p_1(x, t)$$

which is a directly measurable quantity. From the axial momentum balance in perturbed form, it is evident that the rotational ("inviscid") coreflow can not sustain a first order term like $\partial p_1 / \partial x$ herein; the lowest-order axial pressure gradient effect evolves only at second order, or $\epsilon^2 p_2$ -level. This is clearly borne out in the analyses of Culick, and others, in which the axial pressure drop is proportional to γM_0^2 (Mach number of injection, squared), or to ϵ^2 according to the convention employed here.

This, however, is not what is observed in the recent injected cold flow experiments of Brown, et al at CSD/UTC; the measured axial pressure profiles clearly indicate variation of order $M_0^{-1} \epsilon$, or first order.

It therefore seems that the viscous wall layer, with its inherent first-order dissipative processes, impresses this axial pressure variation, at first order, over the entire cross section of the injected channel. Needless to say, this would involve a corresponding variation or distortion of the coreflow radial and axial velocity profiles - from their zeroth order representation.

To resolve the axial variation of p_1 by the wall layer formulation, the second compatibility condition in Eq. (72) can be used, corresponding to the y-term:

$$\frac{\partial}{\partial x} \left(\frac{B_0 U_0}{F_0} \right) + V_0 + \frac{C_1 - C_0 V_0}{F_0} + \frac{U_0}{\gamma p_0} \frac{\partial p_1}{\partial x} = 0 \quad (73)$$

For the special case of uniform (zeroth order) injection at steady state, the presence of a nonzero first-order pressure perturbation would imply physically a corresponding nonzero perturbation upon the mass flux injected, i.e.,

$$B_0 = F_1(0, x, t) \neq 0$$

as given by Eq. (53). Now at steady state, although B_0 is expected to vary with p_1 , we will assume for simplicity that $B_0(x) = B_0 = \text{const.}$

With the foregoing steady state assumptions, Eq. (73) can be readily turned into an ordinary differential equation, for $0 < x < L$:

$$\frac{d^2 p_1}{dx^2} + b_1 \left(\frac{dp_1}{dx} \right)^2 + b_0 = 0 \quad (74)$$

UNCLASSIFIED

UNCLASSIFIED

where $p_1(x)$ is the steady state first-order pressure perturbation; the coefficients are:

$$b_0 \equiv \frac{F_0/B_0}{K_m/v_0}, \quad b_1 \equiv \frac{F_0/B_0}{\sigma p_0} \quad (75)$$

Note that at steady state, according to Eqs. (50) and (55), respectively, $C_0 = F_0$ and $C_1 = F_0 v_0$; thus, in Eq. (73), $C_1 - C_0 v_0 = 0$.

The boundary data are,

$$dp_1/dx(0) = 0, \quad \text{and} \quad p_1(x=L) = p_L \quad (76)$$

The solution is straightforward,

$$dp_1/dx = -\sqrt{b_0/b_1} \operatorname{tg}(\sqrt{b_0 b_1} x) \quad (77)$$

$$p_1(x) = p_1^0 + \frac{1}{b_1} \ln |\cos(\sqrt{b_0 b_1} x)| \quad (78)$$

This concludes the derivation of the injected, viscous wall layer, up to second order. Full solutions, namely, matching between inner and outer expansions will not be attempted herein. Important insights are obtained already from resolving the near-field behavior up to second order, in terms of the y-polynomials.

DISCUSSION OF RESULTS

To facilitate comparison with the experimental data reported by Brown, et al, one may form the normalized axial pressure differential,

$$\Delta p_1 = \frac{\Delta P}{\varepsilon p_0} = \frac{1}{\varepsilon p_0} (P(x=0) - P(x)) = \frac{1}{b_1 p_0} \ln |\cos \sqrt{b_0 b_1} x| \quad (79)$$

This axial pressure differential expression is used to correlate the experimental data of Brown, et al, as shown in Fig. 3. Clearly, the measured pressure profile is correlated very well by Eq. (79), which is obviously superior to the expression attributed to Culick, shown as well.

It should be pointed out that a single point of the data ($x; \Delta p_1$) has been utilized to obtain a scale for the comparison (this is necessary, since no physical input is available regarding the value of B_0 , the perturbed injected mass flux, necessary for defining b_1, b_0), along with $p_0 = F_0 = v_0 = 1$, and $\gamma = 1.4$. Suppose now that $K_m = 1$, and we select a value of $B_0 = 60$. (This is based on some trial and error - but shows how the correlation was obtained without any regression analysis); then,

$$b_0 = 1/B_0 = 1/60, \quad b_1 = 1/\gamma B_0 = 1/1.4 \times 60 = 0.012$$

$$\sqrt{b_0 b_1} = 1/\sqrt{\gamma} B_0 = 0.014$$

Two important observations are therefore demonstrated: (1) axial pressure variation to lowest order is $O(\varepsilon)$, and is governed by the dissipative wall layer processes, as shown in the rigorous analysis herein. The behavior obtained in x differs from than the parabolic pressure drop formula of Culick [1], and (2) one need not invoke local turbulence generation or turbulence encroachment upon the surface to explain the departure of measured p_1 from a laminar behavior.

Another property of interest is the wall friction coefficient, or dimensionless wall shear stress,

$$C_f = \tau_w^* / \frac{1}{2} \rho^* \bar{u}^* = -\mu^* \frac{\partial u^*}{\partial y^*} / \frac{1}{2} \rho^* \bar{u}^*$$

UNCLASSIFIED

UNCLASSIFIED

here \bar{u}^* denotes the mean axial coreflow velocity. Using dimensionless convention employed herein, along with the wall layer coordinate,

$$C_{f0} = - \varepsilon \frac{\partial u_0 / \partial y}{2x^2} \quad (80)$$

where $u_0 = 2x$ was used, for a cylindrical port, and subscript zero denotes zeroth order convention.

Now, from Eqs. (47) and (77),

$$C_{f0} = \varepsilon \cdot \frac{1}{2} \left(\frac{K_m}{F_0} \frac{\partial P_0}{\partial y} \right)^{1/2} \tan(\sqrt{b_0 b_1} x) / x^2 \quad (81)$$

where the first square root term is of order unity. This parameter is plotted against $1/2x$ (which denotes the ratio of blowing to mean axial velocity) in Fig. 6. A nearly linear relationship is obtained, using the foregoing coefficient values. In comparison, the data obtained by Olson and Eckert [6] is considered. Ref. 6 includes a plot of the ratio of (axial pressure gradient)/(mean dynamic axial head) vs $v_{00}^*/u_0^* = 1/2x$. This obtains an almost linear correlation, as would be expected from a parabolic pressure drop. The slight curvature however, particularly apparent at small values of $1/2x < 0.01$, can be followed only with the present formulation, not with any parabolic pressure profile. Thus, the first order pressure distribution, obtained from the viscous wall layer analysis, agrees well with the measured data of Brown, et al [8], while the associated wall friction coefficient follows the same trend as that measured by Olson and Eckert [6].

CONCLUSIONS

A derivation of the viscous wall layer regime has been presented, pertaining to injected flow in an axial porous tube, in simulation of interior solid propellant rocket flows.

Solutions for the radial coordinate (or y-dependence) of all the dependent variables up to the second order have been generated, in polynomial form. The (x,t) -dependence is defined in terms of a relatively simple partial differential system.

Particular results of the analysis for the special case of steady state, are: (1) the first order pressure perturbation was solved for and its axial distribution is given explicitly; this term is entirely due to the laminar dissipative wall-layer processes, and (2) the blown wall friction coefficient was likewise defined. Both results correlate well the available experimental data. Finally, (3) the zeroth order axial velocity distribution within the layer is linear radially; thus, to lowest order, viscous dissipation is negligible in the axial momentum balance. This indicates why inviscid, rotational solutions (such as those of Culick [1] and others, chosen so as to satisfy the no-slip condition at the wall) are so successful in representing these family of flows - up to first order.

NOMENCLATURE

A_t, A	= nozzle throat area and port exit area, respectively
a	= adiabatic velocity of sound
C_f	= wall friction coefficient, Eq. (80)
C_v, C_p	= isochoric and isobaric specific heats (J/kg-K)
F	= radial mass flux (dimensionless)
G	= axial mass flux (dimensionless)

UNCLASSIFIED

h	= thermal enthalpy, dimensionless
K_m	= ratio of inverse Reynolds number and Mach number squared, Eq. (21)
L	= chamber length
M	= Mach number
p	= pressure
P_r	= Prandtl number, Eq. (7)
R_o^*	= channel radius
Re_o	= injected Reynolds number, Eq. (7)
r	= radial coordinate
$S_{1,2,3}$	= "source"-terms in the equations of motion for coreflow, Eqs. (12)-(14)
S_{RO}	= Strouhal number, injected, (Eq. 24)
t	= time (dimensionless)
U_o	= parameter defining (x,t) - variation of wall layer axial velocity component
u, u	= axial velocity, and mean axial coreflow velocity respectively
v	= radial velocity component
x	= axial distance (dimensionless)
y	= radial, magnified wall layer coordinate, perpendicular to surface, Eq. (18)

Greek Symbols:

γ	= C_p/C_v specific heat ratio
Δ	= difference, increment, Eq. (79)
δ	= length scales, Eqs. (22)-(24)
ϵ	= small perturbation quantity, Eq. (19)
λ	= thermal conductivity of gas (air), J/K-m-s
μ	= viscosity coefficient, kg/m-s
ρ	= density

Subscripts, Superscripts:

$()_o$	= denotes zeroth order (perturbation)
$()_1$	= denotes first order perturbation
$()^*$	= denotes dimensional quantity

UNCLASSIFIED

UNCLASSIFIED

REFERENCES

- Culick, F.E.C., "Rotational, Axisymmetric Mean Flow and Damping of Acoustic Waves in a Solid Propellant Rocket", AIAA Journal, Vol 4, No. 8, August 1966, pp. 1462-1464.
- Berman, A.S., "Laminar Flow in Channels with Porous Walls", Journal of Applied Physics, Vol. 24, No. 9, September 1953, pp. 1232-1235.
- Sir Geoffrey Taylor, "Fluid Flow in Regions Bound by Porous Surfaces", Proc. Royal Soc. of London, Ser. A., Vol. 234, No. 1199 (1956), pp. 456-475.
- Wageman, W.E., and Guevara, F.A., "Fluid Flow Through a Porous Channel", The Physics of Fluids, Vol. 3, No. 6, November-December 1960, pp. 878-881.
- Dunlap, R., Willoughby, P.G., and Hermesen, R.W., "Flowfield in the Combustion Chamber of a Solid Propellant Rocket Motor", AIAA Journal, Vol. 12, No. 10, October 1974, pp. 1440-1442.
- Olson, R.M., and Eckert, E.R.G., "Experimental Studies of Turbulent Flow in a Porous Circular Tube with Uniform Fluid Injection Through the Tube Walls", Jour. of Appl. Mech./Transactions of the ASME, March 1966, pp. 7-17.
- Huesman, K., and Eckert, E.R.G., "Studies of the Laminar Flow and Transition to Turbulence in Porous Tubes, with Uniform Injection Through the Tube Wall", (Translation), Warme und Stoffubertrannung, Bd. 1 (1968), pp. 2-9.
- Brown, R.S., Waugh, R.C., Willoughby, P.G., and Dunlap, R., "Coupling Between Velocity Oscillations and Solid Propellant Combustion", 19th JANNAF Combustion Meeting, October 1982, CPIA Publication 366, Vol. 1, pp. 191-208.
- Yagodka, V.I., "Use of Channels with Porous Walls for Studying Flows Which Occur During Combustion of Solid Propellants", Proc. 18th Aeronautics Congress, Vol. 3, 1967, pp. 69-79. (Trans.)
- Yamada, K. Goto, M., and Ishikawa, N., "Simulative Study on the Erosive Burning of Solid Rocket Motors", AIAA Journal, Vol. 14, No. 9, September 1976, pp. 1170-1177.
- Varapaev, V.N. and Yagodka, V.I., "Flow Instability in a Channel with Porous Walls", AN, SSSR, Mekhanika Zhidkosti i Gaza, Vol. 4, No. 5, pp. 91-95, 1969. (Trans.)
- Sviridenkov, A.A., and Yagodka, V.I., "Flow in the Initial Sections of Channels with Permeable Walls", Izv. AN, SSSR, Mekhanika Zhidkosti i Gaza, No. 5, pp. 43-48, September-October 1976 (Moscow). (Trans.)
- Goldshchik, M.A., and Sapozhnikov, V.A., "Laminar Flow Stability in a Mass Force Field", Izv. AN. SSSR, Mekhanika Zhidkosti i Gaza, Vol. 3, No. 5, pp. 42-46, 1969.
- Alekseev, Yu. N., and Korotkin, A.I., "Effect of Transverse Stream Velocity in an Incompressible Boundary Layer on the Stability of the Laminar Flow Regime", Mekhanika Zhidkosti i Gaza, Vol. 1, No. 1, pp. 32-36, 1966.
- Flandro, G.A., "Nonlinear Time Dependent Combustion of a Solid Rocket Propellant", Proc. 19th JANNAF Combustion Meeting, October 1982, CPIA Publication 366, Vol. II, pp. 111-122.
- T'ien, J., "Oscillatory Burning of Solid Propellants including Gas Phase Time Lag", Combustion Science and Technology, Vol. 5, 1972, pp. 47-54.

UNCLASSIFIED

AD-A151 999

ANALYSIS OF COMBUSTION OSCILLATIONS IN HETEROGENEOUS
SYSTEMS(U) PRINCETON COMBUSTION RESEARCH LABS INC NJ
H BEN-REUVEN MAY 84 PCRL-FR-84-002 AFOSR-TR-85-0250
F49620-82-C-0062 F/G 21/2

2/2

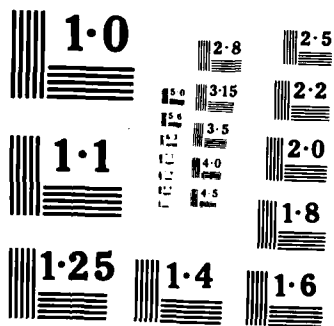
UNCLASSIFIED

NL

END

FILED

DATE



UNCLASSIFIED

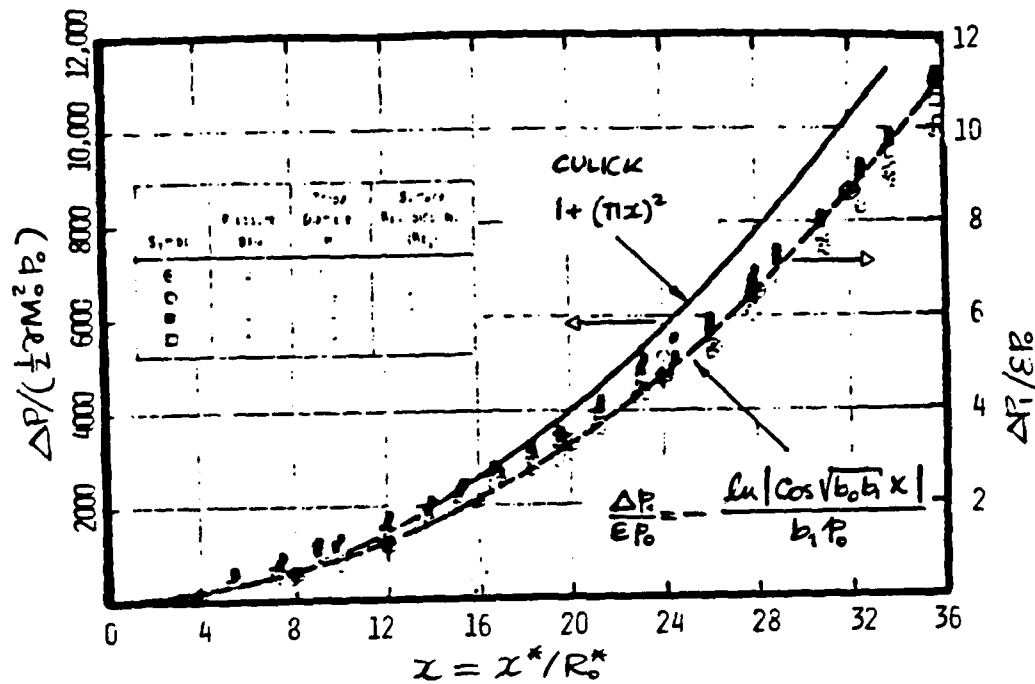


Figure 3. Axial pressure distribution: correlation of the experimental data of Brown, et al [8] by the present theory, Eq. (79), shown superior to the parabolic distribution of Culick.

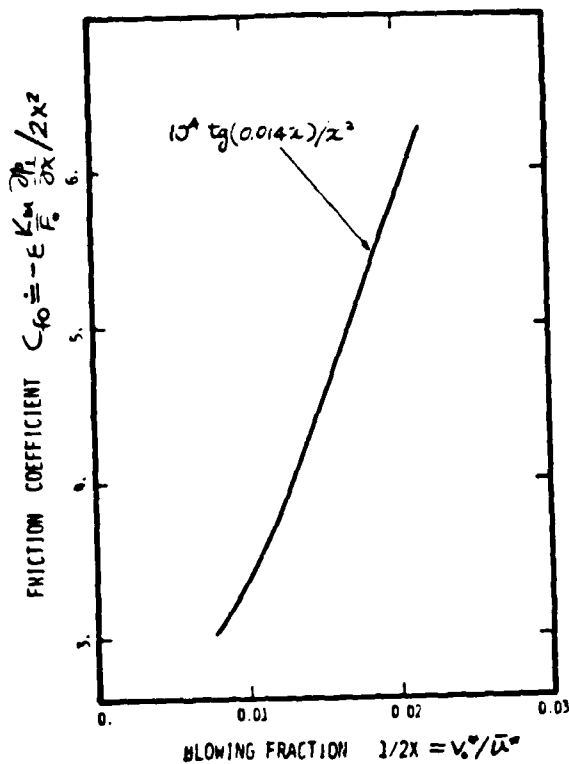
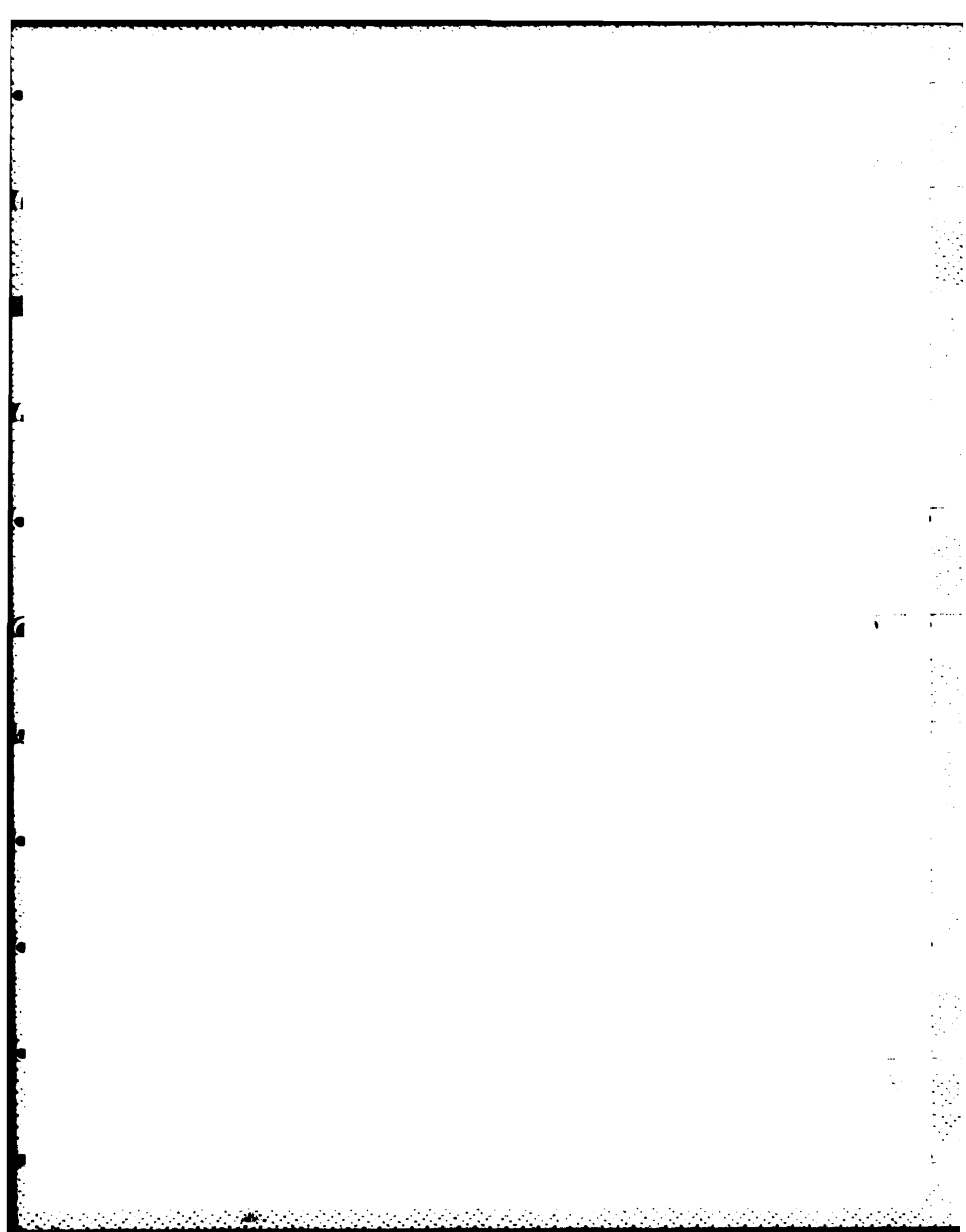


Figure 4. Wall friction coefficient vs reduced blowing rate showing slight curvature at small blowing fraction. This agrees well with the results of Olson and Eckert [6], and could not be explained by the inviscid solutions of Culick [1].

UNCLASSIFIED



END

FILMED

5-85

DTIC